

AD-A197 947

④

NUSC Technical Report 6638
9 March 1988

Aerodynamic Drag of Cylindrical Vehicles Moving Concentrically Within Long Tubes

D.A. Kotlow
Launcher and Missile Systems Department



DTIC
ELECTE
AUG 12 1988
S E D

Naval Underwater Systems Center
Newport, Rhode Island/New London, Connecticut

Approved for public release; distribution unlimited.

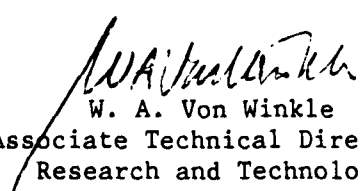
PREFACE

The Naval Underwater Systems Center (NUSC) supplied funding for this study under the Independent Research and Independent Exploratory Development (IR/IED) Project No. A43126. NUSC's Launcher Development Branch (Code 8321), under the direction of R. C. White, supplied additional funding necessary to complete the study. The principal investigator was R. F. Hubbell (Code 8321), and the associate investigator was D. A. Kotlow (Code 8321).

The technical reviewer for this report was Dr. F. M. White, Department of Mechanical Engineering and Applied Mechanics, University of Rhode Island.

Special thanks are expressed to R. F. Hubbell and Dr. F. M. White for their encouragement and many helpful suggestions during the course of this investigation.

REVIEWED AND APPROVED: 9 MARCH 1988


W. A. Von Winkle
Associate Technical Director,
Research and Technology

REPORT DOCUMENTATION PAGE

1a. REPORT SECURITY CLASSIFICATION UNCLASSIFIED			1b. RESTRICTIVE MARKINGS		
2a. SECURITY CLASSIFICATION AUTHORITY			3. DISTRIBUTION/AVAILABILITY OF REPORT Approved for public release; distribution unlimited		
2b. DECLASSIFICATION/DOWNGRADING SCHEDULE					
4. PERFORMING ORGANIZATION REPORT NUMBER(S) TR 6638			5. MONITORING ORGANIZATION REPORT NUMBER(S)		
6a. NAME OF PERFORMING ORGANIZATION Naval Underwater Systems Ctr		6b. OFFICE SYMBOL (if applicable) Code 8321		7a. NAME OF MONITORING ORGANIZATION	
6c. ADDRESS (City, State, and ZIP Code) Newport Laboratory Newport, Rhode Island 02841			7b. ADDRESS (City, State, and ZIP Code)		
8a. NAME OF FUNDING/SPONSORING ORGANIZATION		8b. OFFICE SYMBOL (if applicable)		9. PROCUREMENT INSTRUMENT IDENTIFICATION NUMBER	
8c. ADDRESS (City, State, and ZIP Code)			10. SOURCE OF FUNDING NUMBERS		
			PROGRAM ELEMENT NO.	PROJECT NO.	TASK NO.
			WORK UNIT ACCESSION NO.		
11. TITLE (Include Security Classification) AERODYNAMIC DRAG OF CYLINDRICAL VEHICLES MOVING CONCENTRICALLY WITHIN LONG TUBES					
12. PERSONAL AUTHOR(S) Kotlow, D. A.					
13a. TYPE OF REPORT		13b. TIME COVERED FROM TO		14. DATE OF REPORT (Year, Month, Day) 88-03-09	
				15. PAGE COUNT 127	
16. SUPPLEMENTARY NOTATION					
17. COSATI CODES			18. SUBJECT TERMS (Continue on reverse if necessary and identify by block number)		
FIELD	GROUP	SUB-GROUP			
20	04		Drag Forces; Cylindrical Vehicles; Annular Region Flow Modeling.		
19. ABSTRACT (Continue on reverse if necessary and identify by block number)					
<p>A numerical analysis is made of developing and developed turbulent flow in the annular region between a cylinder moving at constant velocity within a fixed concentric tube. Turbulent shear is modeled by eddy viscosity, and a uniform velocity is assumed at the entrance to the annular region. The computations extend and modify the method of Sud and Chaddock (1981) to arbitrary Reynolds numbers and radius ratios.</p> <p>This report is based on the author's masters thesis, for the University of Rhode Island. However, the fully developed flow results herein are more complete, and those for developing flow are more accurate. Better accuracy was achieved by implementing double precision, which enabled the computations to be performed further into the developing region.</p>					
20. DISTRIBUTION/AVAILABILITY OF ABSTRACT <input type="checkbox"/> UNCLASSIFIED/UNLIMITED <input checked="" type="checkbox"/> SAME AS RPT. <input type="checkbox"/> DTIC USERS			21. ABSTRACT SECURITY CLASSIFICATION UNCLASSIFIED		
22a. NAME OF RESPONSIBLE INDIVIDUAL D. A. Kotlow			22b. TELEPHONE (Include Area Code) (401) 841-1993		22c. OFFICE SYMBOL Code 8321

TABLE OF CONTENTS

Section	Page
LIST OF ILLUSTRATIONS.	iii
LIST OF TABLES	v
LIST OF SYMBOLS.	vi
1 INTRODUCTION	1-1
2 ANALYSIS OF FULLY DEVELOPED FLOW	2-1
Experimental Survey	2-1
Analytical Survey	2-3
Assumptions and Boundary Conditions	2-4
Determination of Velocity Profiles	2-7
Derivation of Shear Stress Ratios	2-14
Derivation of Reynolds Number for Continuity Check . .	2-21
Derivation of Friction Factor and Drag Equations . . .	2-24
Results	2-26
Conclusions	2-35
3 ANALYSIS OF DEVELOPING FLOW	3-1
Experimental Survey	3-1
Analytical Survey	3-8
Assumptions and Boundary Conditions	3-13
Location of Velocity Profiles	3-13
Scheme for Determining Vehicle Drag in Developing Flow	3-27
Results	3-29
4 CONCLUSIONS AND RECOMMENDATIONS.	4-1
APPENDIX A — COMPUTATIONAL SCHEME FOR DETERMINING DRAG IN THE REGION OF FULLY DEVELOPED FLOW	A-1
APPENDIX B — TABULATED RESULTS OF ANALYSIS FOR FULLY DEVELOPED FLOW	B-1
APPENDIX C — COMPARISON OF MOODY CHART METHOD AND PRESENT THEORY FOR PREDICTING PRESSURE DROP THROUGH ANNULI WITH A MOVING BOUNDARY	C-1

TABLE OF CONTENTS (Cont'd)

Section	Page
APPENDIX D -- COMPUTATIONAL SCHEME FOR DETERMINING DRAG IN THE REGION OF DEVELOPING FLOW.	D-1
APPENDIX E -- DRAG PREDICTION USING FULLY DEVELOPED AND DEVELOPING FLOW RESULTS TO QUANTIFY THE VARIOUS DRAG CONTRIBUTIONS	E-1
APPENDIX F -- TABULATED RESULTS OF ANALYSIS FOR DEVELOPING FLOW	F-1
APPENDIX G -- DATA TABLES FOR $U_v = 40$ FEET/SECOND, $b = 1.143$ RUN	G-1
APPENDIX H -- METHOD USED TO ESTIMATE NOSE AND BASE DRAG .	H-1
REFERENCES	R-1
BIBLIOGRAPHY	R-3

Accession For	
NTIS GRA&I	<input checked="" type="checkbox"/>
DTIC TAB	<input type="checkbox"/>
Unannounced	<input type="checkbox"/>
Justification	
By	
Distribution/	
Availability Codes	
Dist	Avail and/or Special
A-1	



LIST OF ILLUSTRATIONS

Figure		Page
1-1	Launch Methods	1-2
1-2	Description of the Mass Continuity	1-2
2-1	Depiction of r_{mt} , $r_{m\phi}$ for Fully Developed Flow Through Concentric Annuli.	2-2
2-2	Velocity Development of Fluid in Annular Region.	2-6
2-3	Profile Analogy Between Moving Tube and Moving Vehicle . .	2-6
2-4	Relationships Between y_{ϕ}^+ and Re_b and Between n^2 and y_{mt}^+ (from Reference 15).	2-10
2-5	Suggested Number of Steps (in Runge-Kutta Routine) for Turbulent Region Calculations.	2-13
2-6	Force Balance Over Entire Annular Segment	2-23
2-7	Description of Flow Regions "i" and "o"	2-23
2-8	Actual Iterative Convergence to a Continuous Velocity Profile	2-27
2-9	Friction Factor Chart for Various Values of b and Re_v in the Region of Fully Developed Flow.	2-29
2-10	Dimensionless Shear for a Range of b and Re_v in Region "i" for Fully Developed Flow.	2-31
2-11	Dimensionless Shear for a Range of b and Re_v in Region "o" for Fully Developed Flow.	2-32
2-12	Plots of Wall Variables.	2-34
2-13	Eddy Diffusivity of Momentum Across the Annular Gap. . . .	2-35
3-1	Entrance Configurations Used in Reference 21	3-3
3-2	Local Pressure Gradients (from Reference 21)	3-4
3-3	Entrance Configurations Used in Reference 22	3-6
3-4	Axial Development of Velocity Profiles with Square and Round Entrances (from Reference 22).	3-7
3-5	Comparisons of Experimental Drag Coefficients of Principal Investigators (from Reference 6)	3-9
3-6	Velocity Profiles Predicted in Reference 4 Compared with Data of Reference 22 (from Reference 22).	3-11

LIST OF ILLUSTRATIONS (Cont'd)

Figure		Page
3-7a	Control Volume Used to Predict Location of First Velocity Profile Within Region "1" Boundary Layer. . .	3-14
3-7b	Forces on Control Volume	3-14
3-8	Assumed Linear Streamline Growth	3-17
3-9	Control Volume of Annular Gap.	3-21
3-10	Control Volume Used to Locate Successive Velocity Profiles Within Region "1" Boundary Layer	3-23
3-11a	Comparison of Developing and Fully Developed Velocity Profiles from Present Simulation	3-30
3-11b	Developing Velocity Profile in the Entrance Region Predicted in Reference 17	3-30
3-12	Comparison of Experimental Results from Reference 6 and Present Theory	3-31
3-13	Example of Computed Velocity Profiles for Developing Flow Model	3-33
3-14	Wall Shear Stress Development.	3-34
3-15	Pressure Signature in the Annulus for Developing Flow . .	3-36
3-16	Pressure Signature of Present Method Compared with That from Irrotational Assumption.	3-36
3-17	Friction Factors in Region of Developing Flow	3-38
3-18	Core Velocity Growth in Region of Developing Flow.	3-38
3-19	Friction Factors for Various Values of b and Re_v in the Region of Developing Flow	3-39
3-20	Dimensionless Average Shear Stress on Vehicle for Developing Flow.	3-40
3-21	Dimensionless Average Shear Stress on Tube for Developing Flow.	3-41
3-22	Entry Length for Various Values of b and Re_v	3-42
A-1	Scheme for Determining Vehicle Drag in Fully Developed Flow	A-2

LIST OF ILLUSTRATIONS (Cont'd)

Figure		Page
D-1	Scheme for Determining Vehicle Drag in Developing Flow . .	D-2
D-2	Procedure for Choosing δ_{in}^+ for the Developing Flow Analysis.	D-4

LIST OF TABLES

Table		Page
2-1	Values of the Parameters Used to Generate Figure 2-4 . . .	2-10
2-2	Polynomial Fit of Data from Table 2-1.	2-11
3-1	Resultant Dot Product on Control Volume Surfaces	3-15
G-1	Entry Region Result for $U_v = 40$ ft/s, $r_i = 10.5$ in., $r_o = 12.0$ in	G-1
G-2	Volume Flux for Profiles Shown in Figure 3-11.	G-1

LIST OF SYMBOLS

a	r_{mt}/r_i
a_{hg}	$(r_o - r_i)/2$
A_a (ft ²)	Cross-sectional area of annulus
A_s (ft ²)	Surface area of concentric portion of vehicle within tube
A_t (ft ²)	Cross-sectional area of tube
A_v (ft ²)	Frontal area of vehicle
b	Radius ratio r_o/r_i
C_{nt}	Nose coefficient from Hoerner (see figures 3-5 and H-1)
D_h (ft)	Hydraulic diameter $2(r_o - r_i)$
f_d	Darcy friction factor, $f_d = 4f_f$
f_f	Fanning friction factor, equation (2-37)
f_{fd}	Friction factor for fully developed flow
f_e	Friction factor for developing flow
g (32.174 ft/s ²)	Gravitational acceleration
g_c (32.174 lb _m *ft/lb _f s ²)	Gravitational constant
h_f (ft)	Irreversible flow loss, equation (2-39)
L_v (ft)	Total length of concentric portion of vehicle within tube
L^* (ft)	Developing length of concentric portion of annulus
L_n (ft)	Axial nose length, figure 3-12
p (lb _f /ft ²)	Pressure in annulus
Q_c (ft ³ /s)	Volume flux through inviscid core
Q_i (ft ³ /s)	Volume flux through region "i" boundary layer
Q_{in} (ft ³ /s)	Volume flux entering the annulus
Q_o (ft ³ /s)	Volume flux through region "o" boundary layer
Q_t (ft ³ /s)	Total volume flux in developing flow portion of annulus
Re_b	Reynolds number based on core bulk velocity and hydraulic diameter
Re_{in}	Reynolds number based on bulk velocity of fluid approaching the annulus and tube radius

LIST OF SYMBOLS (Cont'd)

Re_v	Vehicle Reynolds number $U_v r_i / \nu$
$r_{\delta i}$ (ft)	Radius of boundary layer edge from vehicle centerline for region "i"
r_i (ft)	Vehicle radius
r_i^+	Dimensionless vehicle radius
r_{me} (ft)	Radius at which maximum velocity occurs for a given profile during laminar flow
r_{mt} (ft)	Radius at which maximum velocity occurs for a given profile during turbulent flow
r_o (ft)	Tube radius
$r_{\delta o}$ (ft)	Radius of boundary layer edge from vehicle centerline for region "o"
r_o^+	Dimensionless tube radius
S	Reciprocal of radius ratio b
T (°F)	Bulk temperature of fluid
U_b (ft/s)	Bulk velocity of annular fluid
$U_{\delta i}$ (ft/s)	Velocity at edge of region "i" boundary layer
$U_{\delta o}$ (ft/s)	Velocity at edge of region "o" boundary layer
U_{in} (ft/s)	Bulk velocity of fluid entering the annulus
u_i	Local velocity in boundary layer of region "i"
u_i^+	Dimensionless local velocity in boundary layer of region "i"
u_i^* (ft/s)	Friction velocity for region "i" boundary layer calculations
u_o (ft/s)	Local velocity in boundary layer of region "o"
u_o^+	Dimensionless local velocity in boundary layer of region "o"
u_o^* (ft/s)	Friction velocity for region "o" boundary layer calculations
U_v (ft/s)	Simulated vehicle velocity

LIST OF SYMBOLS (Cont'd)

x (ft)	Axial distance from concentric annular entrance
y_i (ft)	Local distance from vehicle wall within region "i" boundary layer
y_{li} (ft)	Height of sublayer within region "i" boundary layer
y_i^+	Dimensionless y_i
y_{li}^+	Dimensionless y_{li}
y_o (ft)	Local distance from the tube wall within region "o" boundary layer
y_o^+	Dimensionless y_o
y_{lo} (ft)	Height of sublayer in region "o" boundary layer
y_{lo}^+	Dimensionless y_{lo}
ϵ_m	Eddy diffusivity of momentum
δ_i	Region "i" boundary layer height
δ_o	Region "o" boundary layer height
κ	Von Kármán's constant (0.36)
μ	Viscosity
ν	Kinematic viscosity (μ/ρ)
π	3.14159
ρ	Density
τ	Shear stress
τ_i	Shear stress on vehicle
τ_i^*	Dimensionless τ_i , equation (2-45)
τ_o	Shear stress on tube
τ_o^*	Dimensionless τ_o , equation (2-45)
τ_w	Shear stress on wall

SUBSCRIPTS

B	Evaluated at base of vehicle
δ	Evaluated at edge of boundary layer
fd	From fully developed flow analysis
e	From developing (entry) flow analysis
i	Region "i"
li	Region "i" sublayer
2i	Region "i" turbulent layer
ℓ	Limit of sublayer
M	Value taken from Moody chart
mi	Maximum velocity in region "i"
$m\ell$	Maximum velocity for laminar flow
mo	Maximum velocity in region "o"
N	Evaluated over nose of vehicle
o	Region "o"
lo	Region "o" sublayer
2o	Region "o" turbulent layer

SUPERSCRIPTS

-	Time mean or integrated average
*	Dimensionless quantity when used with τ , equation (2-45)
+	Law-of-the-wall quantity in turbulent shear layer

AERODYNAMIC DRAG OF CYLINDRICAL VEHICLES MOVING CONCENTRICALLY WITHIN LONG TUBES

1. INTRODUCTION

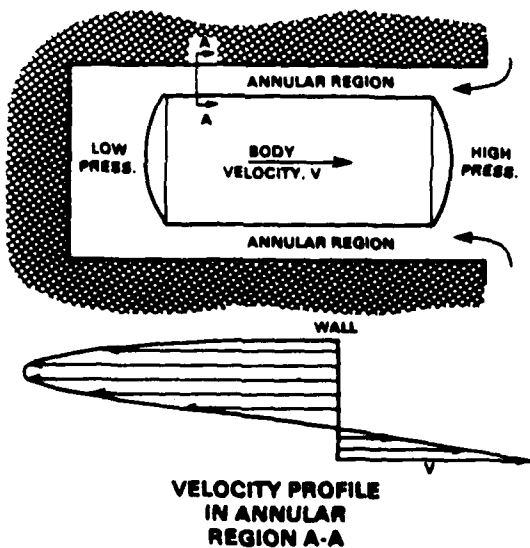
The objective of this study is to model the flow field in the annular region between a moving cylindrical vehicle and a concentric tube. The results of the analysis may be applied to both the swimout and impulse launch methods (figure 1-1). These methods are typically used by the Navy in launching various projectiles. The figure shows the associated velocity profiles in the annulus for each launch method. For swimout launch, the direction of fluid motion is opposite that of the vehicle, which gives rise to shear stresses that oppose the motion of the vehicle. During impulse launch, however, the annular profile shows that the fluid moves in the same direction as the vehicle, and the shear stresses aid launch.

Figure 1-2 shows the cylindrical vehicle during swimout, the vehicle having moved from the initial position x to some new position, $x + dx$. The vehicle displaces a quantity of fluid that must accelerate through the annular gap to fill the void created at the rear of the vehicle. The shear stresses resist vehicle motion and become more pronounced with increasing vehicle speeds and decreasing annular gaps.

For the alternate scenario of impulse launch, the fluid is forced through the annulus from the rear of the cylinder. The shear stresses pull the vehicle along the direction of flow. Since a high-pressure region exists behind the cylinder relative to the forward end, a force imbalance exists that consequently induces vehicle movement. As gap clearances become small, the following events occur that aid the impulse launch:

1. Annular fluid velocities increase, magnifying the wall shear stresses.
2. The volume flux of blowby decreases, resulting in a larger pressure differential across the vehicle.

a. SWIMOUT LAUNCH



b. IMPULSE LAUNCH

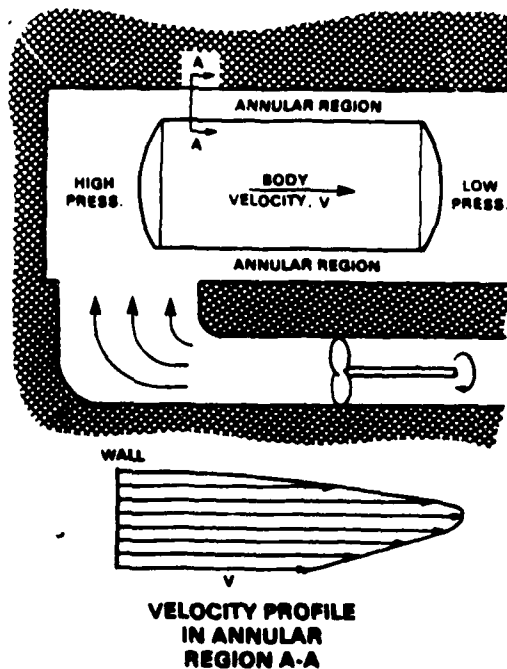


Figure 1-1. Launch Methods

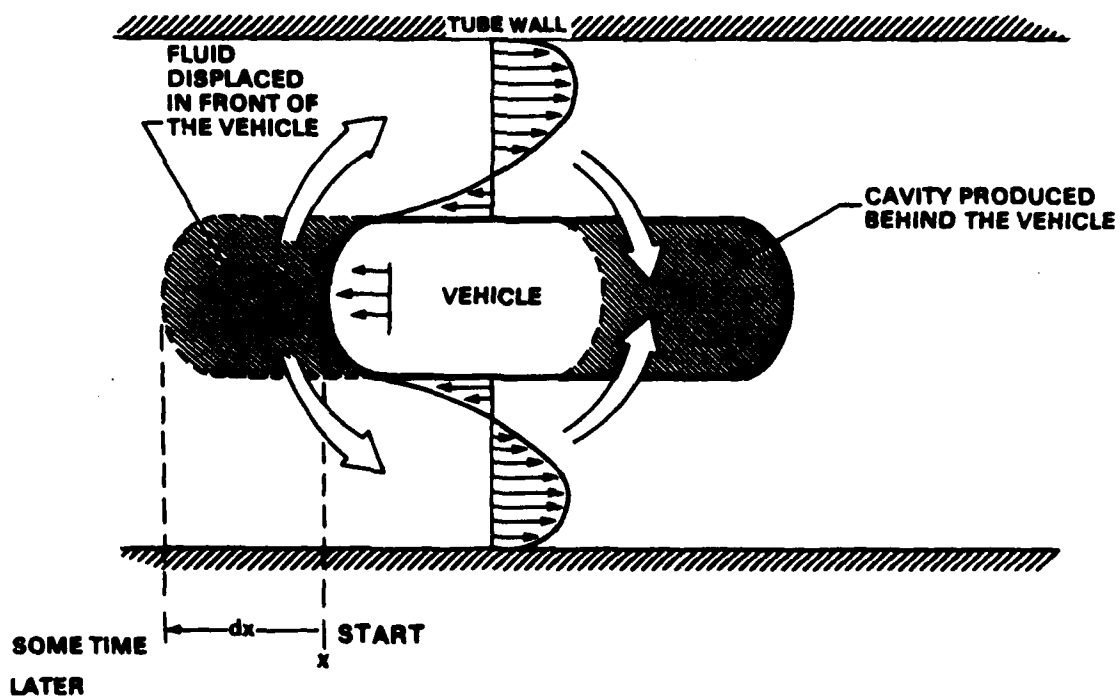


Figure 1-2. Description of the Mass Continuity

Experimental efforts to understand turbulent annular tube flow were reported as early as 1907 (reference 1). In 1968, reference 2 documented the successful prediction of friction factors for fully developed, turbulent annular tube flow. The theoretical results presented were for the range $6000 < Re_b < 4.5 \times 10^4$, for six radius ratios ranging from 1.05 to 50.* Deissler's equation was used to model the eddy diffusivity and obtain velocity profiles for the sublayer, while Von Kármán's similarity hypothesis was used to obtain profiles in the turbulent layer. The combined use of these two equations resulted in reasonable agreement with the experimental results previously obtained by Quarmby in reference 3. Then, in 1971, a model was developed for the hydrodynamic boundary layer growth in the entry region for annular tube flow using the momentum integral technique (reference 4). The velocity profiles were determined by the use of Reichardt's expression for eddy diffusivity, and were adjusted for calculations near the wall by implementation of Van Driest's damping factor.

In 1981, the successful analytical models of references 2 and 4 were combined and extended to include a moving boundary (that is, a vehicle moving within a concentric tube) as reported in reference 5. The predicted vehicle drag coefficient was 16 percent lower than the experimental results of previous investigations, as compiled by Davidson in reference 6. Davidson reduced and correlated these results to a common plot of drag coefficient based on vehicle speed versus the area blockage ratio. In reference 5, Sud and Chaddock stated that neglect of entrance effects and the use of a simplified model for the wake region in their analysis may have contributed to the discrepancy between their results and the correlation of Davidson.

The calculations of Sud and Chaddock were limited to a single tube/vehicle radius ratio for two Reynolds numbers. The analytical approach and general iterative scheme of this present study are nearly identical to those used by Sud and Chaddock. In the present effort, however, two major improvements were implemented that have been developed through exhaustive numerical experimentation. These improvements consist of curve fits to estimate the

*Symbols are defined in the "List of Symbols," p. vi.

initial parameter values and a series of weighted linear interpolations to steer the iteration process. These techniques enable convergence to a solution for a wide range of Reynolds numbers, $10^4 \leq Re_v \leq 10^7$, and radius ratios, $1.01 \leq b \leq 2.0$, while keeping the volume flux constant within 0.01 percent. Additional techniques were developed for solving the developing flow problem. These are discussed under "Analytical Survey" in section 3 of this report.

2. ANALYSIS OF FULLY DEVELOPED FLOW

EXPERIMENTAL SURVEY

Steady, fully developed annular tube flow was experimentally investigated as early as 1907 (reference 1). Since that time, many investigators have conducted experiments to characterize this flow because it occurs frequently in heat exchangers. Of those investigators, some found that $r_{mt}/r_{m\ell} > 1$, whereas others found that $r_{mt}/r_{m\ell} < 1$. This particular characteristic is perhaps the most controversial. These quantities are depicted in figure 2-1.

More recent results (reference 7) confirm those investigators who found $r_{mt}/r_{m\ell} < 1$, which now seems to be the generally accepted result. Consequently, only references 3, 8, 9, and 10 will be discussed in this survey.

In reference 8, the flow of air was measured through two annuli, namely $b = 6.17$ and 1.54 for $4000 < Re_b < 22,000$. The authors found $r_{mt}/r_{m\ell} \approx 1$ for all but $Re_b = 1820$ with $b = 6.17$. Velocities at points beyond r_{mt} (near the tube) were found to agree with the laminar correlations of reference 11, unlike velocities below r_{mt} .

In reference 9, flow of air was measured through annuli in which b ranged from 2 to 5.2 for $10,000 < Re_b < 150,000$. The investigators arrived at the following correlation for r_{mt} :

$$\frac{r_{mt}}{r_o} = \frac{b^{n-1} + 1}{b^n + 1}, \quad n = 0.343,$$

from which modified logarithmic correlations were obtained for describing velocity profiles. Reference 3 indicates that reasonable agreement was obtained with the data of references 12 and 13 for $r_{mt}/r_{m\ell} < 1$.

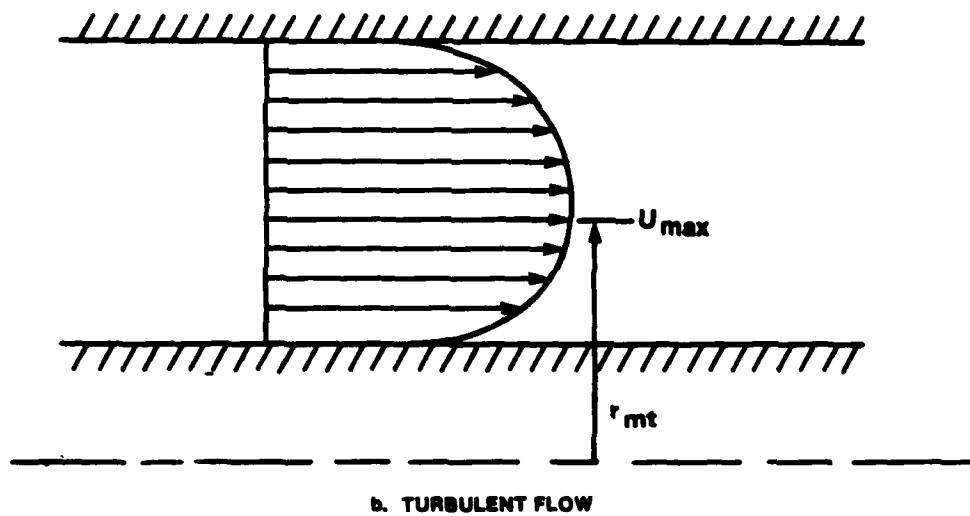
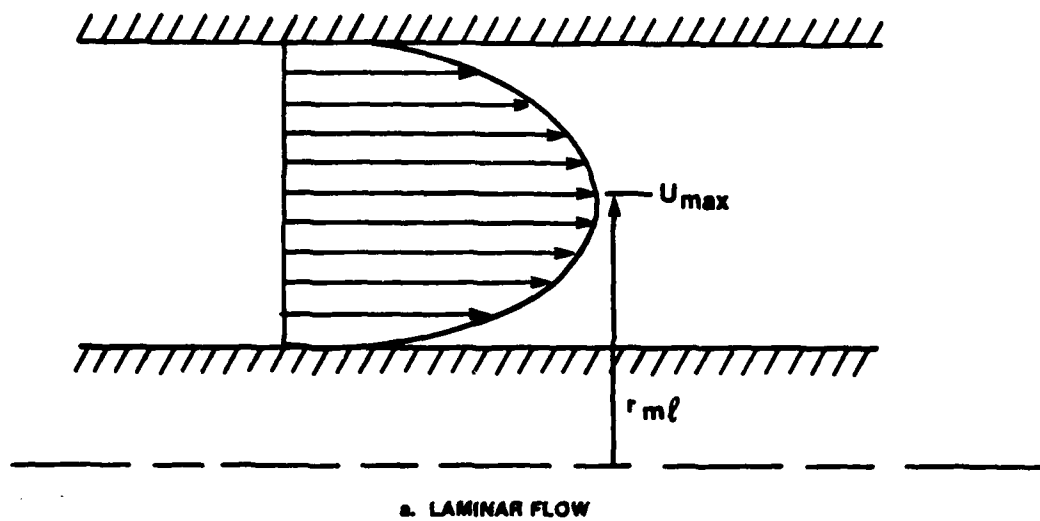


Figure 2-1. Depiction of r_{mt} , r_{ml} for Fully Developed Flow Through Concentric Annuli

The experimenters in reference 10 used air to test the flow through annular pipes, with 7 radius ratios in the range of $1.78 < b < 16$ for the range $47,000 < Re_b < 327,000$. Friction factors were found to be between 1 and 10 percent above pipe flow data, with little dependence on b . The authors concluded that friction factors are independent of Reynolds numbers for the range of radius ratios and Reynolds numbers tested.

According to reference 9, the experiments reported in references 12 and 13 were performed with great care. Reference 12 found $r_{mt}/r_{mf} < 1$ for Reynolds numbers around 250,000 with b as large as 19. The working fluid was water. Reference 13 presented data for Reynolds numbers from 10,000 to 70,000 for air, and for the radius ratio of 1.845.

Reference 3 tested three radius ratios: 2.88, 5.62, and 9.37 for a Reynolds number range from 6000 to 90,000, using air as the working fluid. The author found the difference between r_{mt} and r_{mf} to be a function of both Reynolds number and radius ratios for $40,000 < Re_b < 50,000$, and to be a function of b only for larger values of Re_b . Friction factors were found to be nearly independent of radius ratios, and were closer to plain tube experimental results than those of reference 10.

In reference 7, three annuli with radius ratios of 2.53, 5.68, and 11.36 were tested for the Reynolds number range from 20,000 to 300,000. Friction factors were found to be 8.5 percent above pipe flow for $b = 11.36$ and only 5 percent higher for the ratios 3.53 and 5.68. It was also found that a considerable portion of the boundary layer associated with the outer wall could be modeled using the law-of-the-wall. The profiles within the inner boundary layer could be described using modified law-of-the-wall relations for $b = 2.53$ and 5.68. However, for $b = 11.36$, law-of-the-wall relations could not be deduced.

ANALYTICAL SURVEY

In reference 2, Quarmby disagreed with Tomotika and Imai (reference 14), who found $r_{mt}/r_{mf} > 1$, and stated further that all other investigators known

to him found $r_{mt}/r_{me} < 1$, with the exception of those in reference 8, who found the ratio r_{mt}/r_{me} to be either less than or equal to unity (for low Re_b). Quarmby used the Von Kármán similarity hypothesis and Deissler's expression for eddy diffusivity to obtain turbulent layer and sublayer velocity profiles, respectively. His analytical results compared well with his experimental results in reference 3 for $6000 < Re_b < 45,000$, with $1.05 < b < 50$.

In reference 15, Quarmby further investigated the Re_b effect on $u^+(y^+)$ profiles for the limiting cases of parallel plate and circular tube flows. He corrected deficiencies in his earlier analytical model (reference 2) where the shear stress was assumed uniform across the duct, which is analogous to neglecting the molecular viscosity. Further, the condition of a zero profile gradient at r_{mt} previously unfulfilled in reference 2 was also corrected. When modifications of reference 15 were applied to Deissler's and Von Kármán's equations for eddy diffusivity, good agreement was found with the experimental results of reference 16 for the limiting cases of plain tube and parallel plate channel flows.

Up to this point of the survey, no provisions had been made by any investigator to include the effects of a moving wall in annular tube flows. Sud and Chaddock (reference 5) used Quarmby's modification in the sublayer (reference 15) and the turbulent layer expressions of reference 2 in the extended problem of a vehicle moving concentrically within a tube. Good agreement was found with reference 3 for the generic case of no moving boundaries. As mentioned in section 1, reference 5 also compared well with reference 6. In view of the success of Quarmby and Sud and Chaddock, and the fact that their analyses were physically the most fundamental, an approach similar to that of reference 5 was used in this study.

ASSUMPTIONS AND BOUNDARY CONDITIONS

In this study, the vehicle was assumed to move within the concentric tube at a constant velocity. As in reference 5, the analysis was simplified

by attaching the coordinate system to the vehicle surface just aft of the nose section, thus making the flow field within the annulus appear steady (figure 2-2). If the coordinate system were attached to the tube, the flow field observed would change with the vehicle's passage, and the following sequence of events would occur. As the vehicle approaches the coordinate location, a pressure rise would occur. During the vehicle's passage, annular effects would be present. Finally, as the rear of the vehicle crosses the coordinate location, the pressure would drop rapidly, leading into wake effects. These events would be time-dependent and would add unnecessary complications to the analysis if included as a result of coordinate placement. Because the coordinate system was attached to the vehicle surface, the tube appears to be moving. Figure 2-3 shows how the velocity profile would be interpreted by virtue of coordinate placement on either tube or vehicle wall. Note that the shapes of these velocity profiles are in fact identical, with the exception of the position of the zero velocity vector and consequently the total volume flux.

The velocity profile at the annular entrance was assumed uniform. This is a reasonable assumption provided the boundary layers are initially turbulent and the vehicle nose is well rounded, as discussed in reference 4. Entrance profiles are actually nonuniform because of boundary layer growth on the vehicle nose section and may result in larger drag estimates if properly accounted for. This is especially true for blunt nose vehicles where separation is likely to occur. The following assumptions were made:

1. Steady flow is present, i.e., $d\bar{v}/dt = 0$.
2. There is a uniform velocity profile at the annular entrance. This is a reasonable assumption provided a rounded nose section is being modeled and the boundary layers are turbulent from the start (reference 4). At $x = 0.0$, $u = U_{in}$ for all y .
3. Annular fluid is incompressible with constant ρ .
4. There is no blowing or suction at the walls. Therefore, $u(r)$ only... (no blowing or suction $v = 0.0$).
5. Radial pressure variations are negligible.
6. The tube moves with constant velocity.

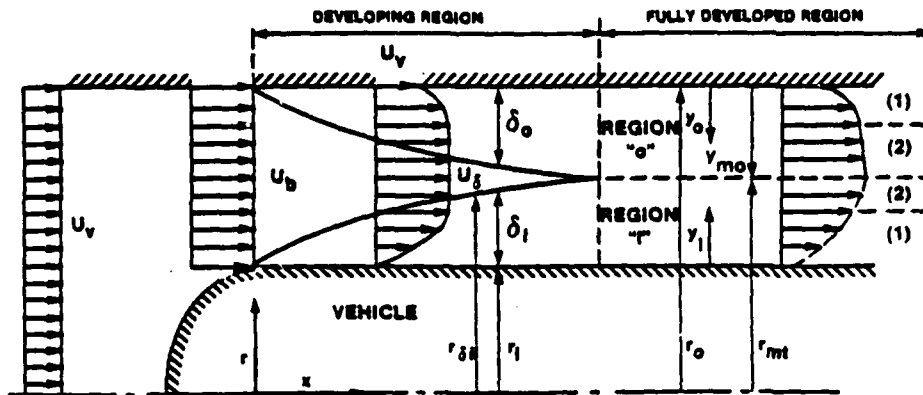


Figure 2-2. Velocity Development of Fluid in Annular Region

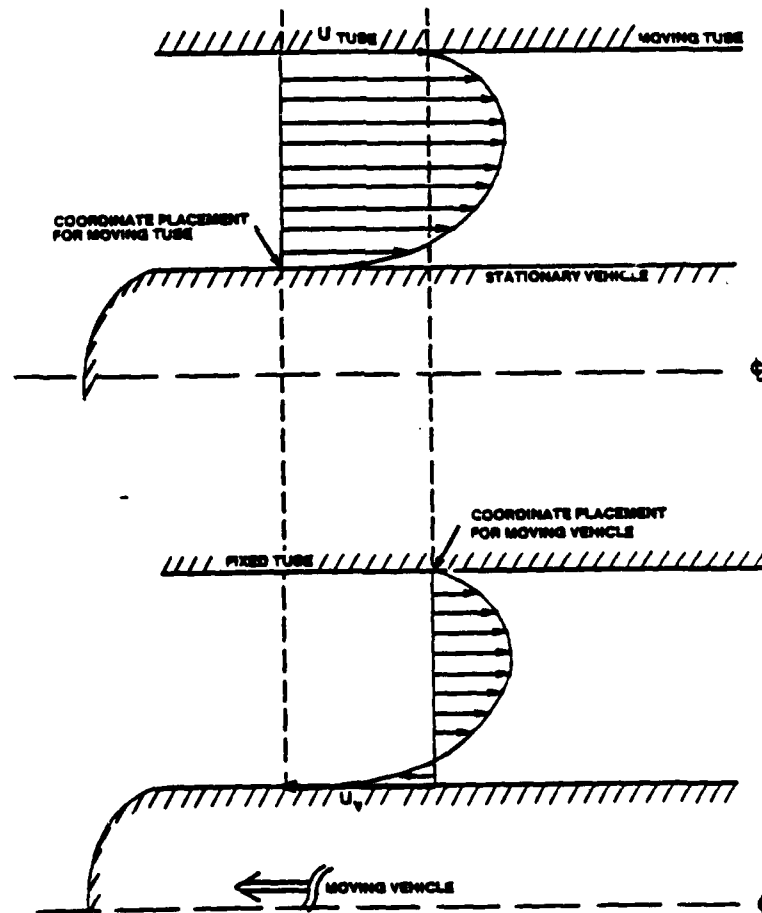


Figure 2-3. Profile Analogy Between Moving Tube and Moving Vehicle

The boundary conditions applied are:

1. At $r = r_{mt}$, $(du/dy)_i = (du/dy)_o = 0.0$.
2. At $r = r_i$, $u = U_v = 0.0$ (stationary vehicle).
3. At $r = r_o$, $u = U_{tube}$ (moving tube).
4. At $r = r_{mt}$, $U_{mo} = U_{mi}$.

Boundary condition no. 1 is consistent with physical intuition. The slopes of the velocity profile for region "i" and region "o" must be the same at $r = r_{mt}$ with no sharp gradients or discontinuities; furthermore, the slopes of the velocity profiles at this location must be zero.

DETERMINATION OF VELOCITY PROFILES

Figure 2-2 shows an enlarged view of the annular region. The portion of the flow field from where the boundary layers start to the point where they meet is termed the entry region or developing region. Velocity profiles are functions of axial location from the throat up to this meeting point. Downstream of the merged boundary layers, the velocity profiles no longer change with axial location. This region is termed fully developed. The fluid that enters the annular core accelerates up to the end of the entry region. Once in the fully developed region, annular velocities have reached their largest values, with a maximum value of any profile occurring at $r = r_{mt}$.

The analysis was dependent on determining the velocity profiles, which were generated by implementing a two-layer model. Deissler's equation for eddy diffusivity of momentum was used to obtain profiles in the sublayer where viscous shear is dominant. The eddy diffusivity in the turbulent layer, which extends beyond the sublayer to the point of maximum velocity at $r = r_{mt}$, was modeled by employing Von Kármán's similarity hypothesis. As previously mentioned, this two-layer approach has produced friction factors that are in good agreement with experiments.

In turbulent theory, properties are generally represented in terms of a time-averaged component and a fluctuating component, such as $u = \bar{u} + u'$, where the time-averaged quantity \bar{u} is defined by

$$\bar{u} = \frac{1}{T} \int_0^T u \, dt .$$

The quantity T is the integration interval usually chosen to be larger than any significant time period of the fluctuations u' . In this study, the fluctuating components were not included so that a mathematical solution would be possible. Average values generally yield sufficiently accurate results (reference 17). Throughout the analysis, all properties will actually be their averaged components.

In a one-dimensional turbulent flow field, the total apparent shear stress (molecular + turbulent) may be represented by

$$\tau = \rho (\nu + \epsilon_m) \frac{du}{dy} , \quad (2-1)$$

where $\nu \gg \epsilon_m$ in the sublayer close to the wall, and $\epsilon_m \gg \nu$ in the turbulent layer.

Nondimensional variables (wall coordinates) were used to generalize the analysis. The friction velocity is defined as

$$u^* = (\tau_w / \rho)^{1/2} . \quad (2-2a)$$

The following dimensionless groups were formed:

$$u^+ = u / u^* , \quad (2-2b)$$

and

$$y^+ = y u^* / \nu . \quad (2-2c)$$

Equation (2-1) was nondimensionalized by making use of equations (2-2) giving

$$\tau/\tau_w = (1 + \varepsilon_m/\nu) du^+/dy^+ . \quad (2-3)$$

Deissler's first-order empirical equation for eddy diffusivity of momentum in dimensionless form is

$$\varepsilon_m/\nu = n^2 u^+ y^+ [1 - \exp(-n^2 u^+ y^+)] \text{ for } (0.0 < y^+ < y_\ell^+) . \quad (2-4)$$

The $u^+(y^+)$ relationship for the sublayer is then the combination of equations (2-3) and (2-4), which gives the first-order ordinary differential equation

$$du^+/dy^+ = \frac{\tau/\tau_w}{1.0 + n^2 u^+ y^+ [1.0 - \exp(-n^2 u^+ y^+)]} \quad (\text{sublayer}) . \quad (2-5)$$

This relationship holds well for both plain tube and parallel plate channel flows if the $y_\ell^+(Re_b)$ and $n^2(y_{mt}^+)$ dependence from reference 15 is used (figure 2-4). A polynomial fit of these data was made so that the $y_\ell^+(Re_b)$ and $n^2(y_{mt}^+)$ dependence shown in figure 2-4 could be included in equation (2-5). See tables 2-1 and 2-2.

The index n^2 in equation (2-5) is a damping factor obtained from plain tube experiments; it accounts for the presence of the wall on turbulence. Including this $n^2(Re_b)$ relation causes the sublayer thickness to increase more rapidly with decreasing Re_b than if a fixed value of n^2 was used. This implies that the turbulent viscosity is made less significant compared with the molecular viscosity when Re_b decreases so that the laminar $u^+ = y^+$ relation is approached (reference 15).

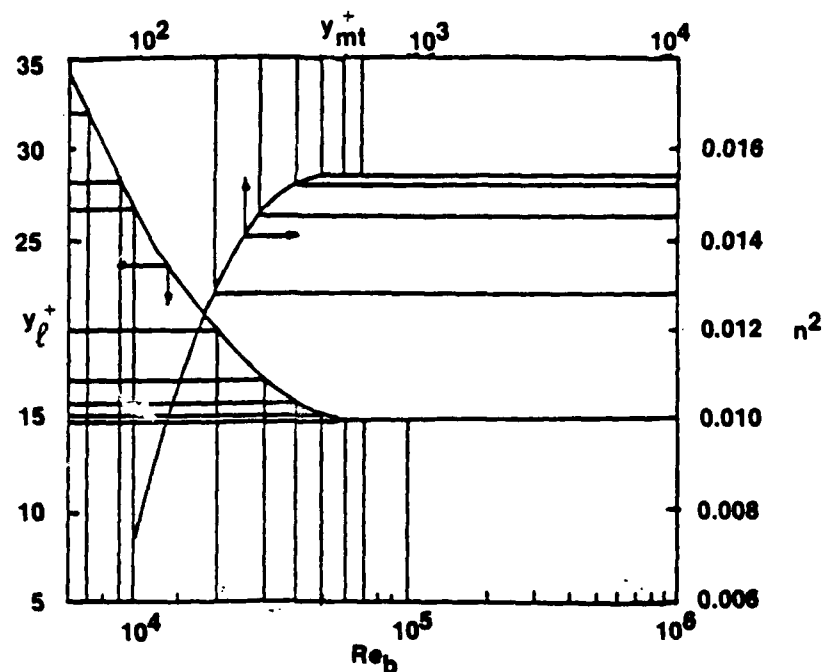


Figure 2-4. Relationships Between y_l^+ and Re_b and Between n^2 and y_{mt}^+
(from Reference 15)

Table 2-1. Values of the Parameters Used to Generate Figure 2-4

y_{mt}^+	n^2	n^2	Re_b	y_l^+	y_l^+
	Data	Curve Fit		Data	Curve Fit
110	0.008	0.0082	7005	32	32.2
144	0.0106	0.0104	9121	28	28
265	0.0140	0.0136	17536	21.5	21.6
297	0.0145	0.0142	36551	16.5	16.4
510	0.0154	0.0154	53225	15	14.9
705	0.0154	0.0154	154455	15	15
1800	0.0154	0.0154			
2500	0.0154	0.0154			
8200	0.0154	0.0154			

Table 2-2. Polynomial Fit of Data from Table 2-1

$Re_b < 20,000$	$y_\ell^+ = -0.6914 \times 10^{-2} Re_b + 0.4103 \times 10^{-6} (Re_b)^2 - 0.8668 \times 10^{-11} (Re_b)^3 + 63.4614$
$20,000 < Re_b < 50,000$	$y_\ell^+ = -0.4339 \times 10^{-3} Re_b + 0.3822 \times 10^{-8} (Re_b)^2 + 27.1373$
$Re_b > 50,000$	$y_\ell^+ = 15.0$
$y_{mt}^+ < 205$	$n^2 = 0.1408 \times 10^{-3} y_{mt}^+ - 0.2922 \times 10^{-6} (y_{mt}^+)^2 - 0.0038$
$205 < y_{mt}^+ < 510$	$n^2 = 0.1886 \times 10^{-4} y_{mt}^+ - 0.1709 \times 10^{-7} (y_{mt}^+)^2 + 0.1813 \times 10^{-11} (y_{mt}^+)^3 + 0.01003$
$y_{mt}^+ > 510$	$n^2 = 0.0154$

The Prandtl mixing length in conjunction with Von Kármán's similarity hypothesis yields the eddy diffusivity of momentum expression for the turbulent layer where

$$\ell = \kappa \left(\frac{du/dy}{d^2u/dy^2} \right), \quad \epsilon_m = \ell^2 (du/dy), \text{ and}$$

$$\kappa = 0.36 \text{ (Von Kármán's constant),}$$

giving

$$\epsilon_m = \left[\kappa \left(\frac{du/dy}{d^2u/dy^2} \right) \right]^2 du/dy. \quad (2-6)$$

Substitution of equation (2-6) into equation (2-3) gives the following $u^+(y^+)$ relation for the turbulent layer:

$$\frac{d^2u^+}{dy^{+2}} = \kappa \frac{(du^+/dy^+)^2}{(\tau/\tau_w - du^+/dy^+)^{1/2}} \quad (\text{turbulent layer}), \quad (2-7)$$

The value 0.36 for Von Kármán's constant was shown to yield good results for the limiting cases of parallel plate channel and pipe flow (reference 15).

For the region "i" sublayer, $0.0 \leq y_{1i}^+ \leq y_{1\ell}^+$, $n = n_i$, $\tau_w = \tau_i$, $y^+ = y_{1i}^+$. Equation (2-5) becomes

$$\frac{du_{1i}^+}{dy_{1i}^+} = \frac{\tau/\tau_i}{1 + n_i^2 u_{1i}^+ y_{1i}^+ \quad 1 - \exp(-n_i^2 u_{1i}^+ y_{1i}^+)}, \quad (2-8a)$$

where $u_{1i}^+ = 0.0$ at $y_{1i}^+ = 0.0$ (from boundary condition no. 2). In the

turbulent layer, $y_{1\ell}^+ \leq y_i^+ \leq y_{imt}^+$, equation (2-7) becomes

$$\frac{d^2 u_{2i}^+}{dy_{2i}^+} = \kappa \left[\frac{(du_{2i}^+/dy_{2i}^+)^2}{(\tau/\tau_i - du_{2i}^+/dy_{2i}^+)^{1/2}} \right], \quad (2-8b)$$

where $u_{2i}^+(y_{2i}^+) = u_{1i}^+(y_{1\ell}^+)$.

Equations (2-8) were integrated to obtain the velocity profiles for region "i" using a fourth-order Runge-Kutta routine as described in reference 18.

Equation (2-8a) is to be integrated from $y_{1i}^+ = 0.0$ to $y_{1i}^+ = y_{1\ell}^+$. The step sizes $H = y_{1\ell}^+/\text{ITER}$ and $H = y_{mt}^+/\text{ITER2}$ were used for the sublayer and turbulent layer calculations, respectively. A parametric study of $\text{ITER2}(\text{Re}_b, b)$ was performed to minimize computational time; from this study, figure 2-5 was generated and a curve fit determined. The expression for ITER2 proved to yield accurate velocities at $y = y_{mt}$ when compared with velocities resulting from very large values of ITER2 (see "Results" later in this section).

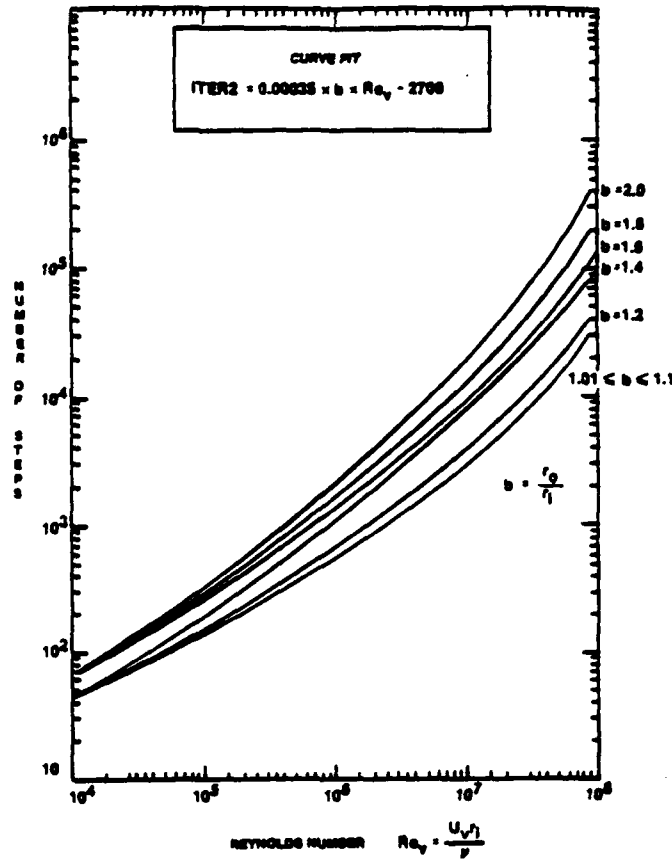


Figure 2-5. Suggested Number of Steps (in Runge-Kutta Routine) for Turbulent Region Calculations

At the end of the integration of equation (2-8a), a $u_{1i}^+(y_{1i}^+)$ profile would have been generated up to $y_{1\ell}^+$. At $y_{1i}^+ = y_{1\ell}^+$, the velocity u_{1i}^+ and the slope of the velocity profile du_{1i}^+/dy_{1i}^+ must be used as the initial values to integrate equation (2-8b).

A similar nondimensionalizing procedure was used to obtain differentiable equations necessary to produce velocity profiles in region "o." Equation (2-5) becomes (for the sublayer $0.0 \leq y_{10}^+ \leq y_{o\ell}^+$)

$$\frac{du_{10}^{+'}}{dy_{10}^{+'}} = \frac{\tau/\tau_o}{1+n_o^2 u_{10}^{+'} y_{10}^{+'} [1-\exp(-n_o^2 u_{10}^{+'} y_{10}^{+'})]} \quad (2-9a)$$

For the turbulent layer $y_{o\ell}^+ \leq y_{2o}^+ \leq y_{omt}^+$, where $u_{2o}^+(y_{2o}^+) = u_{1o}^+(y_{o\ell}^+)$, and equation (2-7) becomes

$$\frac{d^2 u_{2o}^+}{dy_{2o}^{+2}} = \kappa \left[\frac{(du_{2o}^+/dy_{2o}^+)^2}{(\tau/\tau_o - du_{2o}^+/dy_{2o}^+)^{1/2}} \right] \quad (2-9b)$$

For simplicity u_{1o}^+ was initially set equal to zero at $y_{1o}^+ = 0$. After equations (2-9) were integrated, the dimensionless tube velocity was accounted for by

$$u_{2o}^+ = u_{2o}^+ + U_{tube}^+.$$

The Runge-Kutta technique, used with equations (2-8), was similarly used to integrate equations (2-9) for region "o."

DERIVATION OF SHEAR STRESS RATIOS

Equations (2-8) and (2-9) were expressed in terms of the shear stress ratios τ/τ_i and τ/τ_o . These ratios vary across their respective boundary layers. A force balance across the annular gap was performed to find an expression for these ratios. This may be done only for the fully developed region since the flow is not accelerating. The following derivation was performed to find how these shear stress ratios vary with distance from the walls.

The continuity equation in cylindrical coordinates is

$$\frac{1}{r} (rv)_r + \frac{1}{r} w_\theta + u_x = 0,$$

where u_x , u_r , u_θ denote the partial derivatives of the axial velocity component with respect to x , r , θ , etc. The quantities v and w represent the radial and circumferential velocity components. Applying assumption no. 4 to the above equation gives

$$\text{CONTINUITY } u_x = 0. \quad (2-10)$$

The linear momentum equations in cylindrical coordinates are

$$r \text{ MOMENTUM } \frac{\partial v}{\partial t} + (\bar{v} \cdot \bar{v})v - \frac{w^2}{r} = -\frac{1}{\rho} \frac{\partial p}{\partial r} + g + v \left(\bar{v}^2 v - \frac{v}{r^2} - \frac{2}{r^2} w_\theta \right),$$

$$\theta \text{ MOMENTUM } \frac{\partial w}{\partial t} + (\bar{v} \cdot \bar{v})w + \frac{vw}{r} = -\frac{1}{\rho r} \frac{\partial p}{\partial \theta} + g + v \left(\bar{v}^2 w + \frac{2}{r^2} v_\theta - \frac{w}{r^2} \right),$$

$$x \text{ MOMENTUM } \frac{\partial u}{\partial t} + (\bar{v} \cdot \bar{v})u = -\frac{1}{\rho} \frac{\partial p}{\partial x} + g + v \bar{v}^2 u.$$

Applying assumptions 1, 3, and 4, and neglecting gravity terms,

$$r \text{ MOMENTUM } -\frac{1}{\rho} \frac{dp}{dr} = 0, \quad (2-11a)$$

$$\theta \text{ MOMENTUM } -\frac{1}{\rho} \frac{dp}{d\theta} = 0, \quad (2-11b)$$

$$x \text{ MOMENTUM } \frac{v}{r} \frac{d}{dr} \left(\frac{rdu}{dr} \right) - \frac{1}{\rho} \frac{dp}{dx} = 0. \quad (2-11c)$$

Integrating equation (2-11c) twice,

$$u = \frac{1}{\rho v} \frac{dp}{dx} \left(\frac{r^2}{4} + C_1 \log_e r + C_2 \right). \quad (2-12)$$

Applying boundary condition no. 1 across the gap, $r_i \leq r_{mt} \leq r_o$,

$$C_1 = -\frac{r_{mt}^2}{2} . \quad (2-13a)$$

Now applying boundary condition no. 2 for region "i" where $r < r_{mt}$,

$$C_2 = \frac{r_{mt}^2}{2} \log_e r_i - \frac{r_i^2}{4} ; \quad (2-13b)$$

but C_2 may also be found from boundary condition no. 3 for region "o" where $r > r_{mt}$:

$$C_2 = \frac{r_{mt}^2}{2} \log_e r_o + \rho v \frac{U_{tube}}{(dp/dx)} - \frac{r_o^2}{4} .$$

To simplify, assume $U_{tube} = 0.0$,

$$C_2 = \frac{r_{mt}^2}{2} \log_e r_o - \frac{r_o^2}{4} . \quad (2-13c)$$

Equations (2-13b) and (2-13c) were set equal, thus eliminating C_2 and resulting in the following expression for r_{mt} :

$$r_{mt} = \left[\frac{r_o^2 - r_i^2}{2 \log_e (r_o/r_i)} \right]^{1/2} . \quad (2-14)$$

To obtain an expression for the local velocity in region "o" where $r > r_{mt}$, equations (2-13a) and (2-13c) were substituted into equation (2-12), resulting in

$$u = \frac{1}{4\rho\nu} \frac{dp}{dx} \left[r^2 - r_o^2 + 2r_{mt}^2 \log_e(r_o/r) \right] . \quad (2-15)$$

From the definition of average velocity,

$$U_b = \frac{2 \int_{r_i}^{r_o} u r dr}{(r_o^2 - r_i^2)} . \quad (2-16)$$

Equation (2-15) was substituted into equation (2-16), and that equation was simplified to

$$U_b = \frac{-(dp/dx)}{8\rho\nu} (r_o^2) + r_i^2 - 2r_{mt}^2 . \quad (2-17)$$

Then the local velocity in terms of the average velocity for region "o" was obtained by combining equations (2-15) and (2-17), eliminating the dp/dx term.

$$u = \frac{-2U_b \left[r^2 - r_o^2 + 2r_{mt}^2 \log_e(r_o/r) \right]}{r_o^2 + r_i^2 - 2r_{mt}^2} . \quad (2-18)$$

Using the definition of shear stress, $\tau = -\mu \frac{du}{dr}$, equation (2-18) becomes

$$\tau = \frac{4\mu U_b (r^2 - r_{mt}^2)}{r (r_o^2 + r_i^2 - 2r_{mt}^2)} . \quad (2-19)$$

The ratio of local to tube shear stress can be found by using equation (2-19) and the fact that $\tau = \tau_o$ at $r = r_o$:

$$\frac{\tau}{\tau_0} = \frac{r_0 (r^2 - r_{mt}^2)}{r (r_0^2 - r_{mt}^2)} \quad (2-20a)$$

Equation (2-20a) must be expressed in terms of the dimensionless variables y_0^+ , y_{mo}^+ , r_0^+ , so that they may be inserted into equation (2-9), which can then be integrated.

Using the fact that

$$r = r_0 - y_0, \quad (2-20b)$$

$$r_{mt} = r_0 - y_{mo}, \quad (2-20c)$$

and the relations given by equations (2-2), where $\tau_w = \tau_0$, equation (2-20a) is transformed to the dimensionless form

$$\frac{\tau}{\tau_0} = \frac{r_0^+ \left[(r_0^+ - y_0^+)^2 - (r_0^+ - y_{mo}^+)^2 \right]}{r_0^+ - y_0^+ (r_0^{+2} - r_0^+ - y_{mo}^+)^2} \quad (2-20d)$$

A similar procedure was followed to obtain the dimensionless expression for τ/τ_i .

The local velocity for region "i" was found by combining equations (2-12), (2-13a), and (2-13b), giving

$$u = \frac{1}{4\rho v} \frac{dp}{dx} \left[r^2 - r_i^2 + 2r_{mt}^2 \log_e(r_i/r) \right] \quad (2-21)$$

From equations (2-16) and (2-21), the average velocity is

$$U_b = \frac{-(dp/dx)}{8\rho v} \left[(r_0^2 + r_i^2) - 2r_{mt}^2 \right] \quad (2-22)$$

Equations (2-21) and (2-22) were combined so that the local velocity u could be expressed in terms of U_b and the dp/dx term eliminated:

$$u = -2U_b \left[\frac{r^2 - r_i^2 + 2r_{mt}^2 \log_e(r_i/r)}{r_o^2 + r_i^2 - 2r_{mt}^2} \right]. \quad (2-23)$$

From the definition of shear stress, $\tau = -\mu du/dr$, and setting $\tau = \tau_i$ at $r = r_i$, equation (2-23) yields

$$\frac{\tau}{\tau_i} = \frac{r_i (r^2 - r_{mt}^2)}{r (r_i^2 - r_{mt}^2)}. \quad (2-24)$$

Using

$$r = r_i + y_i, \quad (2-25a)$$

$$r_{mt} = r_i + y_{mi}, \quad (2-25b)$$

and equations (2-2) where $\tau_w = \tau_i$ for region "i," the following relationship was obtained for region "i" in terms of the inner variables:

$$\frac{\tau}{\tau_i} = \frac{r_i^+ [(r_i^+ + y_i^+)^2 - (r_i^+ + y_{mi}^+)^2]}{(r_i^+ + y_{mi}^+) [r_i^{+2} - (r_i^+ + y_i^+)^2]}. \quad (2-25c)$$

The ratio τ_o/τ_i was found by first performing a force balance over the entire annular region and then on region "i." One cannot just simply use equations (2-20d) and (2-25c) to find τ_o/τ_i , since they were found by considering regions "i" and "o" separately. A force balance across the annular gap represented by the area enclosed within the dashed line of figure 2-6 yields

$$2r_o\tau_o + 2r_i\tau_i = -(r_o^2 - r_i^2) dp/dx . \quad (2-26a)$$

A force balance across region "i" represented by the shaded area in figure 2-6 gives

$$2r_i\tau_i = -(r_{mt}^2 - r_i^2) dp/dx . \quad (2-26b)$$

The dp/dx term was eliminated between equations (2-26a) and (2-26b), and the resulting expression for τ_o/τ_i was reduced to the following by making use of the definitions of a and b (see "List of Symbols"):

$$\frac{\tau_o}{\tau_i} = \frac{(b^2 - a^2)}{b(a^2 - 1)} . \quad (2-26c)$$

From equations (2-25b), (2-26c), and the definitions of a and b, the following expression for y_{mi}^+ in terms of a, b, and r_o^+ was found:

$$y_{mi}^+ = \frac{(a-1)}{b} \left[\frac{b(a^2-1)}{(b^2-a^2)} \right]^{1/2} r_o^+ . \quad (2-27)$$

From the dimensionless form of equations (2-14) and (2-20c),

$$y_{mo}^+ = (1 - a/b)r_o^+ . \quad (2-28)$$

The definitions of b, r_i^+ , r_o^+ , and equation (2-26c) were used to obtain the following expression for r_i^+ in terms of r_o^+ :

$$r_i^+ = \frac{1}{b} \left[\frac{b(a^2-1)}{(b^2-a^2)} \right]^{1/2} r_o^+ . \quad (2-29)$$

From equation (2-2a), the dimensionless velocities at $r = r_{mt}$ are

$$U_{mo}^+ = \frac{U_{mo}}{\sqrt{\tau_o/\rho}} \quad (2-30a)$$

$$U_{mi}^+ = \frac{U_{mi}}{\sqrt{\tau_i/\rho}} \quad (2-30b)$$

The following relationship was found from boundary condition no. 4 and equations (2-30) and (2-26c):

$$a = \left[\frac{b \left[b \left(U_{mo}^+ / U_{mi}^+ \right)^2 + 1 \right]}{b + \left(U_{mo}^+ / U_{mi}^+ \right)^2} \right]^{\frac{1}{2}} \quad (2-31)$$

DERIVATION OF REYNOLDS NUMBER FOR CONTINUITY CHECK

To ensure constant volume flux, the bulk velocity or Reynolds number for the generated velocity profile at $x = L^*$ must match its value at the throat of the annulus.

From the definition of bulk velocity and equations (2-2),

$$U_{bi} = \frac{2v}{r_i^+ r_i (b^2 - 1)} \int_{r_i^+}^{r_{mt}^+} u_i^+ r^+ dr^+ \quad (2-32a)$$

$$U_{bo} = \frac{2vb^2}{r_o^+ r_o (b^2 - 1)} \int_{r_{mt}^+}^{r_o^+} u_o^+ r^+ dr^+ \quad (2-32b)$$

The quantities U_{bi} and U_{bo} are the bulk velocities within region "i" and region "o," respectively (figure 2-7). The quantities $u_i^+(r^+)$ and $u_o^+(r^+)$ are determined from the integration of equations (2-8) and (2-9), respectively.

From the definition of Reynolds number,

$$Re_b = \frac{(U_{bi} + U_{bo}) D_h}{v} = \frac{4}{(b+1)} \left[\underbrace{\frac{1}{r_i^+} \int_{r_i^+}^{r_{mt}^+} u^+ r^+ dr^+}_{\text{Part 1}} + \underbrace{\frac{b}{r_o^+} \int_{r_{mt}^+}^{r_o^+} u^+ r^+ dr^+}_{\text{Part 2}} \right] \quad (2-33)$$

Equations (2-25) were used to convert part 1, and equations (2-20) were used to convert part 2, to local wall variables y_i^+ and y_o^+ . The following expression resulted:

$$Re_b = \left[\frac{4}{(b+1)} \underbrace{\frac{1}{r_i^+} \int_0^{y_{mi}^+} u^+ (r_i^+ + y_i^+) dy_i^+}_{\text{Part 1}} + \underbrace{\frac{b}{r_o^+} \int_0^{y_{mo}^+} u^+ (r_o^+ - y_o^+) dy_o^+}_{\text{Part 2}} \right] \quad (2-34)$$

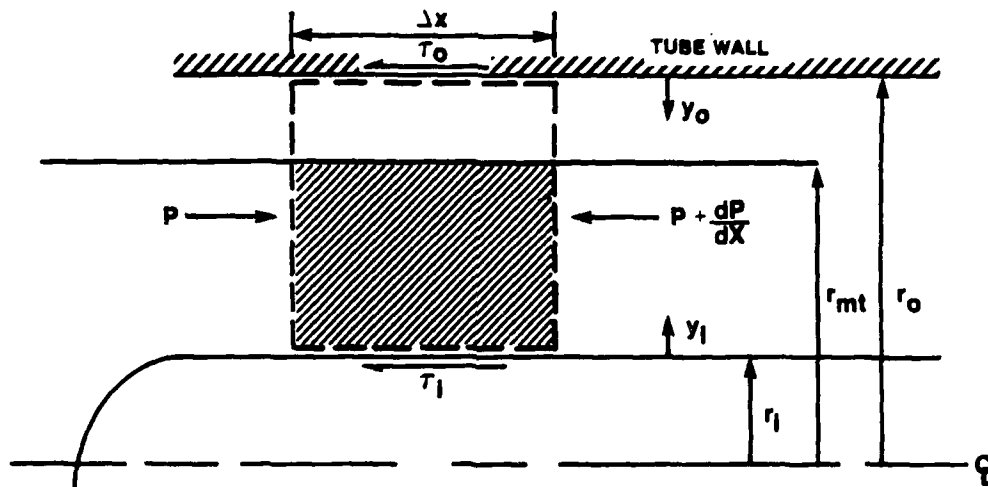


Figure 2-6. Force Balance Over Entire Annular Segment

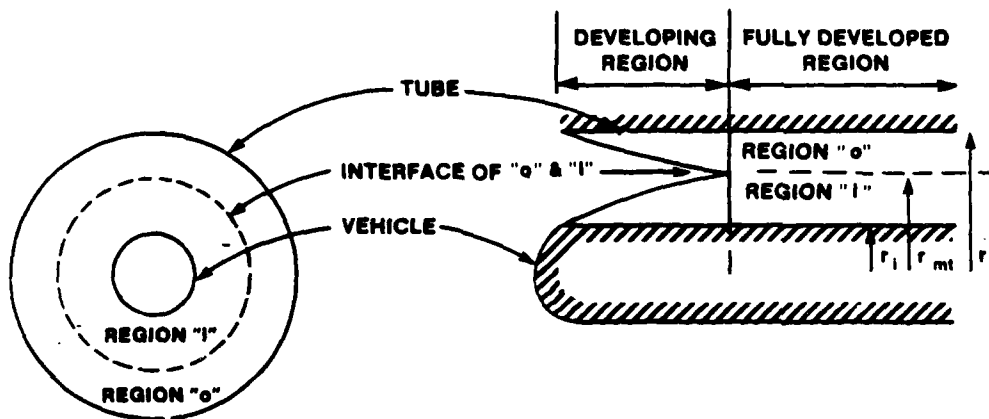


Figure 2-7. Description of Flow Regions "i" and "o"

Equation (2-34) was used to compute the bulk velocity in order to perform the continuity check and ensure constant volume flux. Due to the smaller size of U_b relative to Re_b , U_b was used to check continuity using the following expression:

$$U_b = \frac{Re_b \nu}{D_h} \quad (2-35)$$

DERIVATION OF FRICTION FACTOR AND DRAG EQUATIONS

The goal is to determine the drag force, which acts to oppose the motion of the vehicle. However, as an intermediate step, friction factors are generally used as a means of reporting both analytical and experimental results.

The Fanning friction factor f_f is defined as follows:

$$f_f = \frac{F_D}{1/2 \rho U_b^2 A_W}, \quad \begin{array}{l} F_D \equiv \text{drag force due to wall shear,} \\ A_W \equiv \text{wetted area,} \end{array}$$

giving

$$f_f = \frac{(r_o \tau_o + r_i \tau_i)}{1/2 \rho U_b^2 (r_i + r_o)} \quad (2-36)$$

This friction factor may be expressed nondimensionally using the following relationships in conjunction with equation (2-26c):

$$Re_b = \frac{U_b D_h}{\nu}, \quad D_h = 2 (r_o - r_i)$$

The result is

$$f_f = \frac{8(b-1)^3}{b(b^2-a^2)} \left(\frac{r_o^+}{Re_b} \right)^2 \quad (2-37)$$

The pressure drop was calculated by first finding the head loss h_f by using the Darcy-Weisbach equation, which is valid for laminar or turbulent duct flows of any cross section:

$$h_f = \frac{f_d LV^2}{D_h 2g} \quad (2-38)$$

The quantity f_d is the Darcy friction factor, which can be found from the relation

$$f_d = 4f_f \quad .$$

The steady flow energy equation with no heat transfer or shaft work and nondeformable surfaces for incompressible flow through a constant area duct reduces to

$$h_f = \frac{\Delta p g_c}{\rho g} \quad (2-39)$$

Equations (2-38) and (2-39) were combined to give

$$\frac{dp}{dx} = \rho \frac{f_d U_b^2}{2D_h g_c} \quad (2-40)$$

The total drag force for the fully developed region comprised of both shear and pressure forces is

$$D_{fd} = \pi \left[2r_i \int_{x=L^*}^{x=L_v} \tau_i dx - r_i^2 \int_{x=L^*}^{x=L_v} \frac{dp}{dx} dx \right], \quad (2-41)$$

where L^* is the entrance length and L_v is the vehicle length. The quantities τ_i and τ_o were found by the iteration procedure described in appendix A. Once the shear stresses have been found, dp/dx may be computed from equation (2-40) and the relationship between the Darcy and Fanning friction factors.

The shear stress and pressure drop are constant in the fully developed region; therefore, equation (2-41) reduces to

$$D_{fd} = \pi \left[2r_i \tau_i (L_v - L^*) - r_i^2 \frac{dp}{dx} (L_v - L^*) \right]. \quad (2-42)$$

RESULTS

A computer code was developed following the iterative scheme described in appendix A. A parametric study was performed of $ITER2(Re_v, b)$. As was previously mentioned, $ITER2$ was the parameter that controlled the step size used in the Runge-Kutta routine. For each Re_v and b , small values of $ITER2$ were chosen, then increased until further increase in $ITER2$ produced no further change in the computed friction factors compared to a very large value of $ITER2$. The values for $ITER2$ that resulted in ± 3.0 -percent difference from the largest $ITER2$ used were plotted in figure 2-5. A curve fit performed for that plot is also displayed. This curve fit was used in the computer code to optimize the step size H for any combination of b and Re_v . Central processing unit (CPU) time varied from 10 minutes to 4 hours. The longest CPU time occurred for $b = 2$ at $Re_v = 10^8$.

Figure 2-8 shows the convergence to a uniform velocity profile for the case $b = 1.333$ and $U_{tube} = 200.0$ ft/s. $ITER\# = 1$ represents the first velocity profile computed for an initial guess of $a = a_{hg}$. This is a

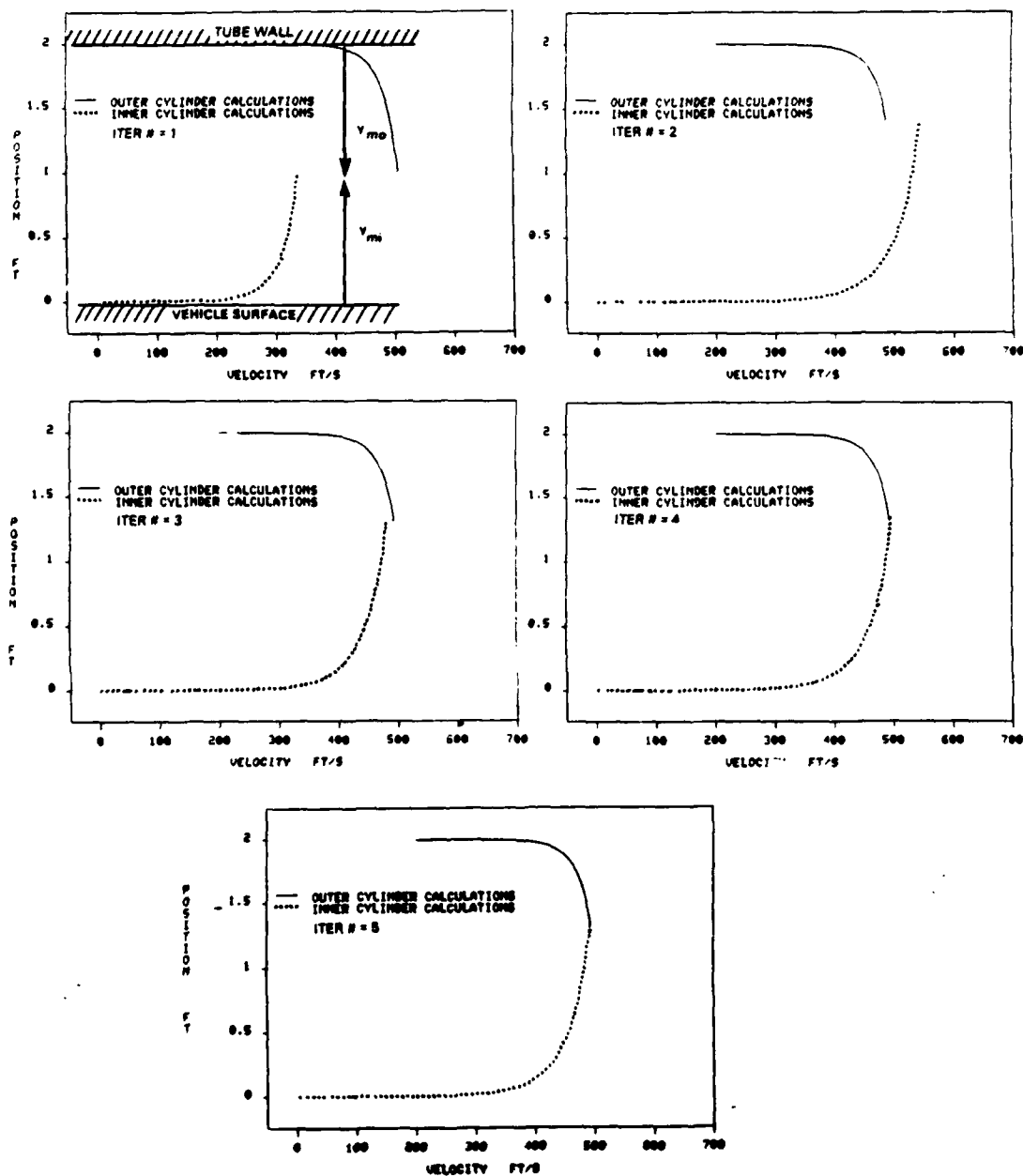


Figure 2-8. Actual Iterative Convergence to a Continuous Velocity Profile

reasonable starting value because the point of maximum velocity will occur close to the center of the annulus. Notice that for ITER# = 1, there exists a large discrepancy between the values of $U_{mo}(y_{mo})$ and $U_{mi}(y_{mi})$. This discrepancy is a physical impossibility and served as a measure of the error of the first guess for "a." The new value for "a" was computed by making use of the percentage difference between U_{mi} and U_{mo} to steer the convergence in the proper direction. Notice at ITER# = 2, r_{mt} was increased, which effectively pushed the region "i" profile out beyond the region "o" profile and resulted in an overcorrection. However, notice that U_{mi} and U_{mo} are now much closer. This procedure of iterating on the quantity a resulted in rapid convergence to a continuous velocity profile in just five iterations. Remember that, although a continuous velocity profile has been found, the correct physical solution is not guaranteed. The profile must be checked for continuity, and the value for "a" adjusted in the proper sense until this flow condition is satisfied. See appendix A.

Figure 2-9 depicts f_{fd} for various values of b and Re_v . The data for this figure are in appendix B. The quantity f_{fd} was calculated by multiplying f_f from equation (2-37) by the factor $(b^2 - 1)/b^2$. This factor comes from the continuity relation, equation (A-1). The newly found friction factor f_{fd} is now in terms of U_v , which is usually known. A considerable amount of time was devoted to generating this figure especially for large values of b and Re_v , which required a large number of iterations (see figure 2-5). Friction factors were smallest for large values of b and Re_v . One may notice from figure 2-9 that a decrease of gap width by a factor of 2 results in increased friction factors by approximately 4000 to 4500 times, depending upon the choice for Re_v .

The following relationships were determined from polynomial regression of observed trends throughout the Reynolds number and radius ratios tested.

The value for the quantity a was found to increase substantially with b and only slightly with Re_v :

$$a = C1 [\log_{10} (Re_v)]^{C2} + 1.0 \quad , \quad (2-43)$$

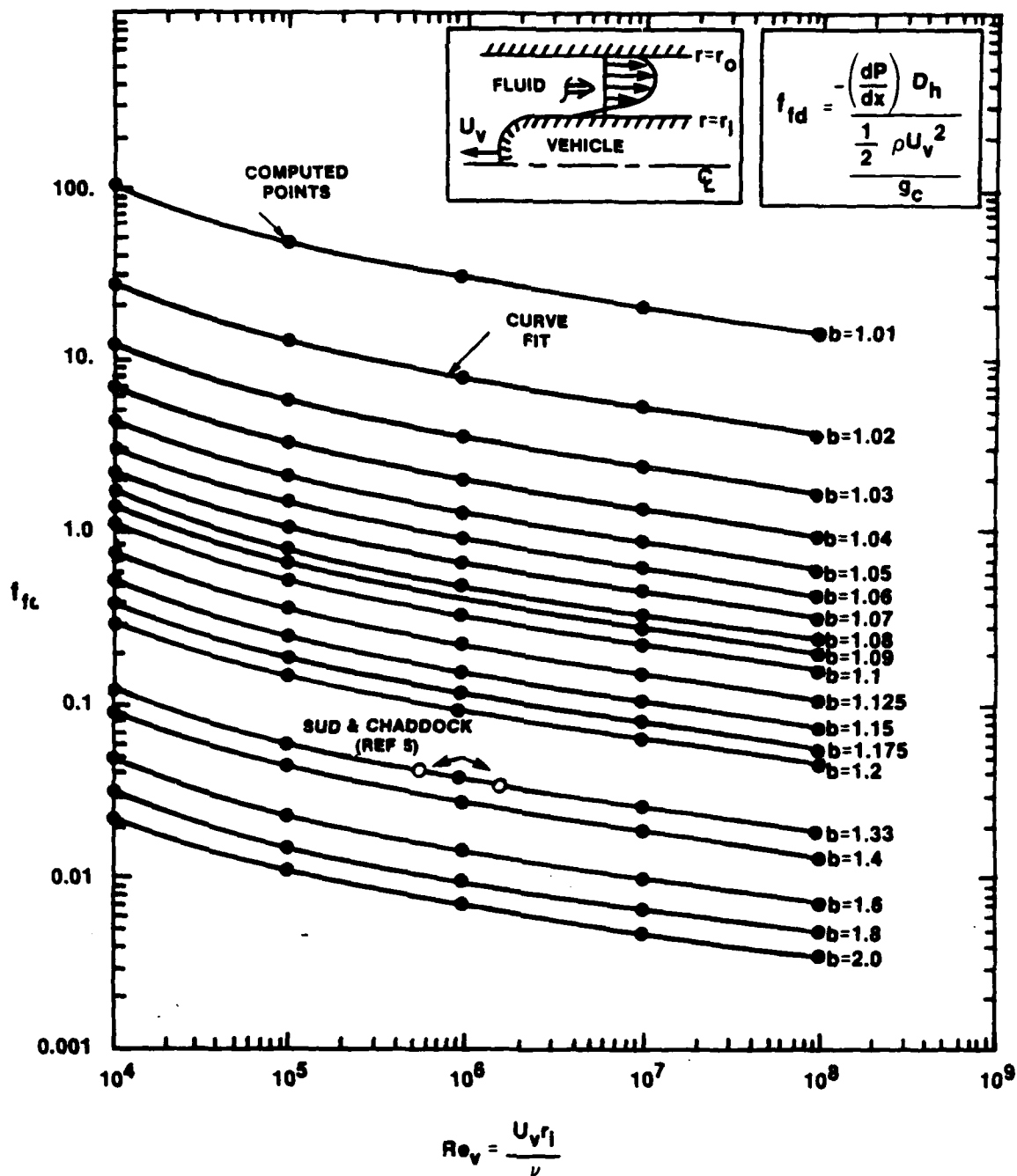


Figure 2-9. Friction Factor Chart for Various Values of b and Re_v in the Region of Fully Developed Flow

where

$$C1 = 0.001 (516.3b - 516.737) \quad \text{for } 1.01 \leq b \leq 1.143,$$

$$C2 = 0.001 \exp (-272.4b^2 + 607.9b - 334.9) \quad \pm 0.16\%,$$

$$C1 = 0.001 (260.2b^2 - 176.2b - 59.04) \quad \text{for } 1.143 < b \leq 2.0,$$

$$C2 = 0.001 \exp (-3.407b^2 + 11.74b - 4.804) \quad \pm 1.07\%.$$

The ratio τ_i/τ_o can be readily computed from equations (2-43) and (2-26c) for given values of b and U_v :

$$Re_v = 10^4, \quad \delta_{mi}^+ = 407.154b - 243.765. \quad (2-44a)$$

$$Re_v = 10^5, \quad \delta_{mi}^+ = 2933.95b - 1755.34. \quad (2-44b)$$

$$Re_v = 10^6, \quad \delta_{mi}^+ = 27,267.1b - 18,137.5. \quad (2-44c)$$

$$Re_v = 10^7, \quad \delta_{mi}^+ = 23,6729b - 161,249. \quad (2-44d)$$

$$Re_v = 10^8, \quad \delta_{mi}^+ = 2,072,380b - 1,437,230. \quad (2-44e)$$

These fits may come in handy during the analysis of developing flow where the upper limit δ_{mi}^+ is needed.

Figures 2-10 and 2-11 were generated from shear stress data obtained from the analysis. The shear stresses were nondimensionalized by the following equations:

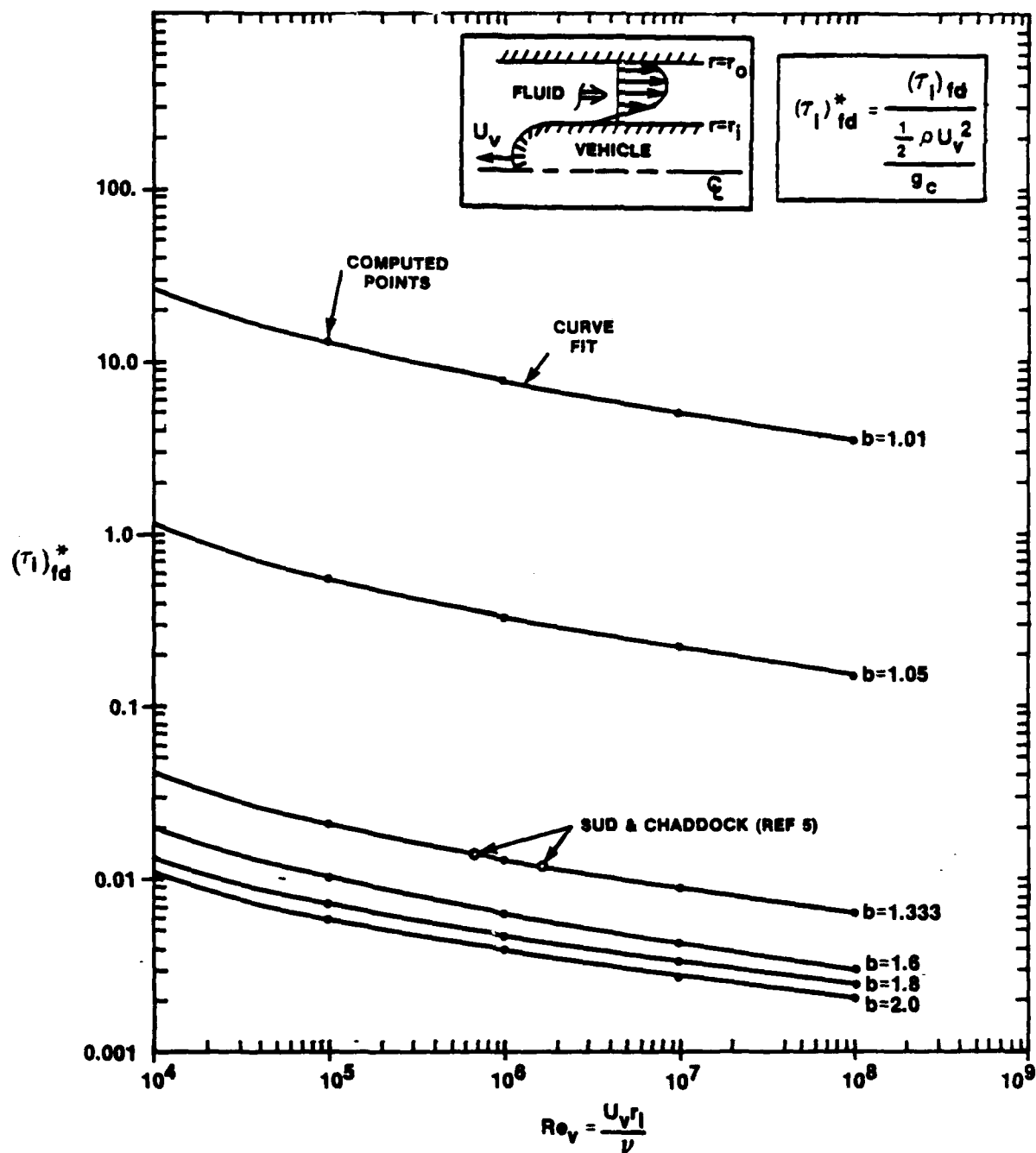


Figure 2-10. Dimensionless Shear for a Range of b and Re_v in Region "1" for Fully Developed Flow

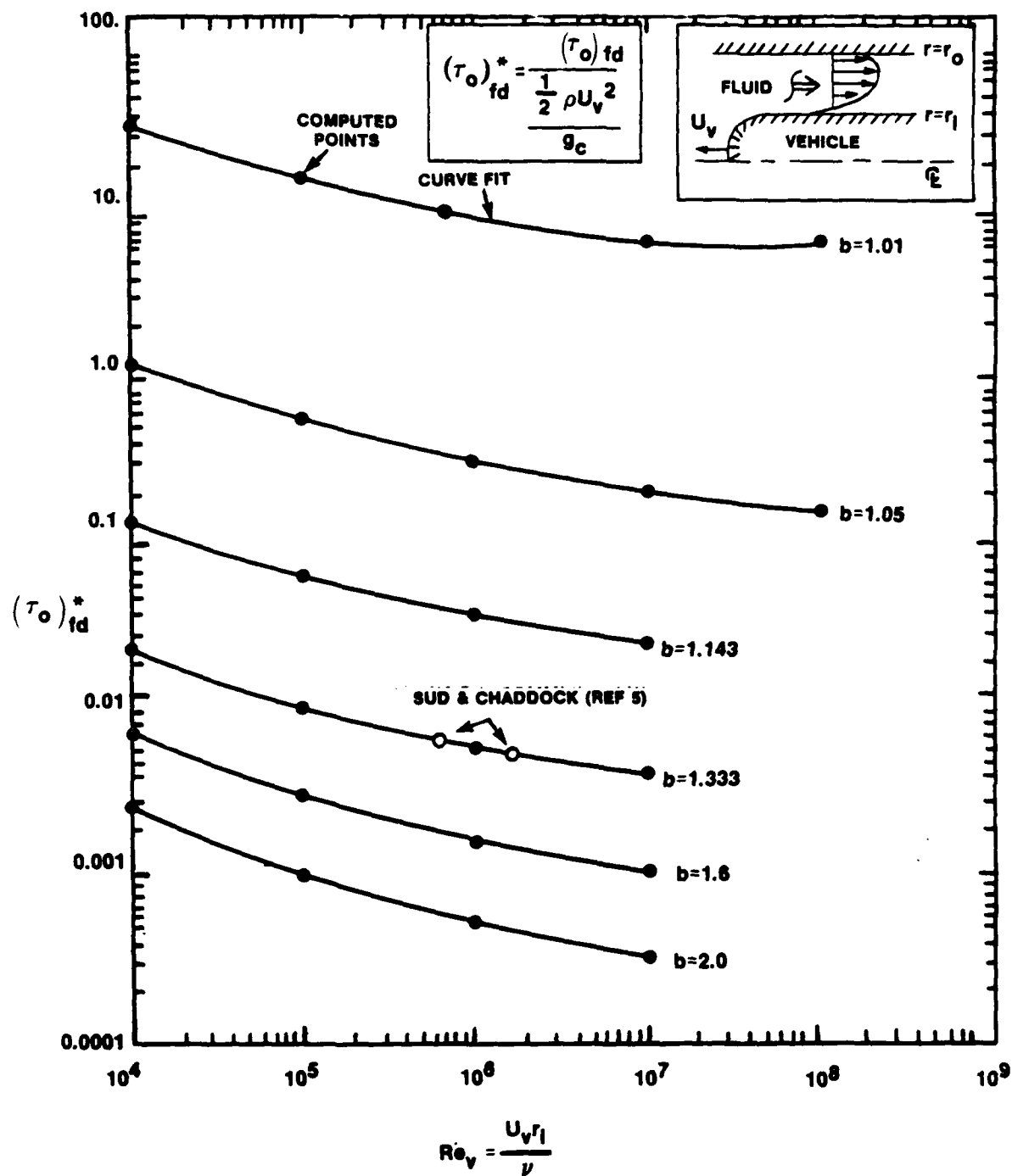


Figure 2-11. Dimensionless Shear for a Range of b and Re_v in Region "o" for Fully Developed Flow

$$(\tau_i)_{fd}^* = \frac{(\tau_i)_{fd}}{\frac{1/2 \rho U_v^2}{g_c}}, \quad (\tau_o)_{fd}^* = \frac{(\tau_o)_{fd}}{\frac{1/2 \rho U_v^2}{g_c}}. \quad (2-45)$$

Shear stresses on the vehicle wall may be readily extracted by using figure 2-10 and the above relations. It is then an easy task to compute the shear drag, equation (2-41). Appendix B contains the values used to generate figure 2-9.

Figure 2-12 displays plots of wall variables for regions "o" and "i" for the case

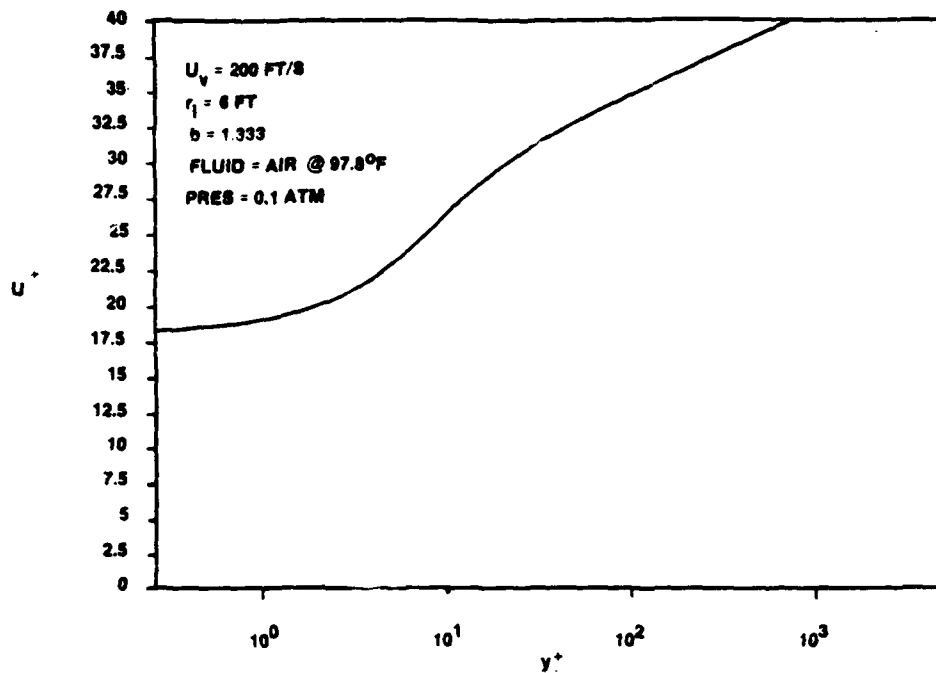
$$U_v = 200.0 \text{ ft/s},$$

$$b = 1.333,$$

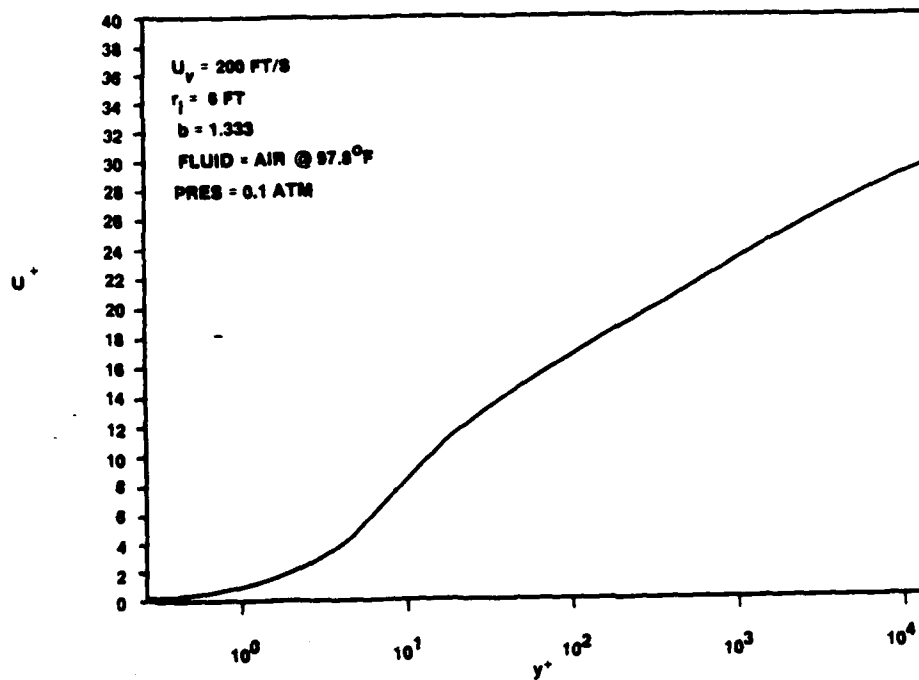
$$r_i = 6.0,$$

$$\nu = 1.786 \times 10^{-3} \text{ ft}^2/\text{s} \text{ (for air at } 97.8^\circ\text{F)},$$

which was also analyzed in reference 17. Although the two-layer model was used in this study, the two plots in figure 2-12 are representative of some three-layer model characteristics exhibiting a sublayer where $u^+ = y^+$, the buffer layer, and then the turbulent layer. Figure 2-13 shows how the eddy diffusivity of momentum varies across the annulus. This figure also shows the relative importance of turbulent to molecular viscosity across the gap of the core. Both figure 2-12 and figure 2-13 show close agreement with the results of reference 17. The maximum velocity was found to occur at $a = 1.22138$, which corresponds to 66 percent of the gap width measured from the vehicle surface. This also can be seen in figure 2-8 for ITER# = 5 and in figure 2-13.



a. DIMENSIONLESS VELOCITY PROFILE IN REGION "o"



b. DIMENSIONLESS VELOCITY PROFILE IN REGION "1"

Figure 2-12. Plots of Wall Variables

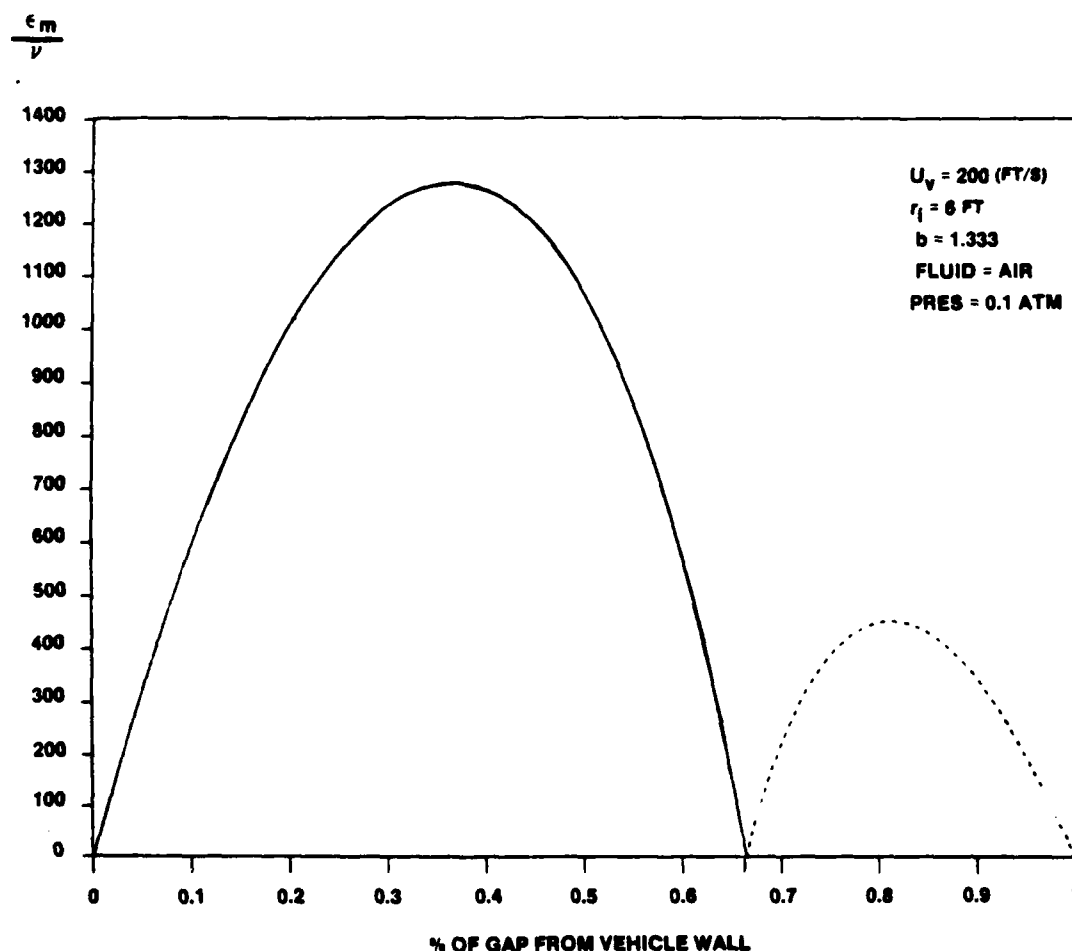


Figure 2-13. Eddy Diffusivity of Momentum Across the Annular Gap

CONCLUSIONS

The friction factor results presented in figure 2-9 agree with the results of reference 19 within 4 to 13 percent, and with the results of reference 5 within approximately 12 percent. The fully developed friction factors of figure 2-9 were compared with the Moody friction factor chart. This comparison, discussed in detail in appendix C, resulted in the conclusion that the Moody diagram can be used to predict the pressure drop for fully developed turbulent flow providing the following correlation is used:

$$f_{fd} = f_M \left[\frac{b^2 + 1}{2(b^2 - 1)} \right]^2, \quad (2-46)$$

where

$$f_M = 0.001 + 2.8 / (\log_{10} Re_b)^{3.1}.$$

As seen from the tabulated results in appendix B, this Moody approximation is accurate to within 4 percent when the value of b is less than 1.2 and has errors up to 10 percent for b between 1.2 and 2.0. The largest error occurs at lower Reynolds numbers, 10^4 - 10^5 .

3. ANALYSIS OF DEVELOPING FLOW

EXPERIMENTAL SURVEY

The region of developing flow is the part of the flow where the fluid core accelerates, and therefore the velocity profiles are functions of axial position. The acceleration is a result of two events.

1. The fluid at a station just ahead of the vehicle is initially at rest. When the vehicle approaches this station, it displaces the fluid, resulting in a fluid velocity greater than its initial value of zero.
2. The merging of boundary layers from both tube and vehicle walls retards the flow within these layers and causes the fluid core velocity to increase so as to keep the volume flux constant at every axial location.

At the annular entrance, the boundary layers are in their infancy. The viscous effects have not had sufficient chance to propagate and are confined to extremely thin layers next to the walls. The velocity of the fluid core must be brought to the respective wall velocity in a very short distance. This gives rise to large velocity gradients (du/dy) at the walls. These gradients decrease as the boundary layers continue to grow downstream. From the relationship $\tau_w = -\mu(du/dy)$, it becomes clear that large shearing stresses are present when large velocity gradients exist, especially at the annular entrance. It is important, then, to determine how the shear stresses vary with axial position so that the shear drag over the entire developing portion may be accurately computed. The end of the hydrodynamic entry region is reached when the upper and lower boundary layers meet (figure 2-2).

Unlike fully developed annular tube flow, little analytical and experimental information is available on turbulent entry flows through annuli, particularly in a case in which one of the walls is moving.

Experimental investigations of turbulent entry flows in annuli with stationary boundaries have been reported in references 20, 21, and 22.

In reference 8, the investigators measured drag forces on the solid core of a vertically positioned annulus. The core was suspended from a calibrated spring while water was passed downward through the annular gap. Radius ratios of $b = 1.78$ and $b = 2.97$ were used for a Reynolds range of $900 - 4.5 \times 10^4$, where the Reynolds numbers were determined from

$$Re = \frac{2(r_o^2 - r_{mt}^2)U_b}{r_o v} .$$

The length of the annulus was varied from 4 to 12 ft so that entrance effects could be studied. Although their experimental apparatus was crude, some useful facts were extracted. The increment of shear friction was found to become persistently larger with increased Reynolds numbers as measurements were taken closer to the annular entrance. The outer wall friction factors were computed by using inner wall values in a relationship derived from a force balance of the annular fluid. This relationship may be used only for fully developed flow since a force imbalance actually exists in the developing portion of the flow. The outer wall factors were found to agree within 2 percent with the data in a previous report (reference 8) for the range $5000 < Re < 3.5 \times 10^5$. It was also found that the outer wall factors were independent of the radius ratio. In addition, the $r_{mt}(Re)$ behavior, which was also calculated using the force balance, agreed within 2 percent with the previous data for $Re > 6000$. In fact, a qualitative assessment of the nature of the flow was not made to indicate at what point the force balance may be applied. It was noted only that beyond 250 equivalent diameters from the throat, the data were little affected by Reynolds numbers. Reference 8 did mention that the use of the force balance to calculate r_{mt} may not be appropriate near the annular entrance.

In reference 21, experiments were conducted on the entrance region taking static pressure measurements. Reynolds numbers based on D_h and U_b ranged from 1.6×10^4 to 7×10^4 . Two radius ratios were used, $b = 2.0$ and $b = 3.2$. Round and square entrances were tested (figure 3-1) for each of these ratios to study the effect of the entrance shape on developing

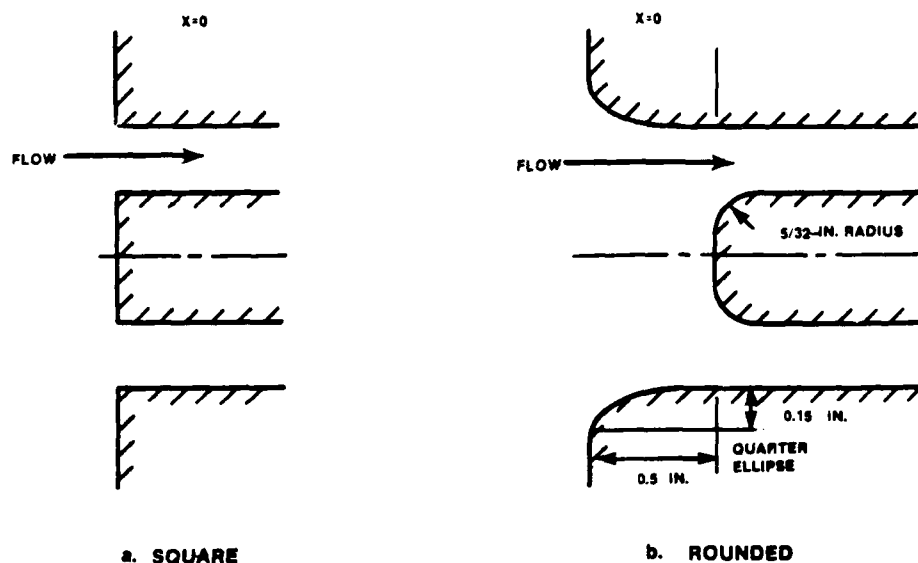
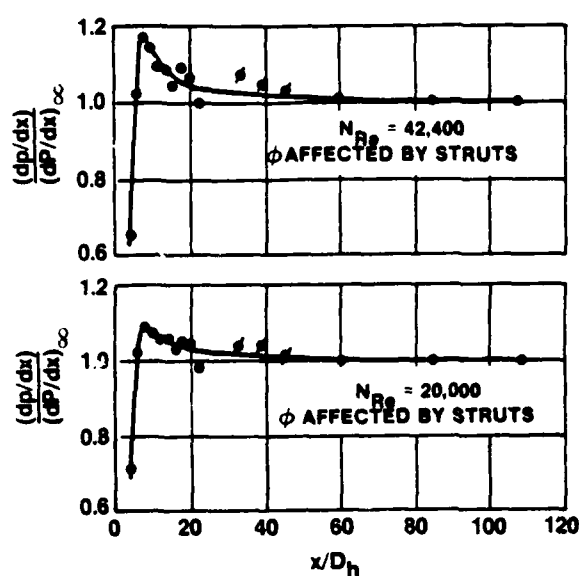


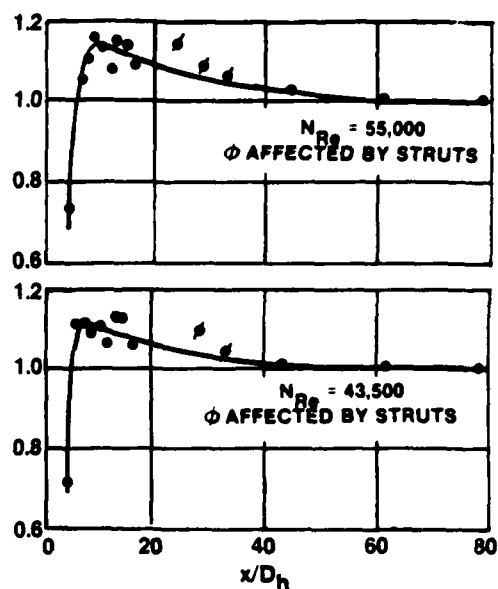
Figure 3-1. Entrance Configurations Used in Reference 21

flow. Entrance lengths for both round and square configurations were found to be 20 to 25 equivalent hydraulic diameters, respectively, an order of magnitude 10 times smaller than that reported by reference 8. The entry length for turbulent flow in circular tubes or parallel plate channels is usually on the order of 20 hydraulic diameters. The investigators in reference 21 found that the square configuration caused an initial separation period in which the pressure drops decreased with distance from the throat. After this period, pressure drops began to increase for approximately three hydraulic diameters (figure 3-2, a and b), at which point they decreased again. The increase in the pressure drops was attributed to the stream expansion following the vena contracta downstream of the sharp entrance.

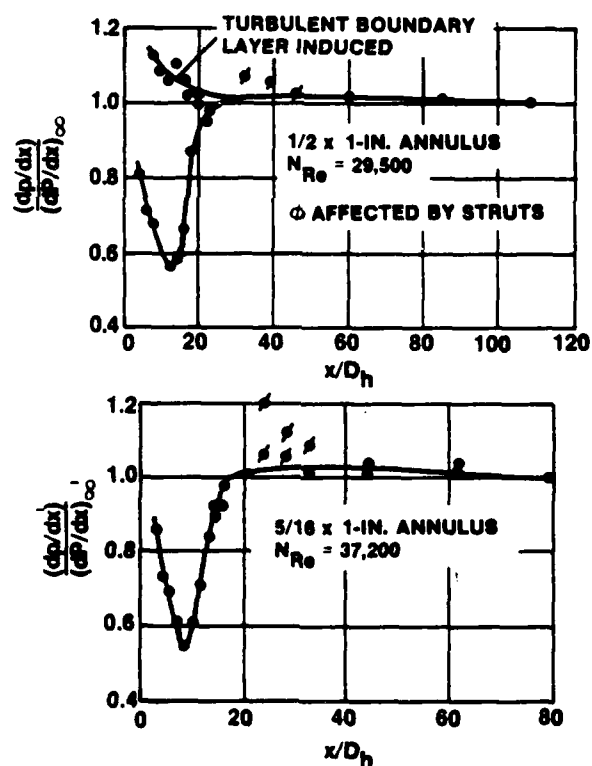
For the rounded entrances, pressure drops were found to decrease up to approximately 12 and 9 hydraulic diameters for $b = 2.0$ and $b = 3.2$, respectively, then increase up to fully developed values (figure 3-2c). The inflection points for both of these ratios were attributed to transition from laminar to turbulent boundary layers. The entry length for the rounded entrance was reduced to 15 hydraulic diameters, and a monotonically



a. LOCAL PRESSURE GRADIENTS FOR 1/2 x 1-IN. ANNULUS WITH A SQUARE ENTRANCE



b. LOCAL PRESSURE GRADIENTS FOR 5/16 x 1-IN ANNULUS WITH A SQUARE ENTRANCE



c. LOCAL PRESSURE GRADIENTS FOR ANNULI WITH ROUNDED ENTRANCES

© 1963, AICHE JOURNAL. REPRINTED WITH PERMISSION.

Figure 3-2. Local Pressure Gradients (from Reference 21)

decreasing pressure gradient resulted by tripping the boundary layer turbulent. The rounded entrances were found to generally improve flow stability. The results shown in figure 3-2c were reported to be qualitatively similar to those in reference 23 for turbulent flow through rectangular and triangular ducts with rounded entrances.

The experiment in reference 23 seemed to be carefully done. Reasonable entrance lengths comparable to plain tube and parallel plate channel flows, which are the limiting cases of annular tube flows, were obtained.

The sharp entrance condition (figure 3-1a) is analogous to the case in which a vehicle is just exiting a tube. The smooth entrance case (figure 3-1b) is more representative of the condition of this present study, except that the length of tube preceding the core may be insufficient. The data presented in reference 21 provide good insight into the nature of developing annular flows. The data can provide a baseline for comparison with an analysis of a vehicle just before it exits a tube.

In reference 22, experiments were conducted similar to those of reference 21. Two annuli having radius ratios of $b = 1.88$ and $b = 2.91$ were investigated. Both annuli were fitted with round and square entrances (figure 3-3). The following information was determined:

1. Mean-velocity profiles
2. Outer wall static pressure gradients
3. Boundary layer thickness parameters
4. Local friction factors.

Re_p ranged from 7×10^4 to 1.6×10^5 . Axial development of velocity profiles for $b = 2.91$ for both entrance geometries is displayed in figure 3-4. The velocity profiles for the square entrance are skewed, especially near the throat, as shown in figure 3-4a. The profiles become less skewed and the maximums shift toward the center of the gap with increased distance from the annular entrance. The profiles for the round entrances are less skewed than those for the square entrances, looking like slug flow near the entrance (figure 3-4b). The shapes of the profiles were

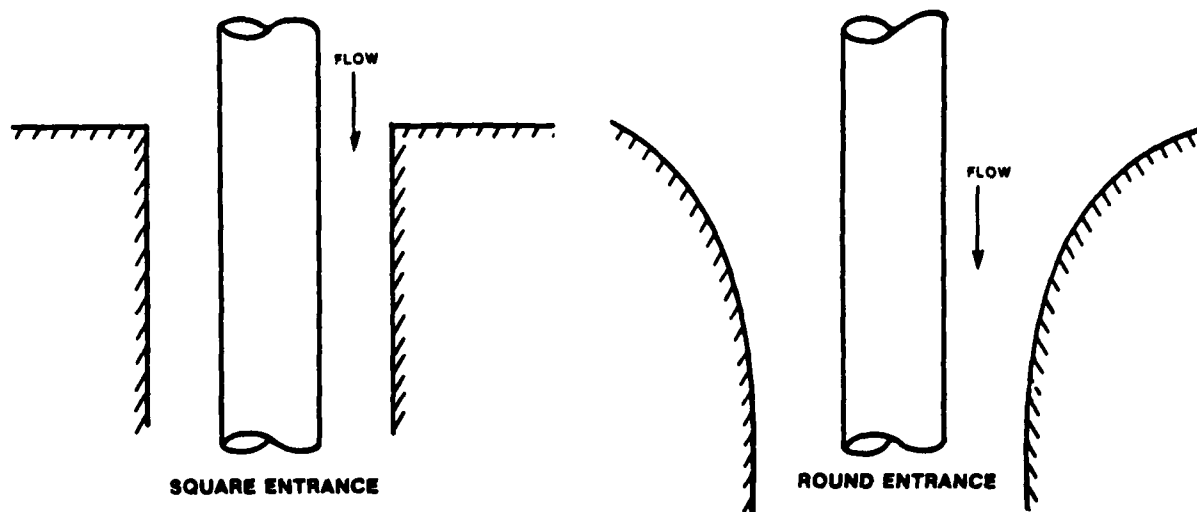
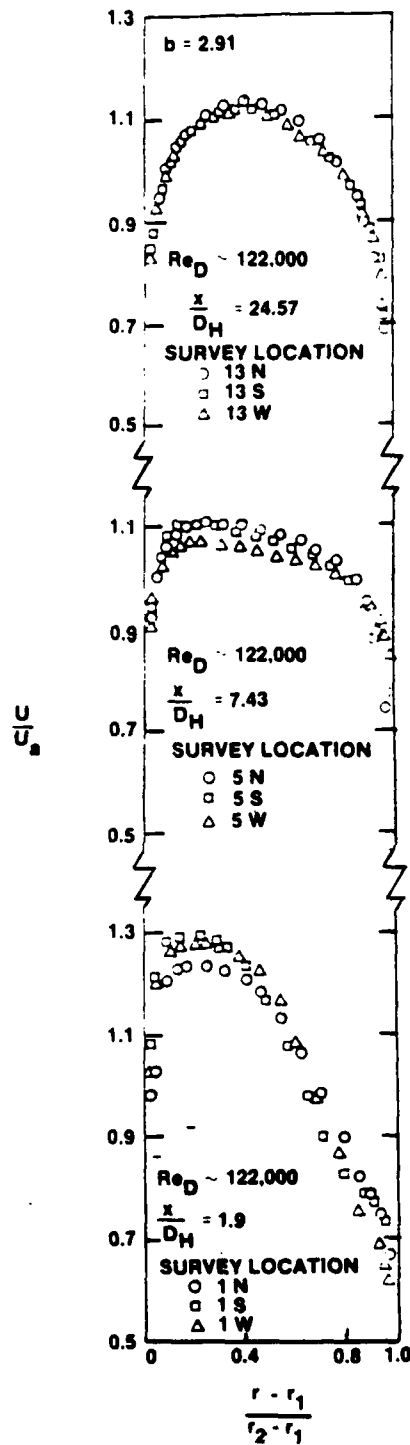


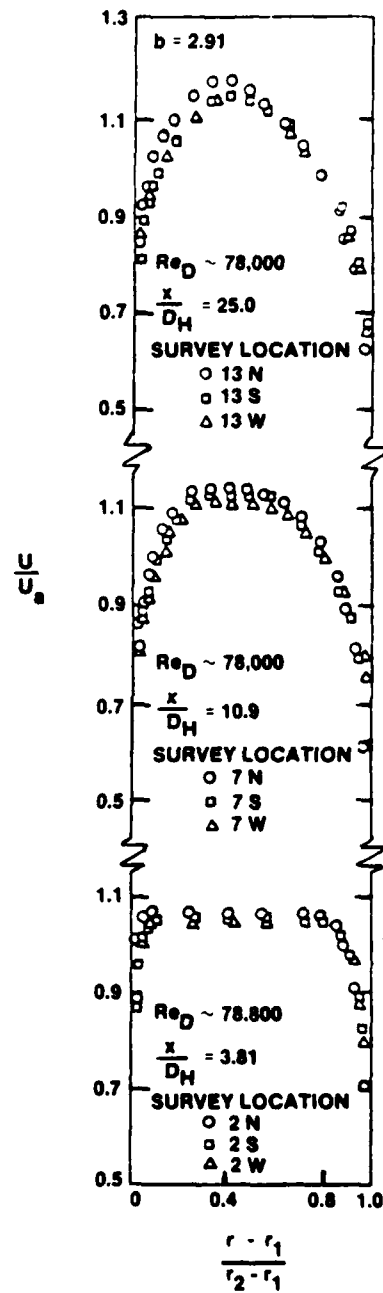
Figure 3-3. Entrance Configurations Used in Reference 22

found to be independent of Reynolds numbers for both entrance geometries. Entry lengths for the square throats with $b = 1.88$ and $b = 2.91$ were found to be 27.73 and 19.81 hydraulic diameters, respectively. However, entrance lengths with the round throats were unobtainable because of flow instabilities that delayed the fully developed condition beyond the test lengths. This contradicts the results in reference 21, which indicated that the entry lengths actually decreased from 25 to 20 equivalent diameters by changing the inlet from sharp to smooth. Notice, however, that the inlet conditions described by these two investigators differ in that for reference 22 the core preceded the tube entrance. Dissimilar results are therefore not unexpected.

The entrance condition investigated in reference 22 is comparable to that of a vehicle exiting a tube. While this condition is not exactly that of the present study, the results of reference 22 provide useful information on developing velocity profiles. The location of transition from the laminar to the turbulent boundary layer was not measured directly. It was estimated using shape factors where a value of 1.4 (from flat plate theory)



a. SQUARE ENTRANCE



b. ROUND ENTRANCE

©1967, ASME JOURNAL OF BASIC ENGINEERING. REPRINTED WITH PERMISSION.

Figure 3-4. Axial Development of Velocity Profiles with Square and Round Entrances (from Reference 22)

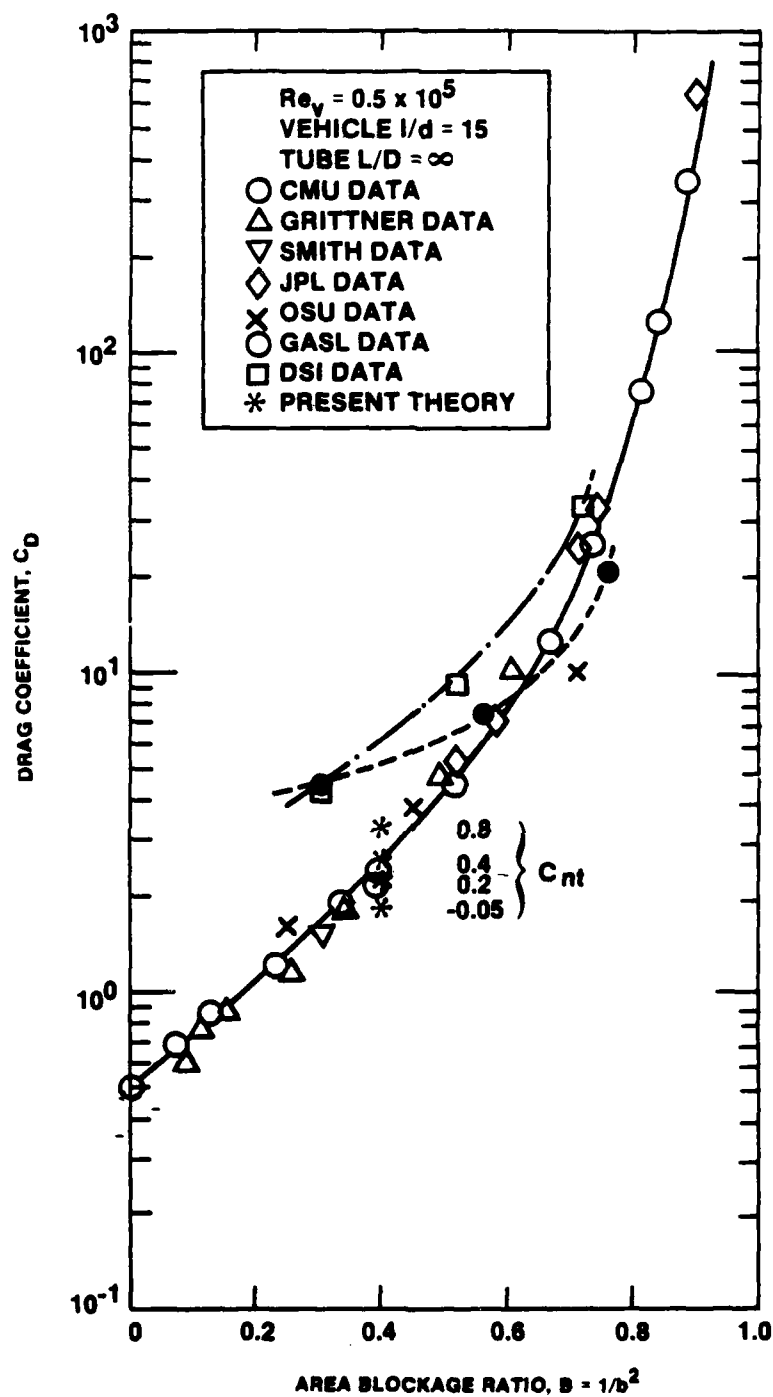
was used to indicate transition from the laminar to the turbulent boundary layer. The calculated shape factors never reached a value of 1.4. Furthermore, the shape factor that indicates transition may be something other than 1.4 for annular tube flow. Thus, it is not certain where transition occurred, if at all. Nevertheless, the investigators contend that transition occurred near the throat of both annuli. Pressure drop data for both entrance geometries showed similar behavior to the data in reference 21.

More recently, the experiments reported in references 6, 24, 25, 26, and 27 were aimed at obtaining correlations between drag force on a vehicle, blockage ratio, and Re_v . Davidson, in reference 6, provided a brief review of these experiments together with a compilation of data onto a single curve (figure 3-5). The experimenters chose 0.5×10^5 for Re_v . Davidson also presented pressure signatures within the annulus from his experiments. C_D was predicted from our present theory for various nose coefficients C_{nt} , and plotted on this figure. A pictorial description of nose shapes and their associated nose coefficients are displayed on page 3-12 of reference 30.

ANALYTICAL SURVEY

Analytical attempts to model the entry region were reported in references 4, 5, and 22. Only round entrances may be considered for conventional boundary layer analysis since separation occurs in flows with square entrances.

In reference 22, it was assumed that radial pressure variations and fluctuating velocity components were negligible. The momentum integral equation was applied to both inner and outer boundary layers separately. The fluid core outside the boundary layers was assumed irrotational. The experimental results showed that the irrotational flow field existed from the annular entrance up to 10-14 hydraulic diameters from the throat for the Re_b range 7×10^4 to 1.6×10^4 . Trends in local friction factors were reportedly similar to the data of reference 28 in which friction factors were generated by using pressure drop data at $x/D_h > 3.81$ and $x/D_h > 5.33$ for $b = 2.91$ and $b = 1.88$, respectively, where the momentum flux was assumed



©1974, DUKE UNIVERSITY. REPRINTED WITH PERMISSION.

Figure 3-5. Comparisons of Experimental Drag Coefficients of Principal Investigators (from Reference 6)

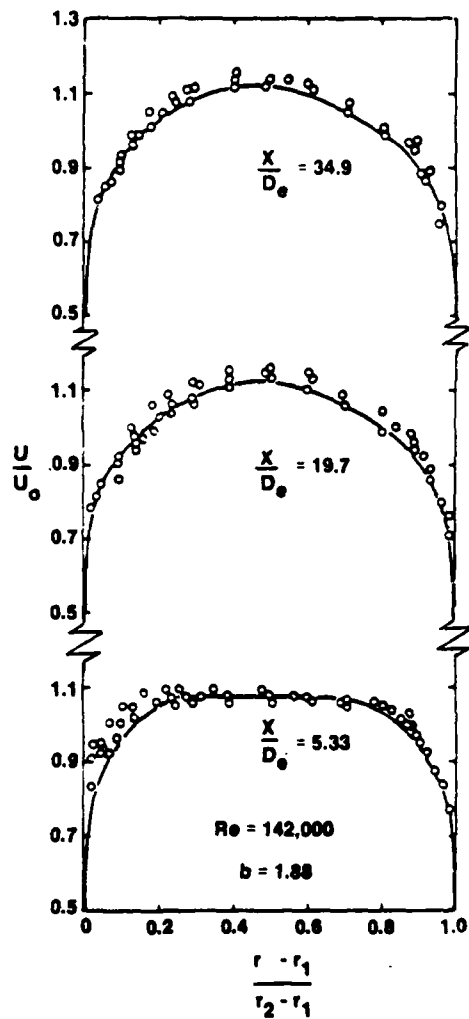
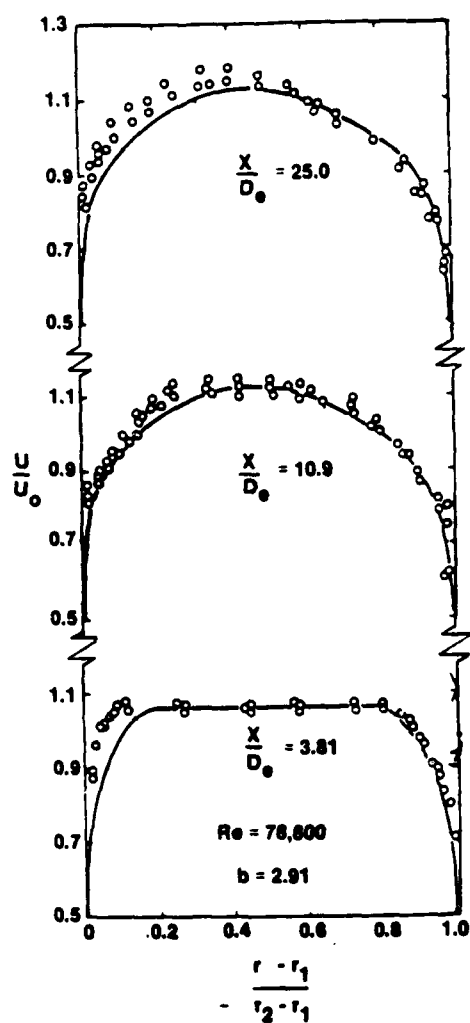
negligible as observed from experimental data. The momentum-integral equation was reduced to the following in terms of friction factors:

$$f_i = \frac{-(r_{mt}^2 - r_i^2)}{\rho U_b^2 r_i} \frac{dp}{dx}, \quad f_o = \frac{-(r_o^2 - r_{mt}^2)}{\rho U_b^2 r_o} \frac{dp}{dx}.$$

It seems odd that the momentum flux becomes negligible so soon before fully developed flow, which occurred beyond $x/D_h = 24.95$ and $x/D_h = 34.93$ for $b = 2.91$ and 1.88 , respectively.

Wilson and Medwell (reference 4) also used the momentum integral method for radius ratios $b = 1.25$ to $b = 5.0$ over a range of Re_b from 10^4 to 3×10^5 . Reichart's expression for eddy diffusivity as suggested in reference 29 was modified by multiplying it by the Van Driest damping factor. This modified expression produced velocity profiles that compared well with the experimental data of reference 22 (figure 3-6). The hydrodynamic entry length for all the radius ratios and Reynolds numbers considered by Wilson and Medwell was found to be approximately 10 equivalent diameters, which strengthens the idea that hydrodynamic development is weakly dependent on radius ratios for the range tested. It appears that Wilson and Medwell have successfully predicted developing profiles in accordance with the experimental data of Okiishi and Servoy (reference 22).

Like Wilson and Medwell, Sud and Chaddock (reference 5) used the momentum integral technique. The eddy viscosity, however, was modeled using a two-layer approach suggested by Quarmby in reference 2. Deissler's equation for eddy diffusivity, equation (2-5), was used for sublayer calculations, and Von Kármán's similarity hypothesis, equation (2-7), was used to obtain the eddy diffusivity expression for turbulent layer calculations. Sud and Chaddock made provisions for a moving boundary, which previously had not been done. Only one radius ratio, $b = 1.33$, and two tunnel pressures, 0.1 and 0.2 atmospheres, were considered at $Re_b = 1.02 \times 10^6$ and $Re_b = 2.55 \times 10^6$, respectively. Sud and Chaddock claim that their entry analysis for large x/D_h predicted velocity profiles, wall shear stresses, and fric-



©1967, ASME JOURNAL OF BASIC ENGINEERING. REPRINTED WITH PERMISSION.

Figure 3-6. Velocity Profiles Predicted in Reference 4 Compared with Data of Reference 22 (from Reference 22)

tion factors that compared favorably with the corresponding values predicted by their fully developed flow analysis. But closer examination of the plotted profiles (figure 3-11b) reveals that the volume flux was not held constant throughout the entry region, rendering their analysis questionable. The total drag coefficient, however, was found to be in good agreement with the compilation of reference 6 (figure 3-5). For the generic case of no moving boundaries, Sud and Chaddock also claimed good agreement with the data of Quarmby in reference 3.

Self-consistency and reasonable agreement with existing data convinced the author of the present study to take an approach similar to that of Sud and Chaddock. However, more care was taken throughout the analysis of developing flow in keeping the volume flux constant. The upper limit of integration for sublayer calculations y_d^+ and the damping factor n^2 were not held fixed as suggested by Sud and Chaddock, but were allowed to vary with Re_b and u^+ as suggested by Quarmby in reference 15 and as discussed under "Assumptions and Boundary Conditions" in section 2. The approach used in this study is summarized as follows:

1. The eddy diffusivities for the sublayer and turbulent layer were modeled by Deissler's equation and Von Kármán's similarity hypothesis, respectively.
2. Velocity profiles were generated by integrating the governing differential equations using the Runge-Kutta technique. The profiles were modified iteratively until continuity requirements were satisfied.
3. The functional dependence of τ_w and Δp with x were found by implementing the momentum-integral technique coupled with the conservation of mass for boundary layers "o" and "i" and for the whole annular gap. The three resulting equations were solved simultaneously (as discussed later in this section) for the unknowns Δp and Δx .
4. Having determined $\tau_w(x)$ from step 3, the shear drag was calculated by numerically integrating the shear stresses over the entry length and multiplying the result by that part of the vehicle's surface area located within the developing region.
5. From step 3, the $\Delta p(x)$ relationship was determined. These pressure drops were numerically integrated over the entry length to obtain the total

pressure drop across that region. The profile drag was then found by multiplying the total pressure drop by the vehicle's projected area.

ASSUMPTIONS AND BOUNDARY CONDITIONS

The same boundary conditions as listed in section 2 apply. The following additional assumption was made for the entry analysis.

The velocity profiles $u(y)$ were determined from equations (2-8) and (2-9) before integrating equations (3-11), (3-12), (3-16), (3-23), and (3-24). Unlike the analysis for the fully developed flow, the shear stress ratios τ/τ_i and τ/τ_o were not determined from equations (2-25c) and (2-20d) that resulted from a force balance. The accelerating fluid in the developing flow region suggests that a force imbalance exists. These ratios were linearized from 1 at the walls to 0 at the edge of the boundary layers as suggested by Wilson and Medwell in reference 4.

LOCATION OF VELOCITY PROFILES

The linear momentum equation, coupled with the conservation of mass principle, was used to determine the axial position of each velocity profile generated. The upper and lower boundary layers were considered separately. Furthermore, two control volumes were used for each boundary layer. The control volume used to locate the first profile within the boundary layer of region "i" is shown in figure 3-7a. Subsequent profiles in region "i" were located using the control volume displayed in figure 3-9.

Consider a control volume for region "i" boundary layer as shown in figure 3-7a. For a steady, fixed control volume, the conservation of mass is

$$\int_{cs} \rho(\bar{V} \cdot \bar{n})dA = 0 , \quad (3-1)$$

where \bar{V} is composed of u , v , w , the axial, radial, and circumferential velocities. Equation (3-1) becomes

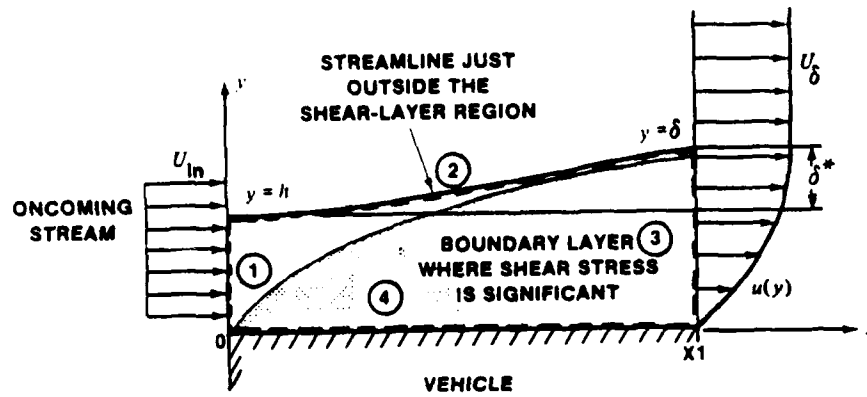


Figure 3-7a. Control Volume Used to Predict Location of First Velocity Profile Within Region "i" Boundary Layer

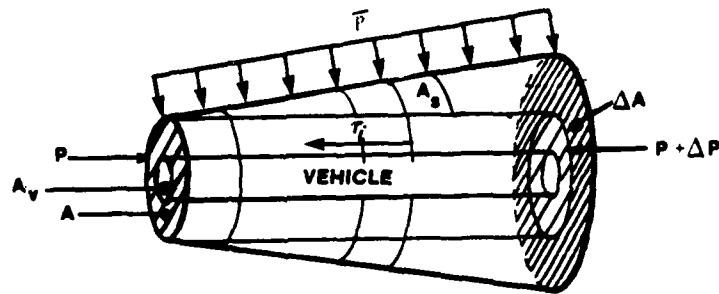


Figure 3-7b. Forces on Control Volume

$$\int_1 \rho(\bar{V} \cdot \bar{n})dA + \int_2 \rho(\bar{V} \cdot \bar{n})dA + \int_3 \rho(\bar{V} \cdot \bar{n})dA$$

$$\int_4 \rho(\bar{V} \cdot \bar{n})dA = 0 \quad , \quad (3-2)$$

where the integrals over 1, 2, 3, and 4 represent the four boundaries of the control surface. The results of the dot products for this control volume in the above equation are summarized in table 3-1.

Table 3-1. Resultant Dot Product on Control Volume Surfaces

Section No.	Axial Station	Boundary Layer Height	Resultant Dot Product
1	$x = 0$	$\delta_i = h$	$\bar{V} \cdot \bar{n} = -U_{in}$
2	$0 < x < x_1$	$h < \delta_i < h + \delta_i^*$	$\bar{V} \cdot \bar{n} = 0$
3	$x = x_1$	$\delta_i = h + \delta_i^*$	$\bar{V} \cdot \bar{n} = u$
4	$0 < x < x_1$	$\delta_i = 0$	$\bar{V} \cdot \bar{n} = 0$

Applying the information from table 3-1 to equation (3-2),

$$\int_{r_i}^{r_i+h} U_{in} r dr = \int_{r_i}^{r_i+h+\delta_i^*} u r dr \quad . \quad (3-3)$$

The steady linear momentum equation is

$$\Sigma_{+ \rightarrow} F_x = \int_{cs} \rho \frac{\bar{V}}{g_c} (\bar{V} \cdot \bar{n}) dA = \frac{\rho}{g_c} \int_1 u (\bar{V} \cdot \bar{n}) dA$$

$$+ \frac{\rho}{g_c} \int_2 u(\bar{V} \cdot \bar{n}) dA + \frac{\rho}{g_c} \int_3 u(\bar{V} \cdot \bar{n}) dA + \frac{\rho}{g_c} \int_4 u(\bar{V} \cdot \bar{n}) dA .$$

Applying the information from table 3-1 to the above equation yields

$$\Sigma F_x = \frac{2\pi\rho}{g_c} \int_{r_i}^{r_i+h+\delta_i^*} u^2 r dr - \frac{2\pi\rho}{g_c} \int_{r_i}^{r_i+h} U_{in}^2 r dr . \quad (3-4)$$

Insert equation (3-3) into equation (3-4):

$$\Sigma F_x = \frac{2\pi\rho}{g_c} \int_{r_i}^{r_{\delta i} = r_i+h+\delta_i^*} u(u - U_{in}) r dr . \quad (3-5)$$

The only forces on the control volume are those due to shear and pressure (see figure 3-7b):

$$\Sigma F_x = F_p + F_{\bar{p}} - F_{p+\Delta p} - F_{SHR} , \quad (3-6)$$

where

$$F_p = pA , \quad (3-7a)$$

$$F_{p+\Delta p} = (p + \Delta p)(A + \Delta A)_i = pA + p\Delta A + \Delta p(A + \Delta A)_i , \quad (3-7b)$$

$$F_{\bar{p}} = \bar{p} A_s \sin \beta \quad \left\{ \begin{array}{l} \sin \beta \text{ gives the x-component of the} \\ \text{force acting on the streamline ,} \end{array} \right\} \quad (3-7c)$$

$$F_{SHR} = 2\pi r_i \int_0^{x_1} \tau_i dx . \quad (3-7d)$$

To find A_s (the surface area of the cone created by the streamline), the streamline depicted in figure 3-7a was assumed to grow linearly with x (see figure 3-8):

$$A_s = 2\pi \int_0^{x_1} (H + x \tan \beta) dx = 2\pi x_1 \left[r_i + \delta_i + (\delta_i^*/2) \right], \quad (3-8)$$

and

$$(A + \Delta A)_i = \pi(r_{\delta i}^2 - r_i^2).$$

δ_i^* can be determined from equation (3-3):

$$U_{in} \frac{(2r_i h + h^2)}{2} = \int_{r_i}^{r_i + h + \delta_i^*} u r dr = \int_{r_i}^{r_i + h + \delta_i^*} (U_{in} + u - U_{in}) r dr,$$

which simplifies to

$$-\delta_i^{*2} + 2(r_i + \delta_i)\delta_i^* + 2 \int_{r_i}^{r_{\delta i} = r_i + h + \delta_i^*} \left(\frac{u}{U_{in}} - 1 \right) r dr = 0. \quad (3-9)$$

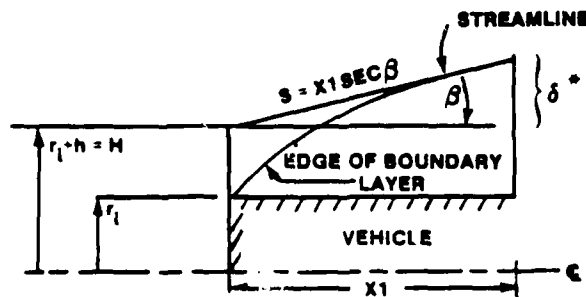


Figure 3-8. Assumed Linear Streamline Growth

Equation (3-9) is a quadratic; then

$$\delta_i^* = \frac{2(r_i + \delta_i) \pm \sqrt{4(r_i + \delta_i)^2 + 8 \int_{r_i}^{r_{\delta i}} \left(\frac{u}{U_{in}} - 1 \right) r dr}}{2}$$

The function $f(r) = (u/U_{in} - 1)r$ is bounded between

$$-r_{\delta i} < f(r) < 0.$$

Then the bounds for

$$M = \int_{r_i}^{r_{\delta i}} f(r) dr$$

are

$$-(r_i + \delta_i)\delta_i < M < 0.$$

For the lower limit of $M = -(r_i + \delta_i)\delta_i$,

$$\delta_i^* = r_i + \delta_i \pm (r_i + \delta_i) \sqrt{1 - \frac{2\delta_i}{r_i + \delta_i}}.$$

The only reasonable solution is obtained when the negative root is taken

$$\delta_i^* = r_i + \delta_i - (r_i + \delta_i) \sqrt{1 - \frac{2\delta_i}{r_i + \delta_i}}.$$

For the upper limit of $M = 0$,

$$\delta_i^* = (r_i + \delta_i) \pm (r_i + \delta_i).$$

Once again, the only reasonable solution is obtained when the negative root is taken, giving

$$\delta_i^* = 0.$$

Therefore, for all computations, the negative root should be used, resulting in the following expression for δ_i^* :

$$\delta_i^* = \frac{1}{2} \left\{ 2(r_i + \delta_i) - \left[4(r_i + \delta_i)^2 + 8 \int_{r_i}^{r_{\delta i}} \left(\frac{u}{U_{in}} - 1 \right) r dr \right]^{1/2} \right\}. \quad (3-10)$$

Assuming:

$$\bar{p} = \frac{\rho U_{\delta av}^2}{2g_c} \quad \text{and} \quad \delta_i^{*2} \approx 0 \quad \text{since} \quad \delta_i^{*2} \ll x_1^2,$$

where

$$U_{\delta av} = 1/2(U_{in} + U_{\delta i}) \quad \text{and} \quad p = \rho \frac{U_{in}^2}{2g_c},$$

and incorporating equations (3-5) and (3-6) gives

{Region "i"}

$$\begin{aligned} - (A + \Delta A)_i \Delta p - \pi r_i (\tau_1 + \tau_{in})_i x_1 &= \frac{2\rho\pi}{g_c} \int_{r_i}^{r_{\delta i}} u_i (u_i - U_{in}) r dr \\ &- \frac{\rho\pi}{4g_c} (2U_{in}U_{\delta i} + U_{\delta i}^2) \left(r_{\delta i} - \frac{\delta_i^*}{2} \right) \delta_i^*. \end{aligned} \quad (3-11)$$

Similarly, for region "o" the momentum balance gives

{ Region "o" }

$$\begin{aligned}
 - (A + \Delta A)_o \Delta p - \pi r_o (\tau_l + \tau_{in})_o x_l &= \frac{2\rho\pi}{g_c} \int_{r_o}^{r_{\delta o}} u(u - U_{in}) r dr \\
 - \frac{\rho\pi}{4g_c} (2U_{in}U_{\delta l} + U_{\delta l}^2) \left(r_{\delta o} - \frac{\delta_o^*}{2} \right) \delta_o^* &. \quad (3-12)
 \end{aligned}$$

The unknowns in equations (3-11) and (3-12) are Δp , x_l , $(\tau_{in})_i$ and $(\tau_{in})_o$. Initially, it was assumed that $(\tau_{in})_i = (\tau_l)_i$ and $(\tau_{in})_o = (\tau_l)_o$. After several values for $\tau_w(x)$ were found, then $(\tau_{in})_i$ and $(\tau_{in})_o$ were found by extrapolating $\tau_w(x)$ out to $x = 0.0$. Therefore, the only two unknowns present in equations (3-11) and (3-12) are Δp and x_l . However, since equations (3-11) and (3-12) do not sufficiently describe the whole flow, another relationship is needed.

Consider a control volume that incorporates the whole annular gap as displayed in figure 3-9. Summing the forces on the control volume,

$$\begin{aligned}
 \Sigma F_x &= F_p - F_{SHRi} - F_{SHRo} - F_{p+\Delta p} , \quad (3-13) \\
 + \rightarrow
 \end{aligned}$$

where

$$F_p = pA ,$$

$$F_{p+\Delta p} = (p + \Delta p)A ,$$

$$F_{SHRi} = 2\pi r_i \int_0^{x_1} \tau_i dx ,$$

$$F_{SHRo} = 2\pi r_o \int_0^{x_1} \tau_o dx .$$

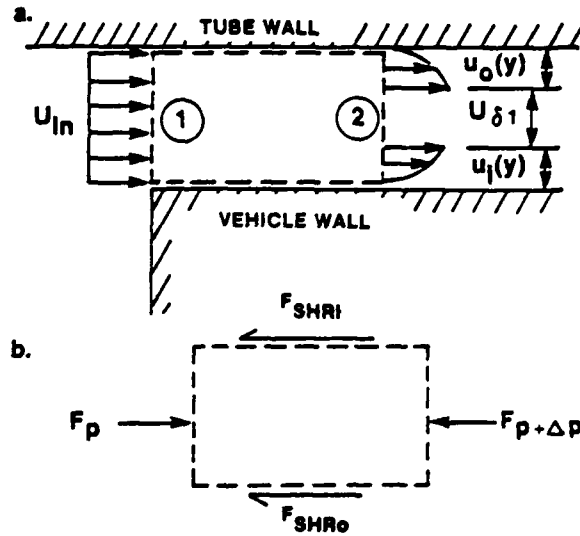


Figure 3-9. Control Volume of Annular Gap

Applying the continuity equation across surfaces (1) and (2) gives

$$- U_{in}(r_o^2 - r_i^2) + 2 \int_{r_i}^{r_{\delta i}} u_i r dr + U_{\delta 1}(r_{\delta o}^2 - r_{\delta i}^2) + 2 \int_{r_{\delta o}}^{r_o} u_o r dr = 0 . \quad (3-14)$$

The momentum equation across sections (1) and (2) gives

$$\Sigma F_{x.} = \frac{2\pi\rho}{g_c} \left[- \int_{r_i}^{r_o} U_{in}^2 r dr + \int_{r_i}^{r_{\delta i}} u_i^2 r dr + \int_{r_{\delta o}}^{r_{\delta i}} U_{\delta}^2 r dr + \int_{r_{\delta o}}^{r_o} u_o^2 r dr \right] . \quad (3-15)$$

Combining equations (3-13), (3-14), and (3-15) and simplifying gives the following relationship:

$$\begin{aligned}
& -\Delta p(r_o^2 - r_i^2) - [r_i(\tau_{in} + \tau_l)_i + r_o(\tau_{in} + \tau_l)_o] x_l \\
& = \frac{2\rho}{g_c} \left[-\int_{r_i}^{r_o} U_{in}^2 r dr + \int_{r_i}^{r_{\delta i}} u_i^2 r dr + \int_{r_{\delta i}}^{r_{\delta o}} U_{\delta}^2 r dr + \int_{r_{\delta o}}^{r_o} u_o^2 r dr \right]. \quad (3-16)
\end{aligned}$$

The two unknowns Δp and x_l are found for region "i" by solving equations (3-11) and (3-16) simultaneously. For region "o," equations (3-12) and (3-16) are solved simultaneously. Naturally, the values of Δp and x_l for region "o" will not initially agree with their counterparts from region "i." The iterative process described in appendix D must be performed until the region "i" and region "o" predictions of x_l match. As a consequence, the Δp from both regions will also match.

To evaluate the location of the velocity profiles within region "i" down stream of the first profile, a momentum balance was performed between two successive profiles as depicted in figure 3-10. The linear momentum equation for this control volume is

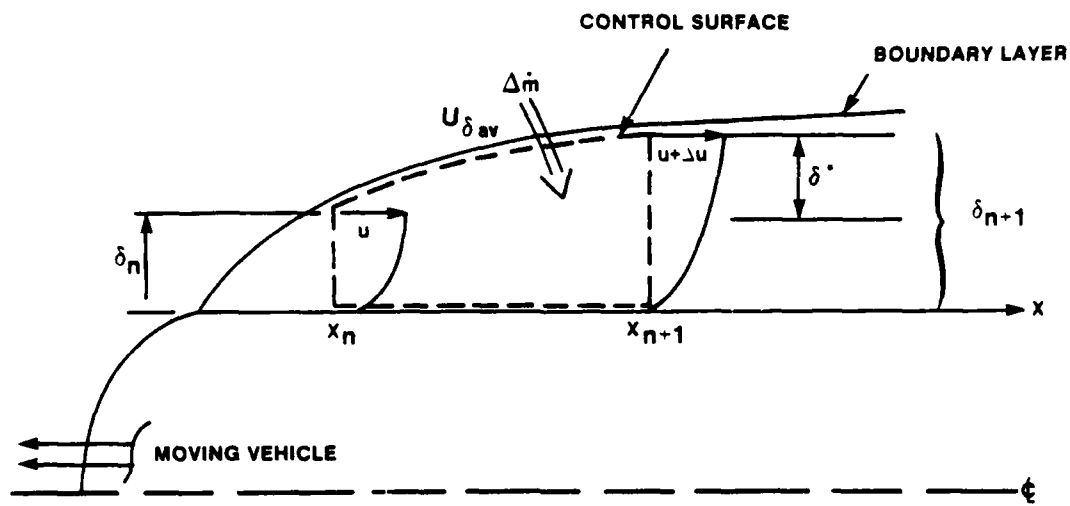
$$\begin{aligned}
\Sigma F_x = & - \int \rho u^2 dA - U_{\delta av} \Delta \dot{m} + \int \rho (u + \Delta u)^2 d(A + \Delta A), \quad (3-17) \\
+ \rightarrow &
\end{aligned}$$

where $U_{\delta av}$ is the average core velocity between $x = x_n$ and $x = x_{n+1}$. Using the fact that

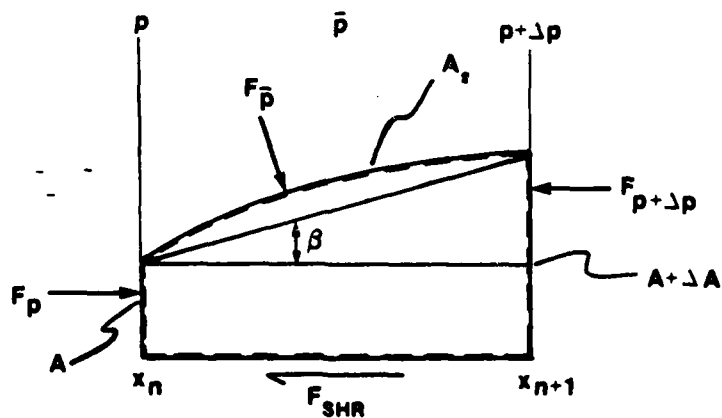
$$\int \rho (u + \Delta u)^2 d(A + \Delta A) = \int \rho u^2 dA + \Delta \left\{ \int \rho u^2 dA \right\},$$

equation (3-17) becomes

$$\begin{aligned}
\Sigma F_x = & - U_{\delta av} \Delta \dot{m} + \Delta \left\{ \int \rho u^2 dA \right\}. \quad (3-18) \\
+ \rightarrow &
\end{aligned}$$



a. PROFILE 1



b. PROFILE 2

Figure 3-10. Control Volume Used to Locate Successive Velocity Profiles Within Region "i" Boundary Layer

From continuity,

$$\Delta \dot{m} = \frac{2\pi\rho}{g_c} \left[\int_{r_i}^{\overbrace{r_i + \delta_{n+1}}^{r_{\delta n+1}}} u r dr - \int_{r_i}^{\overbrace{r_i + \delta_n}^{r_{\delta n}}} u r dr \right]. \quad (3-19)$$

The sum of the forces on the control volume (see figure 3-10b) is

$$\sum_{+ \rightarrow} F_x = F_p + \left(\bar{F}_p \right) - F_{p+\Delta p} - F_{SHR}, \quad (3-20a)$$

where

$$F_p = pA, \quad (3-20b)$$

$$\bar{F}_p = \bar{p} A_s \sin \beta, \quad A_s \equiv \text{surface area of growing boundary layer}, \quad (3-20c)$$

$$\bar{p} = \frac{\rho}{8g_c} (U_{\delta n} + U_{\delta n+1})^2,$$

$$F_{p+\Delta p} = (p + \Delta p) (A + \Delta A) = pA + p\Delta A + \Delta p(A + \Delta A)_i, \quad (3-20d)$$

$$F_{SHR} = 2\pi r_i \int_{x_n}^{x_{n+1}} \tau_i dx. \quad (3-20e)$$

The boundary layer was assumed to grow linearly with x ; thus, the following expression can be written:

$$A_s = 2\pi \int_{x_n}^{x_{n+1}} r(x) dx = 2\pi \left(r_{\delta n} (x_{n+1} - x_n) + \frac{(x_{n+1}^2 - x_n^2) \delta_i^*}{2(x_{n+1} - x_n)} \right), \quad (3-21)$$

where

$$r(x) = \underbrace{r_i + \delta_n}_{r_{\delta n}} + x \tan \beta, \quad \tan \beta = \frac{\delta_i^*}{(x_{n+1} - x_n)},$$

$$\text{and } \delta_i^* = \delta_{n+1} - \delta_n.$$

Inserting equations (3-20b) through (3-20e) and equation (3-21) into equation (3-20a) and neglecting δ_i^{*2} in terms, gives

$$\begin{aligned} \Sigma F_x = -\Delta p (A + \Delta A)_i + \frac{\rho \pi}{g_c} \left[U_{\delta av}^2 r_{\delta n} \delta_i^* - \frac{U_{\delta n}}{2} (r_{\delta(n+1)}^2 - r_{\delta n}^2) \right] \\ - 2\pi r_i \int_{x_n}^{x_{n+1}} \tau_i(x) dx. \end{aligned} \quad (3-22)$$

Combining equations (3-18), (3-19), and (3-22), and letting

$$U_{\delta av} = \frac{U_{\delta(n+1)} + U_{\delta n}}{2},$$

the following expression is arrived at for region "i":

{Region "i"}

$$-\Delta p(A + \Delta A)_i - \pi r_i (\tau_{n+1} + \tau_n)_i \Delta x = \frac{2\pi\rho}{g_c} \left[\left(\int_{r_i}^{r_{\delta i}} u(u - U_{\delta av}) r dr \right)_{n+1} - \left(\int_{r_i}^{r_{\delta i}} u(u - U_{\delta av}) r dr \right)_n - \frac{1}{2} \left(U_{\delta av}^2 (r_{\delta n})_i \delta_i^* - \frac{U_{\delta n}^2}{2} (r_{\delta n+1}^2 - r_{\delta n}^2)_i \right) \right]. \quad (3-23)$$

Similarly, for region "o,"

{Region "o"}

$$-\Delta p(A + \Delta A)_o - \pi r_o (\tau_{n+1} + \tau_n)_o \Delta x = \frac{2\pi\rho}{g_c} \left[\left(\int_{r_{\delta o}}^{r_o} u(u - U_{\delta av}) r dr \right)_{n+1} - \left(\int_{r_{\delta o}}^{r_o} u(u - U_{\delta av}) r dr \right)_n - \frac{1}{2} \left(U_{\delta av}^2 (r_{\delta n})_o \delta_o^* - \frac{U_{\delta n}^2}{2} (r_{\delta n+1}^2 - r_{\delta n}^2)_o \right) \right]. \quad (3-24)$$

Then Δp and Δx can be found for region "i" by solving equations (3-23) and (3-16) simultaneously. Similarly, Δp and Δx for region "o" can be found by solving equations (3-24) and (3-16) simultaneously. There is no guarantee that the prediction of Δx from region "i" will match that from region "o." The quantity δ_o^+ was iteratively changed until the predicted value of Δx from region "i" matched that from region "o." Once the Δx predictions from both region "i" and region "o" equations are in close agreement, the Δp prediction from both regions should, as a consequence, also be in close agreement. For details of the iterative procedure, see appendix D.

The irrotational assumption resulting in the expression

$$dp/dx = -\rho U_\delta (dU_\delta/dx) \quad (3-25)$$

was not used within the momentum balance. Once Δp and x_1 or Δx were found from the momentum balance, they were compared with dp/dx from the irrotational assumption. This was done to determine if the momentum balance was performed correctly.

SCHEME FOR DETERMINING VEHICLE DRAG IN DEVELOPING FLOW

The scheme shown in appendix D was used to obtain the local pressures and shear stresses in the annulus during the developing portion of the flow up to the point where the boundary layers meet (fully developed). The scheme provided the following:

1. Convergence on matching of $U_{\delta i}$ and $U_{\delta o}$.
2. Constant volume flux throughout the annulus.
3. Correct axial position of the developing velocity profiles and boundary layer heights.

The general procedure for obtaining these results is as follows:

1. Equations (2-8) and (2-9) were used to generate the velocity profiles for each of the chosen dimensionless boundary layer heights δ_i^+ .

2. The following procedure was implemented so that $\Delta p(x)$ and $\tau_w(x)$ could be determined.

a. To locate first velocity profile:

- (1) Solve equations (3-11) and (3-16) simultaneously for x_1 and Δp .
- (2) Solve equations (3-12) and (3-16) simultaneously for x_1 and Δp .
- (3) Change δ_0^+ and follow iteration scheme of appendix D.
- (4) Repeat steps (1) through (3) until x_1 values predicted from steps (1) and (2) match.

b. To locate successive velocity profiles:

- (1) Solve equations (3-23) and (3-16) simultaneously for Δx and Δp .
- (2) Solve equations (3-24) and (3-16) simultaneously for Δx and Δp .
- (3) Change δ_0^+ and follow iteration procedure of appendix D.
- (4) Repeat steps (1) through (3) until Δx values predicted from steps (1) and (2) match.

3. The local pressure drops and shear stresses on the vehicle wall at each axial station have been determined from step 2.

The fluid dynamic drag imparted on the portion of the vehicle subjected to developing flow is

$$(\text{Drg})_e = A_v \int_0^{L^*} \left(\frac{dp}{dx} \right)_e dx + 2\pi r_i \int_0^{L^*} (\tau_i)_e dx . \quad (3-26)$$

The total drag on the vehicle due to concentric annular flow (developing and fully developed) is obtained by summing equations (2-42) and (3-26).

The drag contributions due to the nose and base of the vehicle have not been incorporated in the analysis. They can be included to find the overall drag as discussed in appendix H.

RESULTS

Fifteen velocity profiles were typically generated within the developing region. The CPU time was seen to vary from 10 to 40 minutes. Generally, the CPU time increased with increasing values of Re_v and b for $0.01 \leq b \leq 2.0$ and $10^5 \leq Re_v \leq 10^7$.

A test case was run so that the present analysis could be compared with that of Sud (reference 17). Figures 3-11a and 3-11b show this comparison for the case of:

$$\begin{aligned}U_{tube} &= 200 \text{ ft/s} \\r_i &= 6 \text{ ft} \\r_o &= 8 \text{ ft} \\p &= 0.1 \text{ atm} \\Re_b &= 1.02 \times 10^6 \\T &= 98^\circ\text{F}.\end{aligned}$$

Profiles 1 and 2 of figure 3-11a are the developing profiles at $x/D_h = 1.53$ and $x/D_h = 18.95$, respectively. Profile 2 is the nearly fully developed velocity profile as predicted by the developing analysis. Profile 3 was computed from the fully developed analysis. Note that profiles 2 and 3 are very similar, even though they were computed independently, with continuity being the only common link. Closer examination of these profiles reveals that the area under each curve is the same, which indicates that the volume flux remained constant throughout the analysis. The near equality between profiles 2 and 3 gives confidence that the current model is self-consistent and correct within the limits of integral theory. The profiles of figure 3-11a and those obtained by Sud, figure 3-11b, are similar with respect to profile shape, magnitude, and position of maximum velocity. Careful examination of the profiles labeled " $x/D_h = 11.47$ " and "Fully Developed" in figure 3-11b suggests that continuity was violated.

Figure 3-12 shows that the present model compares well with the experimental results of Davidson (reference 6). The pressure drop over L_n could be computed by using a nose coefficient from Hoerner in conjunction with the Bernoulli equation (see appendix H). The exact coefficient for an ogive

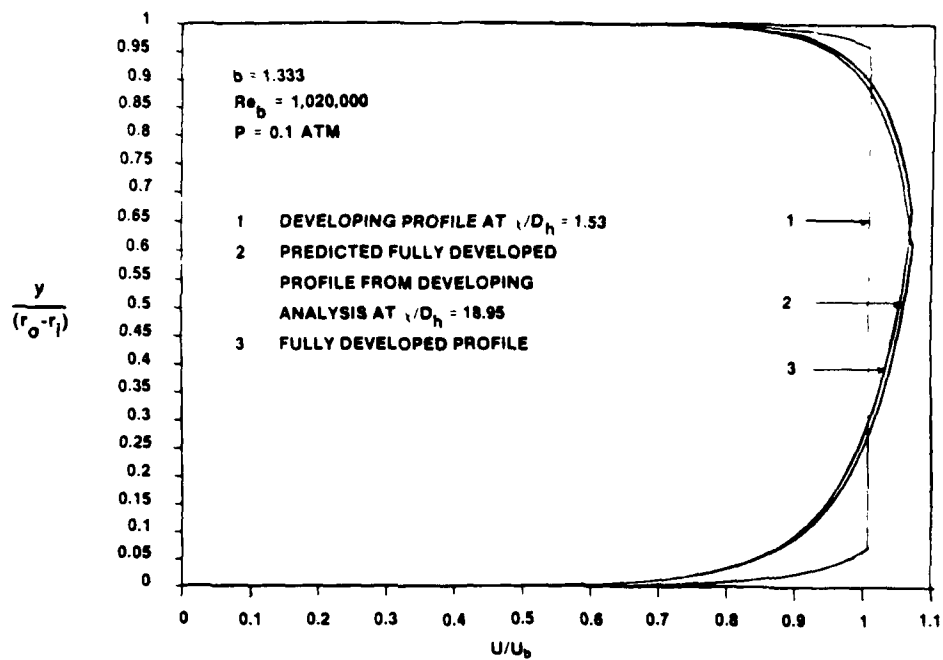


Figure 3-11a. Comparison of Developing and Fully Developed Velocity Profiles from Present Simulation

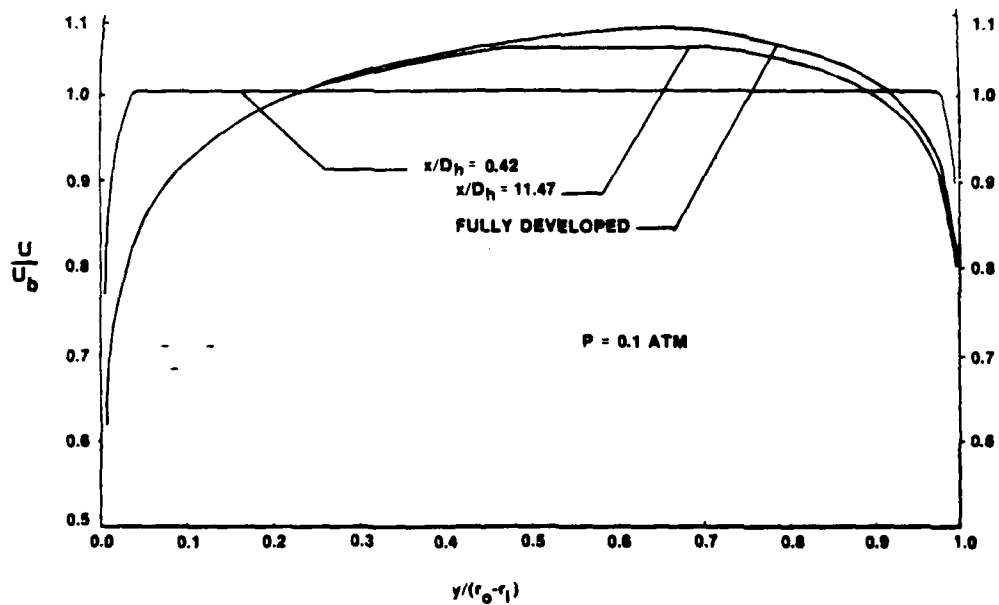


Figure 3-11b. Developing Velocity Profile in the Entrance Region Predicted in Reference 17

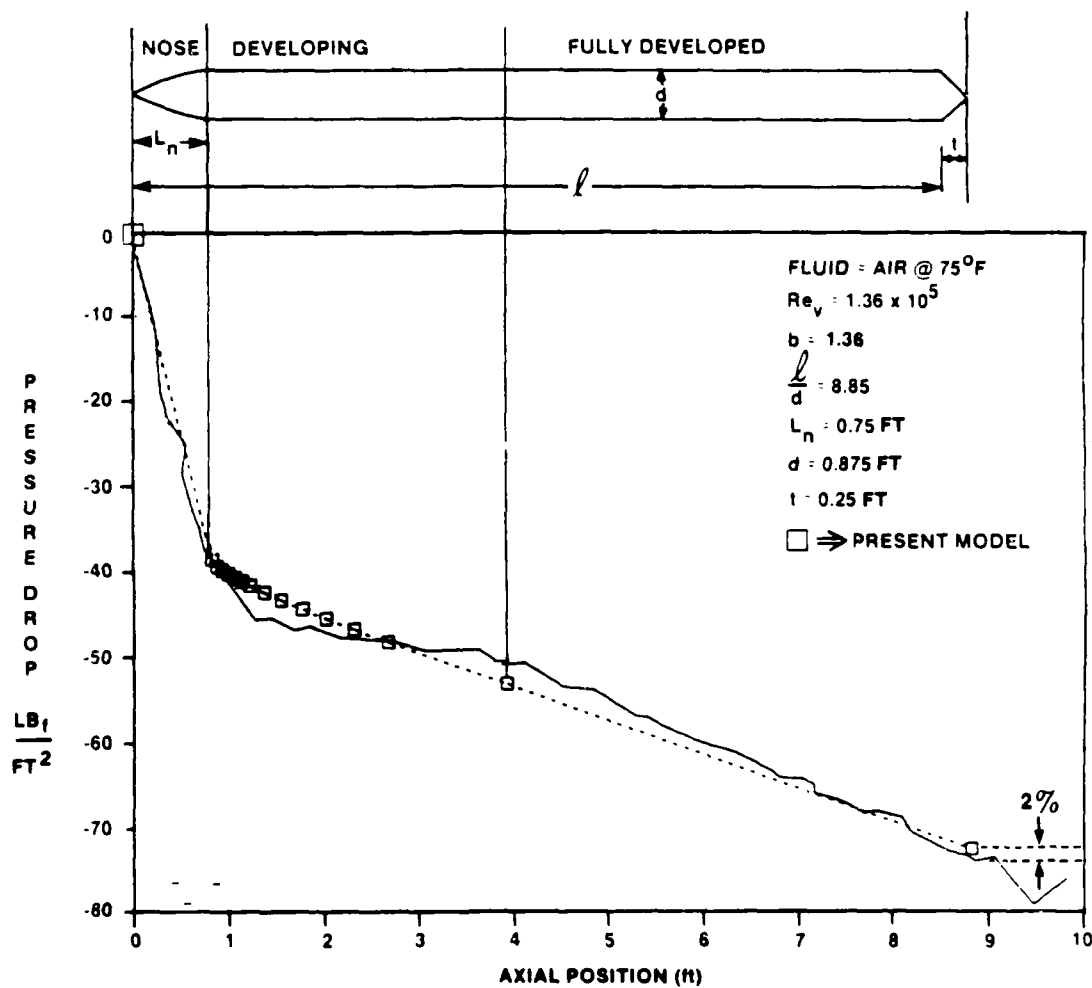


Figure 3-12. Comparison of Experimental Results from Reference 6 and Present Theory

nose was not known; therefore, the Δp across L_n was set equal to the corresponding value obtained by Davidson. The present analysis takes over from that point on. The Δp across length l agrees within 2 percent with Davidson's data (see figure 3-12).

The following example was run because it represents a typical Navy problem of a torpedo moving within a tube.

$$\begin{aligned}U_{\text{tube}} &= 40 \text{ ft/s,} \\r_i &= 10.5 \text{ in.,} \\r_o &= 12.0 \text{ in.,} \\v &= 0.12583 \times 10^{-4} \text{ ft}^2/\text{s (sea water at } 60^\circ\text{F).}\end{aligned}$$

The results of the developing flow model are displayed in figures 3-13 through 3-18. Figure 3-13 shows 3 of 15 computed velocity profiles as they develop in the annulus. These are at approximately 10 percent, 50 percent, and 95 percent of boundary layer growth. Appendix G (table G-1) summarizes the results of the entry computation shown in this figure. Notice that the developing flow model at large x/D_h agrees well with the fully developed flow model. The largest discrepancy (3.1 percent) exists for the δ_o computation. A comparison of core velocities reveals that they agree within 1.3 percent for this case. The volume fluxes within the three regions (lower boundary layer, core, and upper boundary layer) for these three profiles are listed in table G-2. It is interesting to note that throughout development the volume flux for the region "i" boundary layer is always greater than that for region "o." This trend was consistent throughout the range of b and Re_v tested. The total volume fluxes Q_{tot} for each profile displayed in figure 3-13 is within 0.8 percent of the volume flux entering the annulus Q_{in} . This indicates that continuity has been fulfilled throughout the developing flow analysis.

Figure 3-14 shows shear stress development on both the tube and vehicle walls. Notice that maximum shear stress on both walls occurs at the throat of the annulus. The maximum developing shear stress on the vehicle is approximately 7.7 times greater than the value for fully developed flow. By approximately 4 hydraulic diameters (15 percent of entry length) the shear

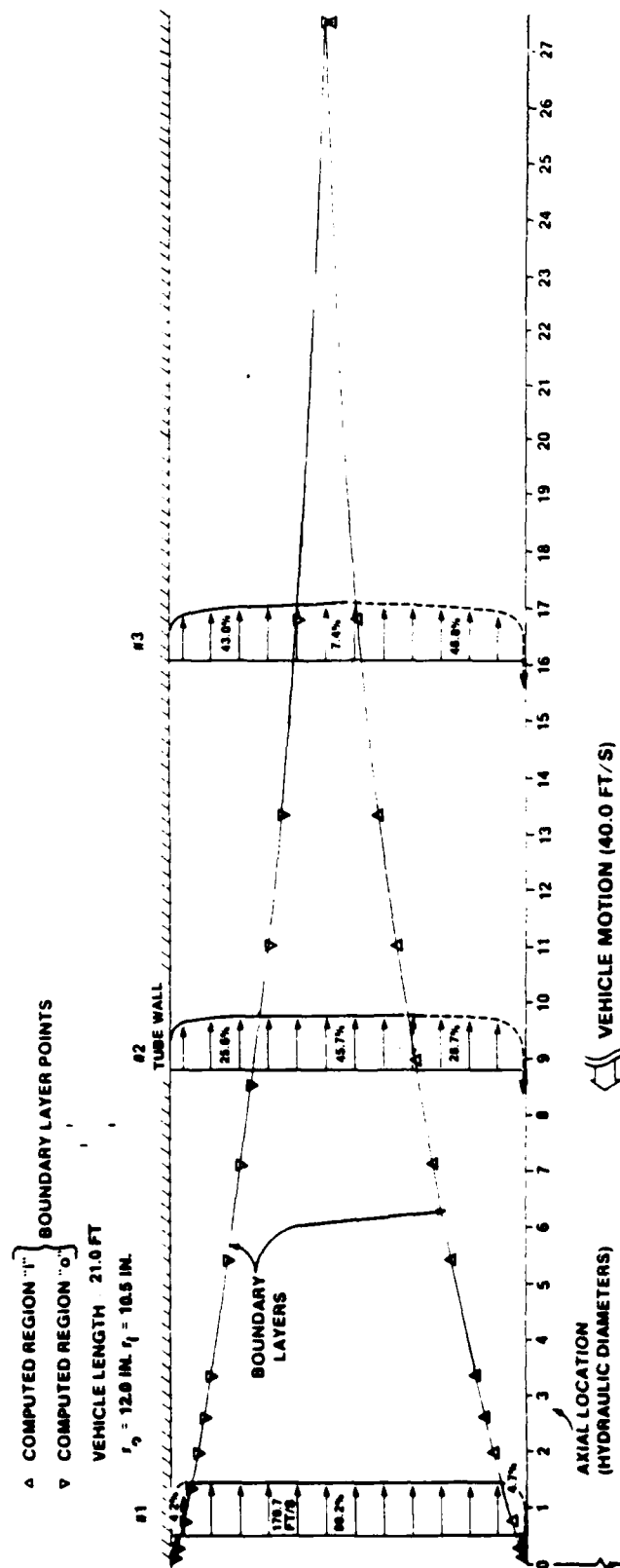


Figure 3-13. Example of Computed Velocity Profiles for Developing Flow Model

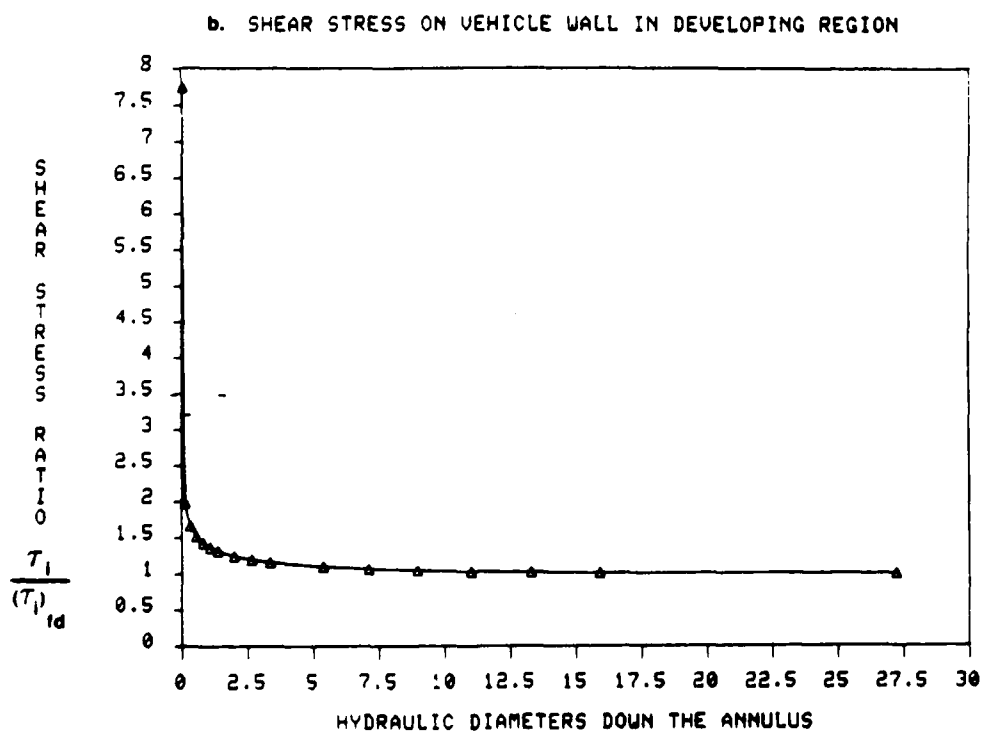
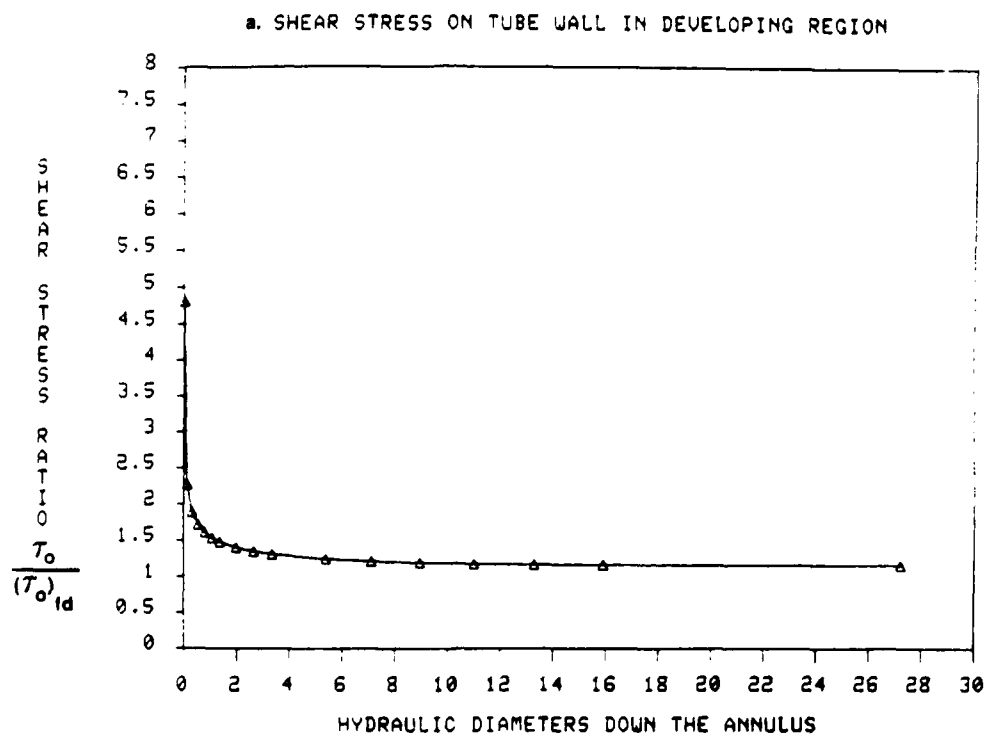


Figure 3-14. Wall Shear Stress Development

stresses decay to within 10 percent of the values for fully developed flow. The rapid decay of these developing shear stresses translates to a small increase in shear drag when compared with fully developed values.

Figure 3-15 displays the local pressure drops during profile development. The pressure drop at the annular throat is roughly 6.3 times greater than the value for fully developed flow and decays to within 10 percent of such values by approximately 11 hydraulic diameters (41 percent of entry length). Of the two (shear and form) drag contributors in the entry region, the form drag seems to be of greater significance to the total. To quantify these two drag contributors, the drag force due to each (calculated in appendix E) is presented below:

$$\begin{array}{rcl}
 (\text{PDRG})_e & = -14,788 \text{ lbf [27.5 percent of } (\text{DRG})_T]. & \\
 (\text{SHRDRG})_e & = -2354 \text{ lbf [4.4 percent of } (\text{DRG})_T]. & \left. \vphantom{\begin{array}{l} (\text{PDRG})_e \\ (\text{SHRDRG})_e \end{array}} \right\} 31.9 \text{ percent} \\
 (\text{SHRDRG})_{fd} & = -5424 \text{ lbf [10.1 percent of } (\text{DRG})_T]. & \\
 (\text{PDRG})_{fd} & = -31,252 \text{ lbf [58.1 percent of } (\text{DRG})_T]. & \left. \vphantom{\begin{array}{l} (\text{SHRDRG})_{fd} \\ (\text{PDRG})_{fd} \end{array}} \right\} 68.2 \text{ percent} \\
 (\text{DRG})_T & = -53,818 \text{ lbf.} &
 \end{array}$$

As suspected, $(\text{PDRG})_e$ was substantially larger than $(\text{SHRDRG})_e$. The largest drag contributor is $(\text{PDRG})_{fd}$, with the fully developed flow region contributing 68.2 percent to the total drag. Of course, the amount that all of these contribute to drag would vary, depending on L_v , b , and U_v .

Figure 3-16 shows that use of the irrotational assumption within the momentum balance can be an inaccurate method for computing dp/dx . The irrotational assumption does rather well between the second computed point and at four hydraulic diameters. Beyond four hydraulic diameters, dp/dx

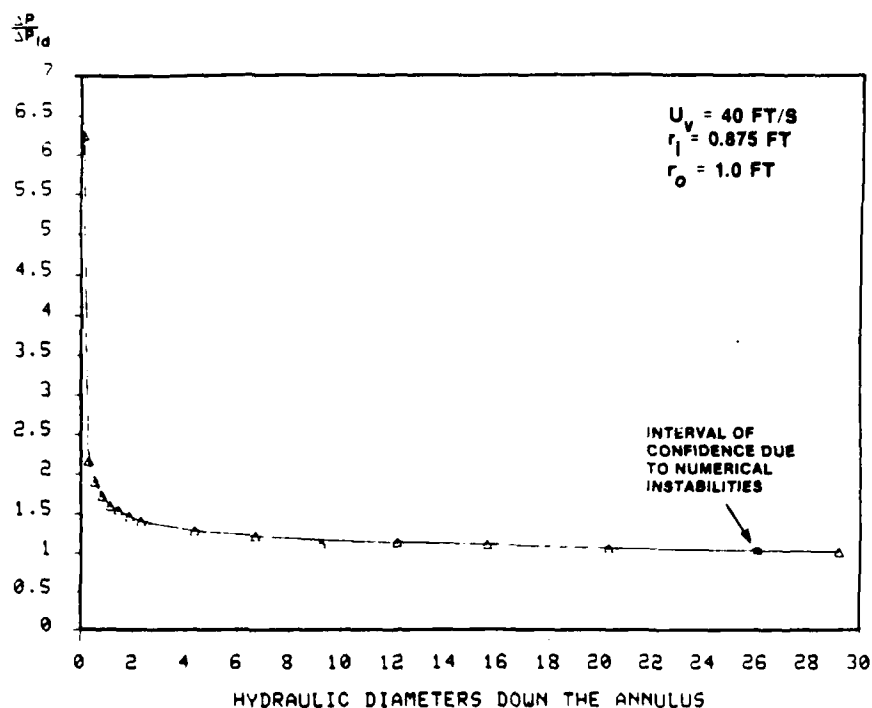


Figure 3-15. Pressure Signature in the Annulus for Developing Flow

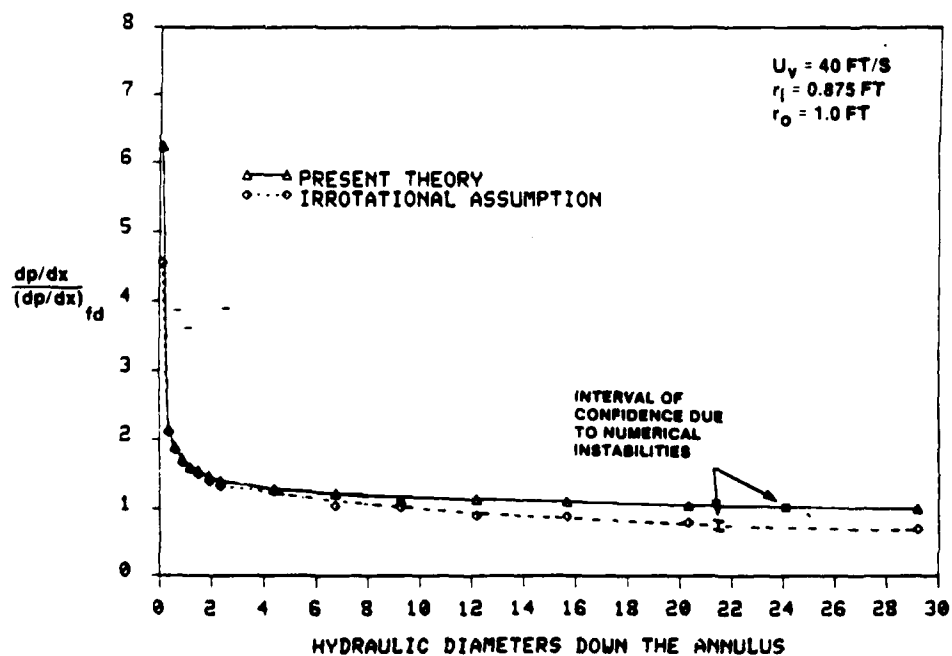


Figure 3-16. Pressure Signature of Present Method Compared with That from Irrotational Assumption

dips below the fully developed value long before the flow becomes fully developed (30 percent of entry length).

Figure 3-17 displays the friction factor behavior during flow development. It takes approximately 11 hydraulic diameters for the friction factor to decay to within 10 percent of values for fully developed flow. The largest factor occurs at the annular throat and is approximately six times greater than the fully developed value.

Figure 3-18 displays the velocity ratio $U_\delta/U_{\delta_{fd}}$ as a function of hydraulic diameters down the annulus. It is important to note that the core velocities U_δ are increasing monotonically. This behavior must occur and acts as an indicator of the numerical stability of the analysis. Notice from this figure that the velocity at the annular throat is approximately 94 percent of the fully developed value. If the monotonicity of the core velocities is not achieved, the dU_δ/dx may fluctuate wildly and cause considerable error in calculations for the local pressure drops. This can be easily seen from the irrotational assumption

$$\frac{dp}{dx} = -\rho \frac{U_\delta}{g_c} \left(\frac{dU_\delta}{dx} \right).$$

The curves of figure 3-19 were generated by computing dp/dx at a number of axial locations (same as figure 3-15) for each Re_v and b . The integrated value was then determined from

$$\frac{\Delta p}{L^*} = \frac{1}{L^*} \int_0^{L^*} \left(\frac{dp}{dx} \right) dx$$

and nondimensionalized as shown in the upper right corner of figure 3-19.

The curves of figures 3-20 and 3-21 were generated in a manner similar to that used for figure 3-19; however, the values for $(\bar{\tau}_i)_e$ and $(\bar{\tau}_o)_e$ were nondimensionalized as shown in figures 3-20 and 3-21, respectively.

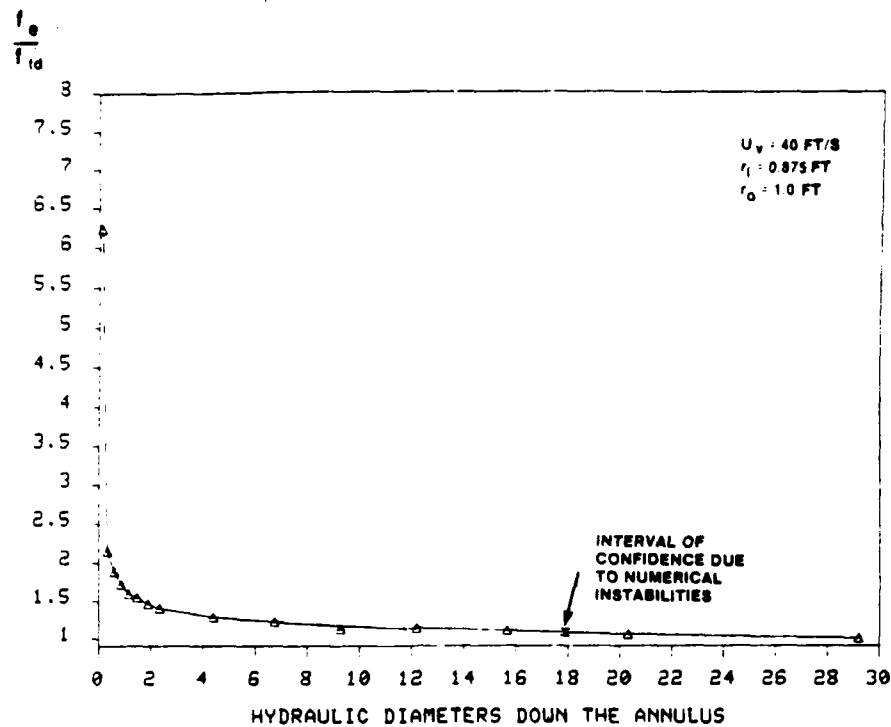


Figure 3-17. Friction Factors in Region of Developing Flow

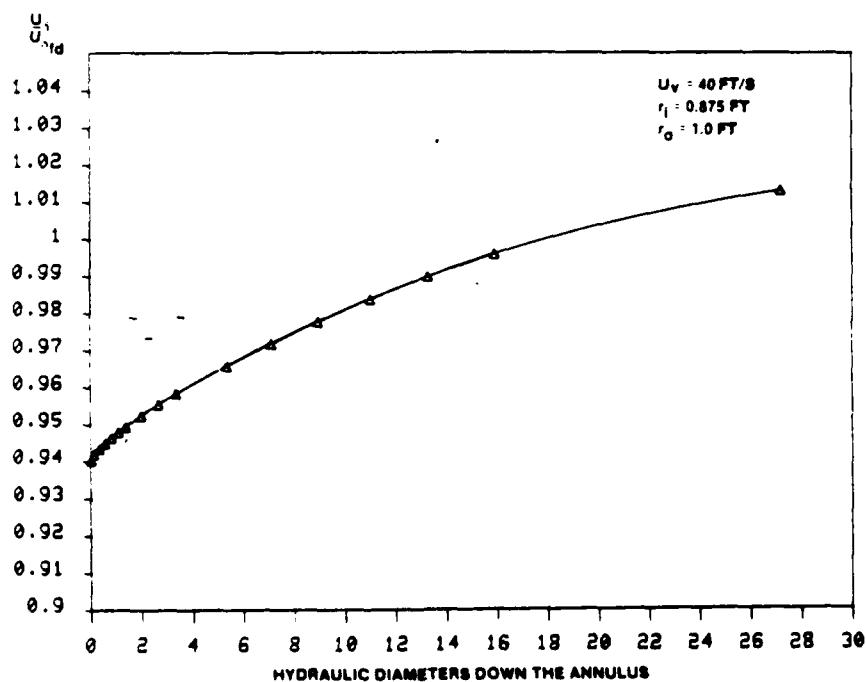


Figure 3-18. Core Velocity Growth in Region of Developing Flow

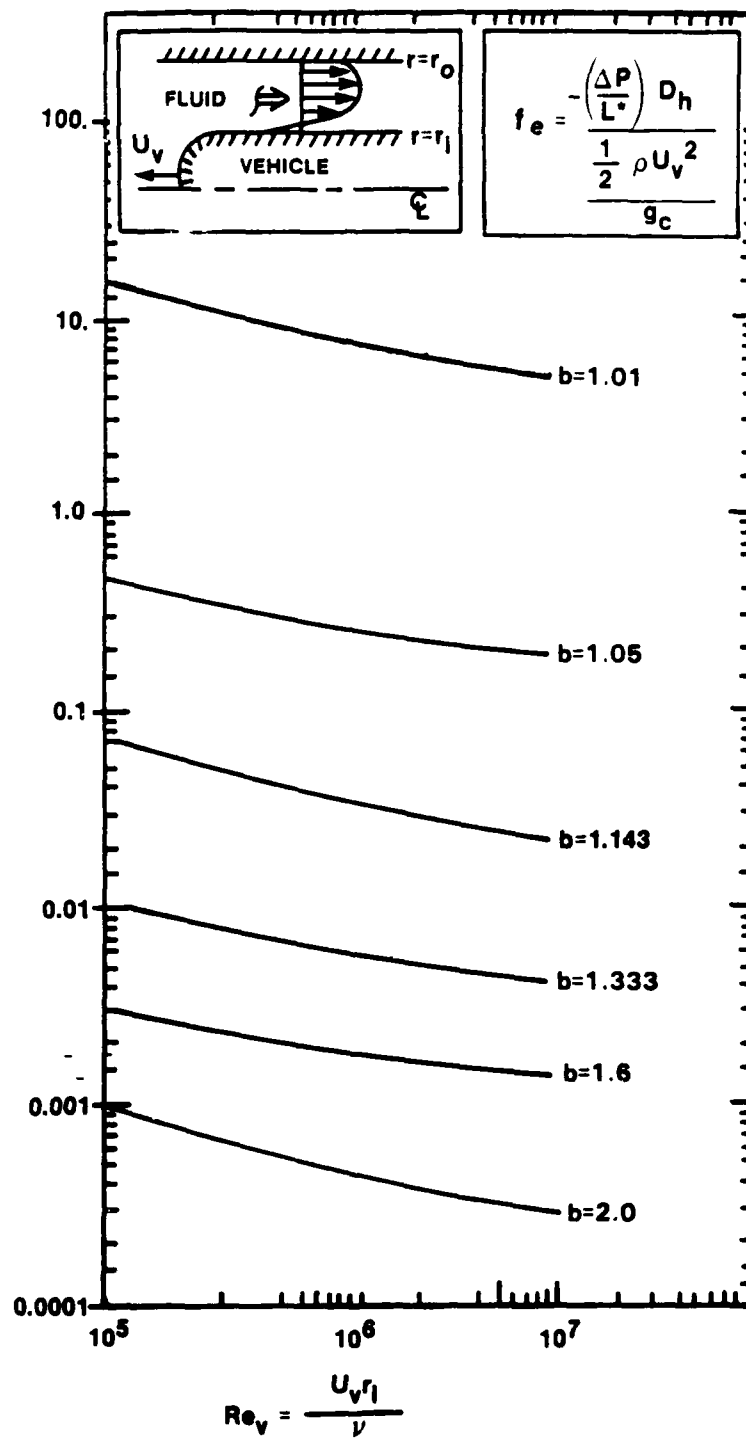


Figure 3-19. Friction Factors for Various Values of b and Re_v in the Region of Developing Flow

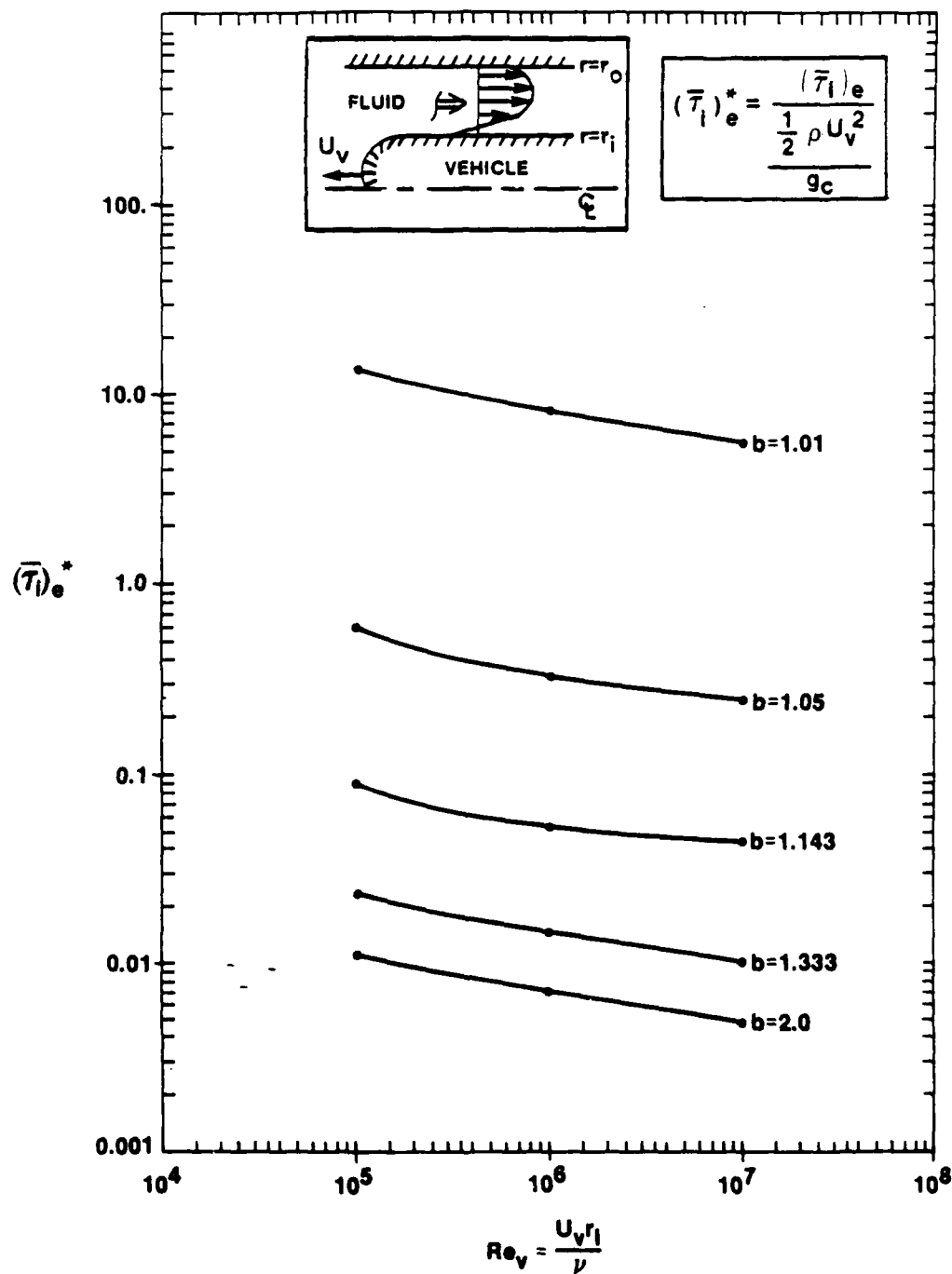


Figure 3-20. Dimensionless Average Shear Stress on Vehicle for Developing Flow

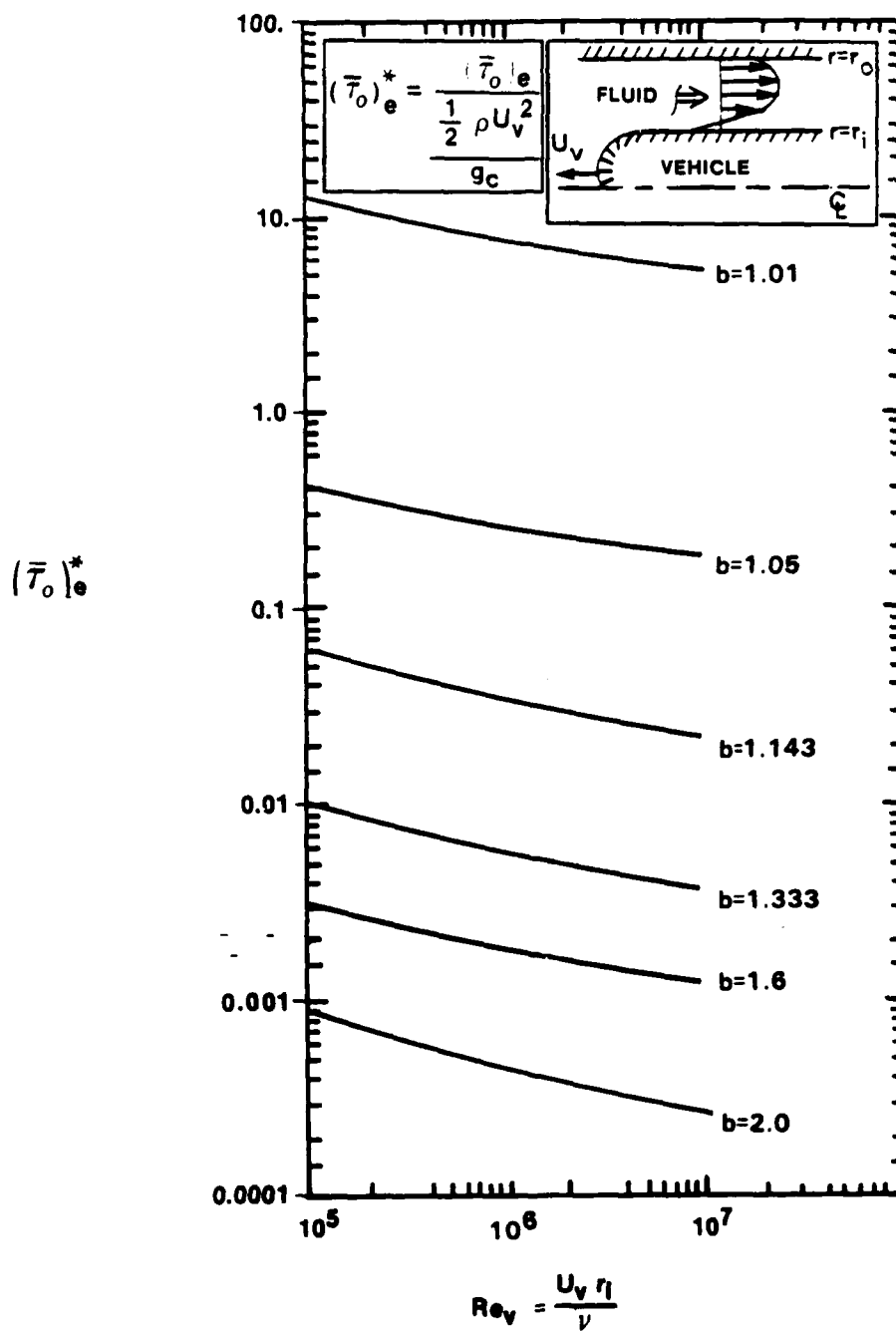


Figure 3-21. Dimensionless Average Shear Stress on Tube for Developing Flow

Figures 3-19 and 3-20 may be used to determine the drag only for the developing portion of the flow in the annulus. However, to actually calculate the drag (shear and form) in this region, entry length L^* is needed. Figure 3-22 provides this information. Appendix E shows how one would compute the drag force on a vehicle given U_v , L_v , r_i , and b using only figures 2-9, 2-10, 3-19, 3-20, and 3-22. Data tables used to generate curves for figures 3-19, 3-20, 3-21, and 3-22 may be found in appendix F.

Results for $Re_v = 10^4$ could not be obtained because of the following reasons:

1. For some cases the convergence criteria for continuity could not be achieved.
2. Shear stresses were seen to oscillate with increased axial distance.

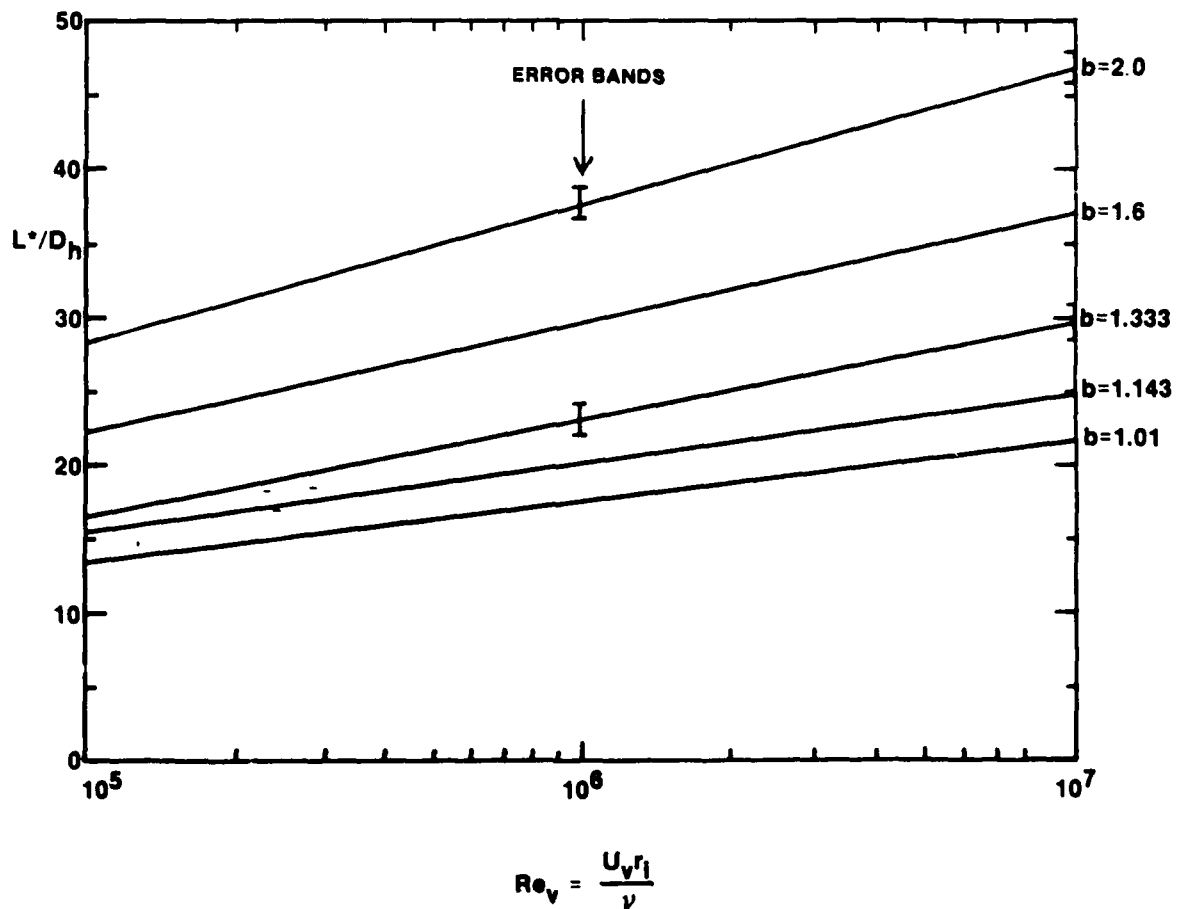


Figure 3-22. Entry Length for Various Values of b and Re_v

4. CONCLUSIONS AND RECOMMENDATIONS

Several conclusions may be drawn from this study:

1. The analysis presented herein has been proven to be self-consistent. The developing flow analysis for large x/D_h predicts nearly identical fully developed values for velocity profiles, τ_i , τ_o , δ_i , and δ_o . See appendix G.

2. The friction factors for fully developed flow are in good agreement with the results of references 5 and 19.

3. Assuming the annulus to be entirely fully developed would result in lower drag estimates for $L_v/d \geq 12$. However, for blunt vehicles with $L_v/d < 12$, the flow will be largely in a developing state. Thus, a fully developed approximation would yield extremely low drag predictions if applied toward the whole flow.

4. The Moody chart method (excluding entrance and exit losses) can lead to very inaccurate drag predictions for the fully developed condition. However, reasonable friction factors can be obtained if the modification of equation (2-46) is used.

5. Pressure signatures using the present theory compared well with the experimental results of reference 6. Refer to figure 3-12.

The integral method presented in this study is limited to a right circular cylinder confined in a concentric tube. An investigation using the finite element or finite difference solution for the entire body, which includes the flow over the ends of the vehicle, should be pursued. Such a solution applied to the confined wake would be:

1. More accurate
2. Not limited to $L_v/d \geq 10$ (limited by Hoerner coefficient)
3. Applicable to a variety of tail lengths and degrees of tapering.

Also, this solution applied to the flow over the nose would yield:

1. More accurate pressure signatures over the nose
2. Solutions for a variety of nose shapes
3. Much better approximation of the velocity profile at the entrance of the annulus.

It is not certain how much error was introduced by assuming a uniform velocity profile at the annular entrance. Intuitively, it is realized that the profile will actually be skewed, and that the effect of skewing will be felt throughout the annulus. The fluid's momentum has not been properly accounted for in this study since the boundary layer on the vehicle surface was assumed to begin after the nose section. Moreover, approximately one-half of the pressure drag can be attributed to the pressure drop over the nose of the vehicle (figure 3-12). The use of continuity and Bernoulli equations to adjust C_{nt} (nose coefficient from Hoerner) for the confined flow problem is only an approximation for the pressure drop across the nose (see appendix H). A more accurate method for determining this pressure field should be pursued.

The coefficient C_b (base coefficient) was assumed by Hoerner to be a function of $(\bar{\tau}_i)_e^*$ and $(\tau_i)_{fd}^*$ as shown in appendix H. This relationship may be true for external flows only and, therefore, may be inappropriate for internal flows.

The analysis presented in this report is limited to vehicles that have reached constant velocities. This may be largely the case for such applications as trains moving through tunnels. It is not exactly the situation encountered in a launching process where the vehicles or projectiles are accelerating while in the tube. This analysis should be extended to include vehicle accelerations.

Entry lengths L^*/D_h , reported in reference 32, have been improved by 10-40 percent. The following factors contributed to this improvement:

1. First-order (instead of second-order) curve fits of the last four computed points of the developing region were used to determine the slope of the boundary layers "i" and "o" at the last computed point, to extrapolate for the developed values.

2. Double precision was used when performing the momentum balances, equations (3-11) through (3-24).

APPENDIX A

COMPUTATIONAL SCHEME FOR DETERMINING DRAG IN THE REGION OF FULLY DEVELOPED FLOW

The velocity profiles were generated following the scheme in figure A-1. The generated profiles must satisfy continuity and the imposed boundary conditions listed in section 2. Velocity profiles were first generated for region "o," then for region "i." These profiles must meet at $r = r_{mt}$, the location of maximum velocity. This means that at $y^+ = y_{mo}^+$, the velocity U_{mo} predicted by region "o" computations must closely match the velocity U_{mi} at $y^+ = y_{mi}^+$, predicted from region "i" computations.

The general iteration procedure was obtained from reference 4. Graphic representation of the iterative scheme used, figure A-1, will now be explained in greater detail. Numbers preceding the following paragraphs correspond to the block numbers in figure A-1.

① The quantity r_o^+ was assumed, which is equivalent to specifying the shear stress on the tube wall from $r_o^+ = r_o \sqrt{\tau_o / \rho}$. An alternate physical implication of the choice for r_o^+ is apparent from the relationship $\tau_o = -\mu(du/dy)$, which implies that the slope of the velocity profile has been assumed. Having a good initial guess for r_o^+ would minimize the number of iterations required for convergence. The first estimate of r_o^+ for a specified U_{tube} was found as described in the following paragraphs.

The bulk velocity U_{in} entering the annulus is obtained from continuity, with the assumption that the fluid acts like slug flow at the annular entrance. The volume flux Q_a that approaches the stationary vehicle is

$$Q_a = \pi r_o^2 U_{tube} .$$

The volume flux at the annular entrance is

$$Q_{in} = (r_o^2 - r_i^2) U_{in} .$$

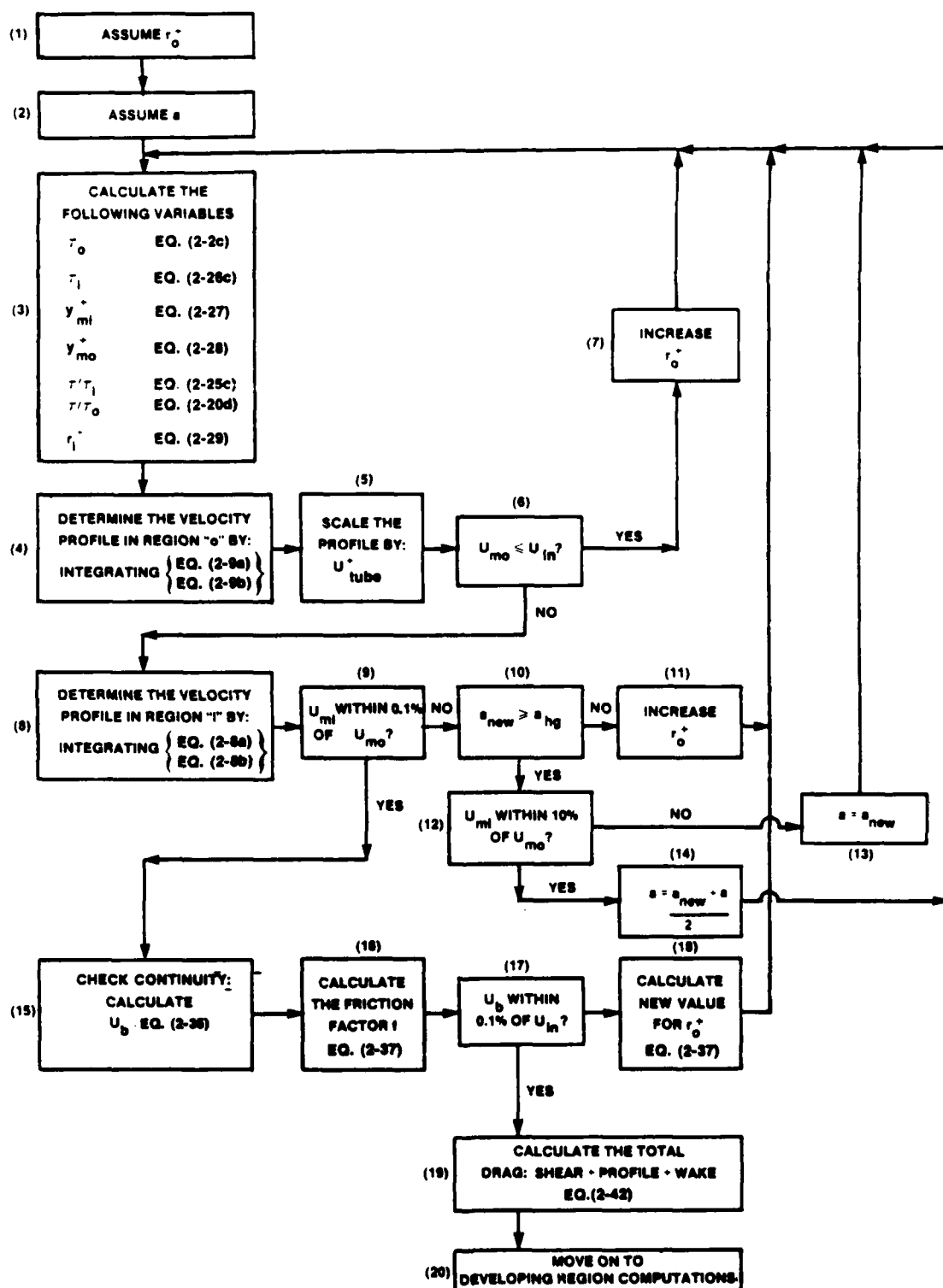


Figure A-1. Scheme for Determining Vehicle Drag in Fully Developed Flow

From continuity, $Q_{in} = Q_a$; the relationship between the inlet velocity U_{in} and the velocity U_{tube} is then

$$U_{in} = \frac{U_{tube} b^2}{(b^2 - 1)} \quad (A-1)$$

For turbulent annular flow through a concentric annulus, White (reference 32) suggests the friction factor is of the form

$$f = \frac{64\xi}{Re_b}, \quad \xi = \frac{(r_o - r_i)(r_o^2 - r_i^2)}{r_o^4 - r_i^4 - (r_o^2 - r_i^2) \log_e(r_o/r_i)}$$

The shear stress on the tube wall is found from the definition of friction factor, assuming that $\tau_i = \tau_o$. Then,

$$\tau_o = \frac{f \rho U_{in}^2 (b-1)}{2(b+1)}$$

Once the wall shear is known, r_o^+ may be easily determined from equation (2-2a) and one similar to equation (2-2c).

② A value of $a = r_{mt}/r_i$ is specified next; r_{mt} is obtained from equation (2-14).

③ The quantities τ_o , τ_i , y_{mo}^+ , y_{mi}^+ , τ/τ_o , τ/τ_i are determined from the equations specified in block (3) of figure A-1. These values may be determined once values for r_o^+ and a have been specified. The quantities τ/τ_i and τ/τ_o are needed before equations (2-8) and (2-9) can be solved.

④ Region "o" velocity profiles are generated by integrating equations (2-9a) and (2-9b). The Runge-Kutta method is used to perform the integration as explained in section 2. The step size for numerical integration is determined from a parametric study of $H \approx fcn(Re_v, b)$. The results of the

study are shown in figure 2-5, from which a curve fit was made. Only 100 steps were necessary to obtain sufficient accuracy when integrating for the sublayer profiles. Therefore, the curve fit applies only to the turbulent layer and will predict velocity profiles within ± 3.5 percent. The curve fit applies for the radius ratio range $1.01 \leq b \leq 2.0$ and for $10^4 \leq Re_v \leq 10^8$, where Re_v is based on vehicle radius and speed.

⑤ Equation (2-20d) was derived by assuming $U_{tube} = 0.0$. This value was assumed to simplify the algebra during the derivation. At this point, the velocity profile must be corrected by adding the dimensionless value for a chosen tube velocity U_{tube}^+ to the existing velocity components u_{o2}^+ :

$$u_{o2}^+ = u_{o2}^{+'} + U_{tube}/u_o^* .$$

⑥ The quantity U_{mo} , the dimensional velocity at the edge of the turbulent boundary layer for region "o," must be larger than the velocity U_{in} entering the annulus. This is true because the boundary layers have grown and met, causing the core fluid to accelerate to fully developed velocities so that continuity could be satisfied. The quantity U_{mo} is checked against U_{in} to accelerate convergence. If $U_{mo} < U_{in}$, the assumed value for the slope of the velocity profile at the tube wall is considered to be too small; thus r_o^+ is increased. A good control on the amount of increase was found to be

$$r_o^+ = 1.1r_o^+(U_{in}/U_{mo}) .$$

Blocks (3) - (7) are then repeated until $U_{mo} > U_{in}$.

⑧ Once $U_{mo} > U_{in}$, the velocity profile for region "i" is computed by integrating equations (2-8) in a similar manner as was done for region "o" (block 4).

(9) The dimensional velocities U_{mo} and U_{mi} must be nearly equal to comply with boundary condition no. 4 in section 2.

(10) If the condition in this block is not satisfied, the value for a_{new} from equation (2-31) is compared with the value a_{hg} where

$$a_{hg} = r_{mt}/r_i = [0.5(r_o - r_i) + r_i]/r_i .$$

(11) If $a_{new} \leq a_{hg}$, then r_o^+ is assumed to be too low. For annular tube flow, r_{mt} will lie above the centerline of the gap. This is especially true if the tube is moving. By increasing r_o^+ , τ_o is really being increased, which implies that the slope of the velocity profile at the tube wall is effectively increased. The quantity r_o^+ is increased by the following amount:

$$r_o^+ = r_o^+ + 10,000 .$$

This rate of increase for r_o^+ proved to work well in speeding the convergence for the range of Reynolds numbers and radius ratios tested. Blocks (3)-(10) are repeated until block (10) is satisfied.

(12) If $a_{new} \geq a_{hg}$, then r_{mt} must be located above $r_{mt} = a_{hg}r_i$, which is the expected condition. U_{mi} is checked to see if it was within 10 percent of U_{mo} .

(13) Since U_{mi} is not within 10 percent of U_{mo} , the full value of a_{new} from equation (2-31) is taken and blocks (3)-(12) are repeated until block (12) is satisfied.

(14) Since U_{mi} is within 10 percent of U_{mo} and block (9) is not satisfied, a more precise value for a must be determined. This is done by taking an average between a and a_{new} . Blocks (3)-(9) are repeated until block (9) is satisfied.

(15) Although U_{mi} is within 0.1 percent of U_{mo} , continuity must be checked. The volume flux that enters the annulus must be approximately equal to the volume flux at any axial location in the annulus. This is achieved by calculating the bulk velocity from equation (2-35).

(17) The bulk velocities are used as a basis for checking continuity rather than Reynolds numbers so that greater sensitivity can be gained from the smaller magnitudes of the velocities compared to the typically large values of Reynolds numbers.

(18) Since U_b is not within 0.1 percent of U_{in} , a new r_o^+ (slope of the velocity profile at the tube wall) is calculated from equation (2-37). Blocks (3)-(7) are repeated until block (17) is satisfied.

(19) Since the bulk velocity in the annulus U_b compares well with the bulk velocity entering the annulus U_{in} , the solutions for friction factor and wall shear stress have been found. Therefore, the total drag may be calculated from equation (2-42).

APPENDIX B

TABULATED RESULTS OF ANALYSIS FOR FULLY DEVELOPED FLOW

Re_v	b	a	f_{fd}	f_M	$(\tau_i)_{fd}^*$	$(\tau_o)_{fd}^*$	$\Delta P_{fd}/\Delta P_M$
10^4	1.01	1.00505	101.	0.03902	25.09	24.51	1.03
10^5		1.00506	49.3	0.02004	12.32	12.00	0.97
10^6		1.00506	29.5	0.007713	7.469	7.253	0.99
10^7		1.00506	19.7	0.005438	4.942	5.000	1.01
10^8		1.00506	14.0	0.005929	3.559	4.848	1.02
10^4	1.02	1.01019	25.5	0.03896	5.927		1.03
10^5		1.01023	12.4	0.02002	2.850		0.97
10^6		1.01024	7.43	0.01181	1.901		0.99
10^7		1.01025	4.97	0.007707	1.277		1.01
10^8		1.01026	3.54	0.005435	0.9110		1.02
10^4	1.03		11.4	0.03889	2.658		1.02
10^5			5.55	0.01999	1.312		0.97
10^6			3.33	0.01180	0.8667		0.99
10^7			2.23	0.007700	0.5547		1.01
10^8			1.59	0.005431	0.4146		1.02
10^4	1.04	1.02076	6.51	0.03883	1.509		1.03
10^5		1.02091	3.15	0.01997	0.7637		0.97
10^6		1.02095	1.89	0.01179	0.4996		0.99
10^7		1.02100	1.25	0.007694	0.3353		1.00
10^8		1.02106	0.901	0.005427	0.2397		1.02
10^4	1.05		4.21	0.03876	1.090	0.9730	1.03
10^5			2.03	0.01994	0.5381	0.4713	0.97
10^6			1.22	0.01178	0.3275	0.2838	0.89
10^7			0.817	0.007687	0.2201	0.1892	1.01
10^8			0.584	0.005423	0.1574	0.1347	1.02

Re_v	b	a	f_{fd}	f_M	$(\tau_i)_{fd}^*$	$(\tau_o)_{fd}^*$	$\Delta P_{fd}/\Delta P_M$
10^4	1.06	1.03171	2.95	0.03870	0.6867		1.03
10^5		1.03199	1.42	0.01991	0.3630		0.97
10^6		1.03212	0.856	0.01176	0.2304		0.99
10^7		1.03226	0.573	0.007681	0.1566		1.01
10^8		1.03238	0.408	0.005419	0.1104		1.02
10^4	1.07		2.19	0.03863	0.5126		1.03
10^5			1.05	0.01989	0.2756		0.96
10^6			0.634	0.01175	0.1712		0.98
10^7			0.429	0.007674	0.1175		1.02
10^4	1.08	1.04295	1.69	0.03857	0.4051		1.03
10^5		1.04345	0.811	0.01986	0.2179		0.96
10^6		1.04384	0.490	0.01174	0.1326		0.98
10^7		1.04398	0.328	0.007667	0.090215		1.01
10^8		1.04445	0.234	0.005412	0.06010		1.02
10^4	1.09		1.35	0.03850	0.3228		1.04
10^5			0.645	0.01984	0.1378		0.96
10^6			0.391	0.01173	0.1061		0.99
10^7			0.262	0.007661	0.07453		1.01
10^8			0.187	0.005408	0.05338		1.02
10^4	1.1		1.1	0.03844	0.02757		1.03
10^5			0.529	0.01981	0.1493		0.96
10^6			0.320	0.01171	0.08707		0.99
10^7			0.215	0.007654	0.06096		1.01
10^8			0.153	0.005404	0.04433		1.02
10^4	1.143	1.07999	0.05497	0.03801	0.1562	0.1151	1.02
10^5		1.08199	0.2677	0.01964	0.07994	0.05561	0.96
10^6		1.08303	0.1623	0.01163	0.04902	0.03310	0.99
10^7		1.08381	0.1089	0.007610	0.03319	0.02191	1.01
10^8		1.08433			0.02399	0.0156	
1.36E5	1.164	1.0974	0.1872	0.01822	0.05722	0.03747	0.93

Re_v	b	a	f_{fd}	f_M	$(\tau_i)_{fd}^*$	$(\tau_o)_{fd}^*$	$\Delta P_{fd}/\Delta P_M$
10^4	1.2		0.2994	0.03779	0.0824		1.03
10^5			0.144	0.01955	0.04584		0.96
10^6			0.0870	0.01159	0.02594		0.98
10^7			0.0588	0.007588	0.01911		1.01
10^8			0.0419	0.005366	0.01380		1.02
10^4	1.333	1.2075	0.1206	0.03694	0.04121	0.02108	1.03
10^5		1.21725	0.0583	0.01920	0.02108	0.009693	0.95
10^6		1.2221	0.0351	0.01142	0.01311	0.00565	0.96
10^7		1.22576	0.0237	0.007500	0.00903	0.003699	0.99
10^8			0.0172	0.005314	0.006542		1.01
10^4	1.4		0.0886	0.03652	0.03170		1.02
10^5			0.01628	0.01903	0.01642		0.95
10^6			0.0260	0.01134	0.01021		0.96
10^7			0.0177	0.007456	0.007128		1.00
10^8			0.0126	0.005289	0.004927		1.00
10^4	1.6	1.41288	0.0464	0.03532	0.01929	0.006823	1.01
10^5		1.43954	0.0223	0.01854	0.009974	0.002835	0.92
10^6		1.45194	0.0137	0.01111	0.006299	0.001606	0.95
10^7		1.46149	0.00921	0.007329	0.004430	0.001034	0.97
10^8			0.00667	0.005215	0.003038		0.98
10^4	1.8		0.0304	0.03422	0.01268		0.99
10^5			0.0146	0.01809	0.007386		0.90
10^6			0.00896	0.01089	0.004720		0.92
10^7			0.00620	0.007211	0.003315		0.96
10^8			0.00440	0.005146	0.002370		0.95
10^4	2.0		0.0223	0.03322	0.01122	0.00255	0.97
10^5		1.80723	0.0107	0.01767	0.006010	0.0009731	0.87
10^6		1.83229	0.00662	0.01068	0.003892	0.0005305	0.89
10^7		1.84989	0.00452	0.007100	0.002794	0.0003334	0.92
10^8			0.00332	0.005081	0.001988		0.94

APPENDIX C

COMPARISON OF MOODY CHART METHOD AND PRESENT THEORY FOR PREDICTING PRESSURE DROP THROUGH ANNULI WITH A MOVING BOUNDARY

The following example was performed to illustrate the difference between the pressure drop from the fully developed analysis and that from using the Moody chart.

The comparison applies for the following condition:

Vehicle roughness = smooth,

$$r_i = 0.875 \text{ ft,}$$

$$b = 1.1429,$$

$$L_v = 21 \text{ ft,}$$

$$U_v = 40 \text{ ft/s,}$$

$$\text{Fluid} = \text{sea water @ } 60^\circ\text{F, } \nu = 0.1258 \times 10^{-4} \text{ ft}^2/\text{s.}$$

Then,

$$\text{Re}_v = U_v r_i / \nu = 2.782 \times 10^6 . \quad (\text{C-1})$$

The Reynolds number associated with the Moody chart is

$$\text{Re}_b = U_b D_h / \nu = 3.39 \times 10^6 . \quad (\text{C-2})$$

By definition, the actual fully developed pressure drop is related to the friction factor f_{fd} by

$$\Delta p_{fd} = \frac{f_{fd} \rho U_v^2 L}{2 g_c D_h} . \quad (\text{C-3})$$

In comparison, a computation using the Moody chart would result in a pressure drop given by

$$\Delta p_M = h_f g / g_c .$$

where, neglecting entrance and exit losses, the Moody head loss is related to an appropriate average kinetic energy in the passage:

$$h_f = \frac{f_M L U_{av}^2}{D_h 2g} \quad (C-4)$$

From the continuity relation, the bulk and vehicle velocities are related by

$$U_b = U_v b^2 / (b^2 - 1) .$$

Because the inner and outer tube walls are moving at different speeds, the inner shear stress correlates with U_b , and the outer shear stress correlates with $(U_b - U_v)$. By choosing the arithmetic mean of these as the appropriate average velocity to use in equation (C-4),

$$U_{av} = U_b - \frac{1}{2}U_v = U_v \frac{b^2 + 1}{2(b^2 - 1)} \quad (C-5)$$

Combining equations (C-4) and (C-5) and using the Moody chart yields the pressure drop:

$$\Delta p_M = \frac{f_M \rho U_v^2 L}{2g_c D_h} \left[\frac{b^2 + 1}{2(b^2 - 1)} \right]^2 \quad (C-6)$$

where f_M is computed from equation (2-46) using Re_b as the appropriate Reynolds number. The two estimates of pressure drop given by equations (C-3) and (C-6) should be equal if the assumptions in the comparison are realistic. The ratio of these two equations is

$$\frac{\Delta p_{fd}}{\Delta p_M} = \frac{f_{fd}}{f_M} \left[\frac{b^2 - 1}{b^2 + 1} \right]^2 \quad (C-7)$$

For the particular example given in this appendix, the author has computed $f_{fd} = 0.135$. From equation (2-46), with $Re_b = 3.39 \times 10^6$, $f_M = 0.00933$. With $b = 1.143$, equation (C-7) predicts

$$\frac{\Delta p_{fd}}{\Delta p_M} = \frac{0.135}{0.00933} (0.2657)^2 = 1.02 .$$

For this example, the error in the Moody estimate is only 2 percent. This ratio, tabulated in table B-1 for a variety of values of Re and b , shows that the Moody approximation will result in an average error of ± 1.3 percent. The maximum error of 13 percent occurred at $b = 2.0$, $Re_v = 10^5$.

APPENDIX D

COMPUTATIONAL SCHEME FOR DETERMINING DRAG IN THE REGION OF DEVELOPING FLOW

The scheme used in this study for determining drag in the region of developing flow is depicted in figure D-1. The following text provides detailed explanations of the scheme. (Numbers preceding paragraphs correspond to the block numbers in figure D-1.)

① These inputs are the only ones necessary to run the computer code. NUMX is the number of axial stations to be used in the analysis. A typical value was NUMX = 20. However, greater accuracy may be obtained by assigning larger values to NUMX at the expense of increased central processing unit (CPU) time. The longest CPU time experienced by the author for a solution to the developing velocity profiles was approximately 2 hours. This was for just 20 axial stations, and $Re_v = 10^7$ for $b = 2.0$.

② The fluid density ρ (lbm/ft³) and kinematic viscosity ν (ft²/s) were acquired from subroutine "Viscosity." Sutherland's law was used to compute μ for air, and the ideal gas equation was used to find ρ . The viscosity for water was found by using an empirical formula developed by Bingham from reference 18. The values for a and δ_{imx}^+ were obtained from equations (2-43) and (2-44). If Re_v is something other than the values for which the equations were fitted, a linear fit between the encompassing Reynolds numbers will provide a fair estimate for δ_{imx}^+ . The number of iterations used in the Runge-Kutta routine for integrating the sublayer equations (2-8a) and (2-9a) was set to ITER = 1000. This was found to be sufficiently large for all radius ratios and Reynolds numbers tested. The number of iterations used to integrate the turbulent layer equations, ITER2, was determined from the curve fit shown in figure 2-5. The limit of integration for the region "i" turbulent layer, δ_{in}^+ for each station, depends on the number of stations NUMX to be evaluated. For example, if 10 stations were to be used, δ_{imx}^+ would be divided into 10 boundary layer heights (figure D-2). The first height would be $\delta_{i1}^+ = \delta_{imx}^+ / \text{NUMX}$. The next height would be $\delta_{i2}^+ = \delta_{i1}^+ + \delta_{imx}^+ / \text{NUMX}$, and so on. Each height corresponds

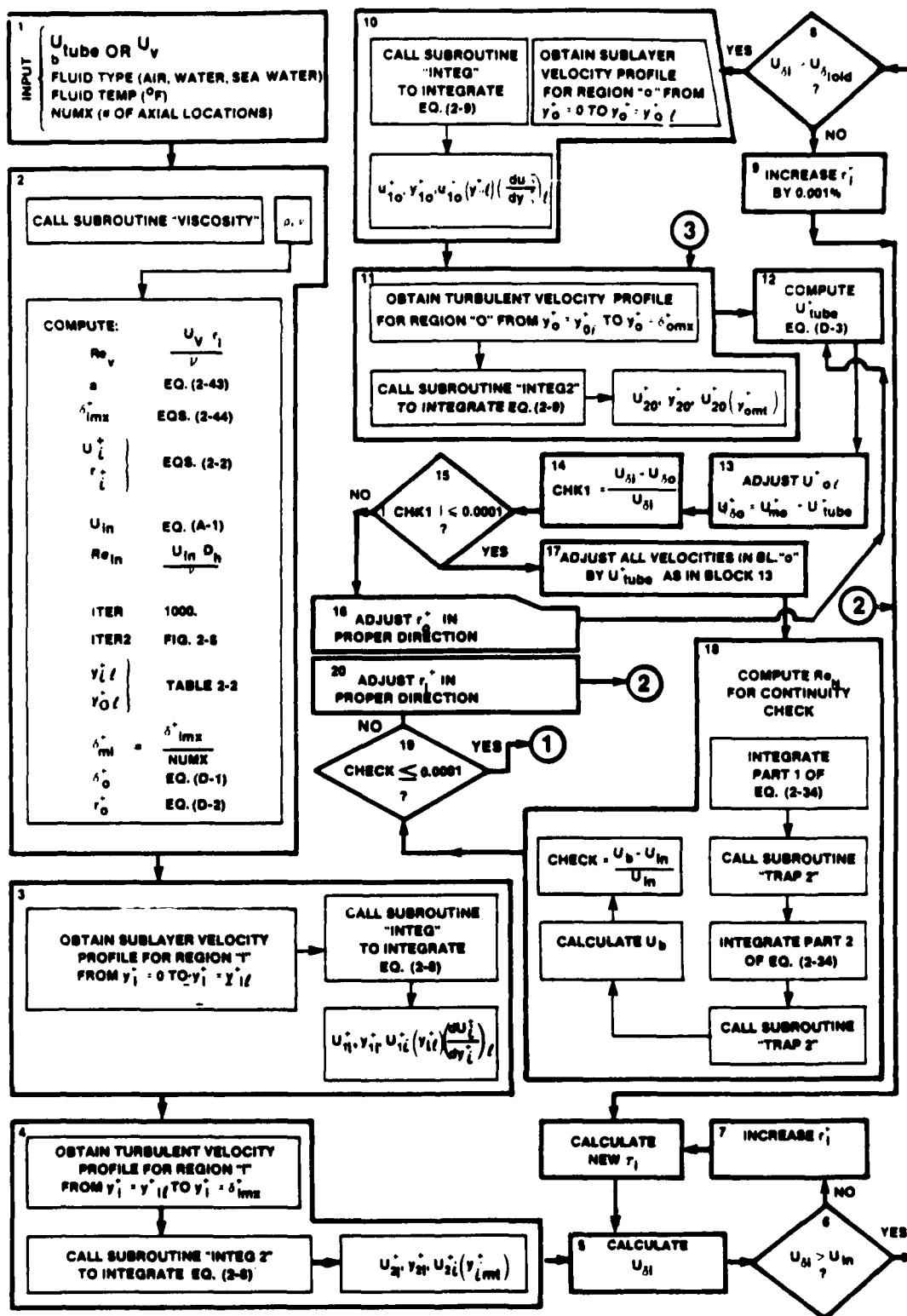


Figure D-1. Scheme for Determining Vehicle Drag in Developing Flow

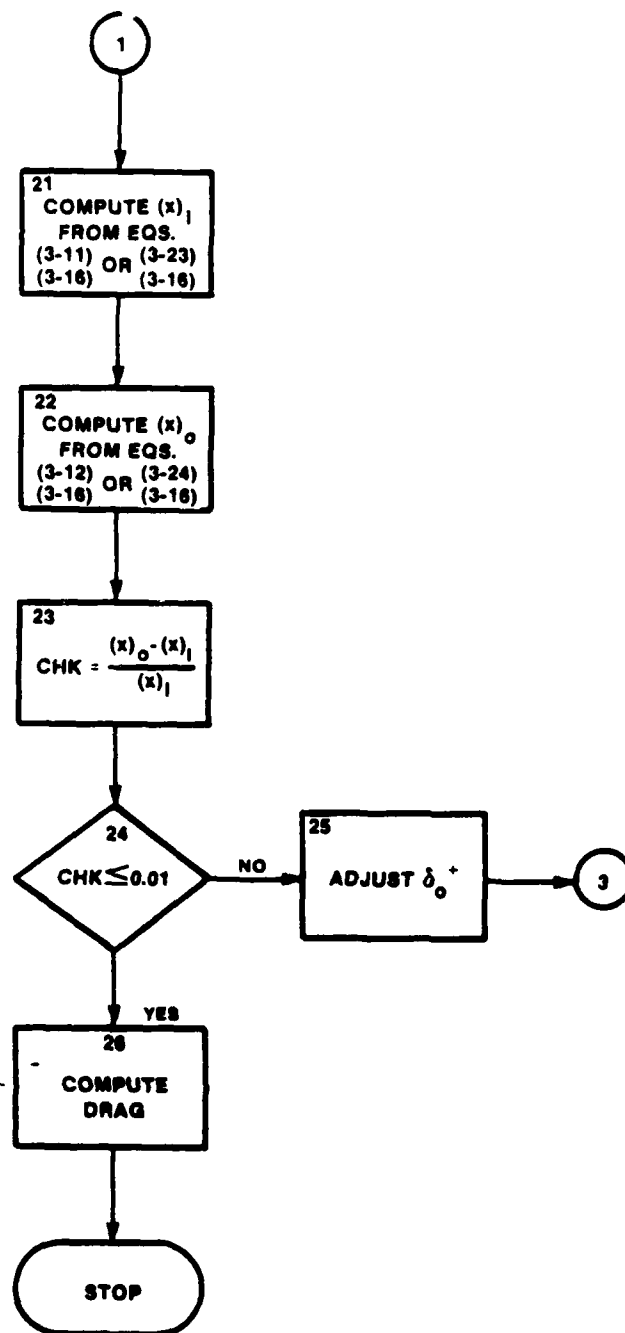


Figure D-1. Scheme for Determining Vehicle Drag
in Developing Flow (Cont'd)

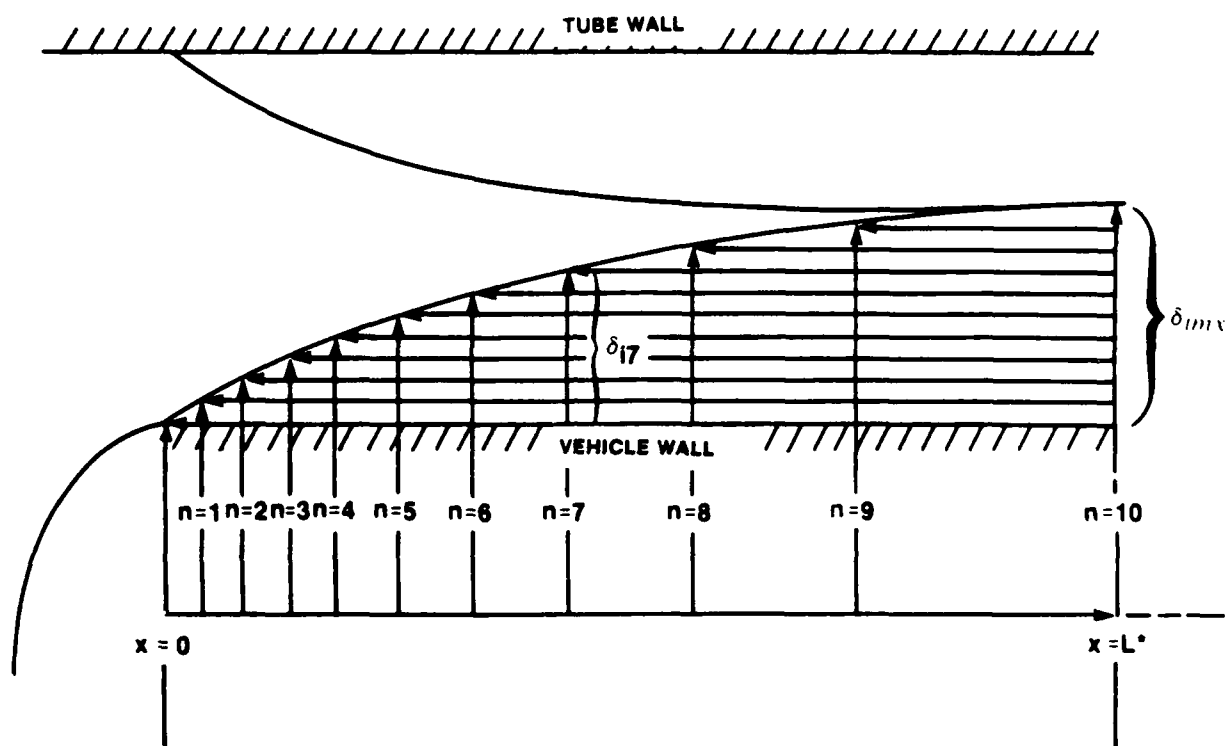


Figure D-2. Procedure for Choosing δ_{in}^+ for the Developing Flow Analysis

to a unique axial location. For each δ_{in}^+ , values of δ_0^+ and r_0^+ were estimated using the following curve fits of data from reference 5:

$$\delta_0^+ = 0.4131\delta_i^+, \quad (D-1)$$

$$r_0^+ = \text{ABS}(8/9r_i^+ - 1333.33) . \quad (D-2)$$

The values obtained from these curve fits serve only as first estimates and will be refined by iteration.

③ Subroutine "INTEG" at this point integrates equation (2-8a) from 0 to $y_{i\ell}^+$. The Runge-Kutta method is used to numerically integrate the equation. Subroutine "INTEG" outputs the following: $u_{1i}^+(y_{1i}^+)$, $u_{i\ell}^+(y_{i\ell}^+)$, and $du_{i\ell}^+/dy_{i\ell}^+$. The quantities $u_{i\ell}^+$, $y_{i\ell}^+$ and $du_{i\ell}^+/dy_{i\ell}^+$ are used as inputs to subroutine "INTEG2," which integrates equation (2-8b).

④ Subroutine "INTEG2" is called at this point to numerically integrate equation (2-8b) from $y_{i\ell}^+$ to δ_{in}^+ . The outputs of this routine are: $u_{2i}^+(y_{2i}^+)$, $u_{mi}^+ = u_{2i}^+(y_{imt}^+)$.

⑤ The dimensional velocity $U_{\delta i}$ at the boundary layer edge of region "i" is determined from

$$U_{\delta i} = u_{mi}^+ u_i^* .$$

⑥ The following condition is used to accelerate convergence:

$$U_{\delta i} > U_{in} .$$

The flow must accelerate through the annular core since the fluid is slowed down within the growing viscous boundary layers emanating from both the vehicle and tube walls.

⑦ Since the condition in block (6) has not been satisfied, it is assumed that r_i^+ is too low. Therefore, r_i^+ must be increased until block (6) is satisfied, which effectively means the wall shear stress τ_i is actually being increased.

A new τ_i is computed from equations similar to equation (2-2a). Blocks (5) through (7) are repeated until block (6) is satisfied.

⑧ Since block (6) has been satisfied, the velocity at the present location must be greater than the values at the previous locations. As the code progresses into the annulus, as shown in figure (D-2), values of δ_{in}^+ will increase.

⑨ Since the condition in block (8) has not been satisfied, r_i^+ is increased by 0.001 percent. Blocks (5) through (8) must be repeated until this condition is satisfied.

⑩ Now that a reasonably large value of $U_{\delta i}$ has been found, the velocity profile in the sublayer for region "o" is found by using subroutine "INTEG." This routine integrates equation (2-9a) between the limits of 0 to $y_{o\ell}^+$. "INTEG" yields: $u_{1o}^+(y_{1o}^+)$, $u_o^+(y_{o\ell}^+)$, and $(du_o^+/dy_o^+)_{\ell}$.

⑪ The values $u_o^+(y_{o\ell}^+)$ and $(du_o^+/dy_o^+)_{\ell}$ are used as inputs to subroutine "INTEG2," which numerically integrates equation (2-9b) between the limits of $y_{o\ell}^+$ to δ_{on}^+ . "INTEG2" yields $[u_{2o}^+, y_{2o}^+, u_{mo}^+ = u_o^+(y_{mot}^+)]$.

⑫ The assumed tube velocity U_{tube} is nondimensionalized as follows:

$$U_{tube}^+ = U_{tube} / u_o^* . \quad (D-3)$$

⑬ $U_{\delta o}^+$ is adjusted by U_{tube}^+ to account for the moving tube as follows:

$$U_{\delta o}^+ = u_{mo}^+ + U_{tube}^+ .$$

It is not necessary to adjust the whole region "o" profile at this point since more iterations may be required to match $U_{\delta o}$ and $U_{\delta i}$.

(15) $U_{\delta o}$ and $U_{\delta i}$ must be nearly equal due to the inviscid nature of the potential core. The fluid in the core region has not experienced any viscous effects due to the presence of the walls. The term

$$CHK1 = \frac{U_{\delta i} - U_{\delta o}}{U_{\delta i}}$$

provides a check on how close $U_{\delta o}$ is to $U_{\delta i}$. It also indicates the direction of correction. The matching criteria of 0.001 percent is chosen to ensure numerical stability during the computations for Re_b , equation (2-34), and dp/dx , equation (3-25).

(16) A series of checks is performed on the value of r_o^+ . Based on the disagreement between $U_{\delta i}$ and $U_{\delta o}$, r_o^+ is adjusted by using a linear interpolation scheme. Blocks (12-16) are repeated until block (15) is satisfied.

(17) At this point, block (15) has been satisfied, and now all the velocities in the boundary layer of region "o" must be scaled by the dimensionless tube velocity U_{tube}^+ to account for the moving tube.

(18) At this point, the core velocities $U_{\delta i}$ and $U_{\delta o}$ are nearly equal (within 0.001 percent). Continuity must now be checked by computing equation (2-34). Parts 1 and 2 of that equation are integrated using the trapezoidal rule. The bulk velocity is used rather than the Reynolds number to check for continuity. Bulk velocities are generally much smaller in magnitude than the typically large values of Reynolds numbers, which may make the check too sensitive to differences of large numbers.

(19) If continuity is satisfied, the location of velocity profiles is predicted. If continuity is not satisfied, then r_i^+ must be adjusted until continuity is satisfied.

(20) The quantity r_i^+ is adjusted by using a linear interpolation scheme based on the resulting value of U_b from the previous guess of r_i^+ . Increasing r_i^+ will increase U_b .

(21) The first velocity profile within region "i" is located by solving equations (3-11) and (3-16) simultaneously. Successive profiles within this region are located by solving equations (3-23) and (3-16) simultaneously.

(22) The first velocity profile in region "o" is located by solving equations (3-12) and (3-16) simultaneously. Successive profiles within this region are located by solving equations (3-24) and (3-16) simultaneously.

(23) Now the velocity profile for region "i" is checked to see if it has the same location as that for region "o."

(24) The quantity δ_o^+ is adjusted based on the discrepancy between $(x)_i$ and $(x)_o$ and the previous guess of δ_o^+ .

(25) Now both $\tau_i(x)$ and $\Delta p(x)$ can be integrated over the entry length L^* . These values are then multiplied by the vehicle surface area within the developing region and the projected vehicle area, respectively, to obtain the drag shown by equation (3-26).

APPENDIX E

DRAG PREDICTION USING FULLY DEVELOPED AND DEVELOPING FLOW RESULTS TO QUANTIFY THE VARIOUS DRAG CONTRIBUTIONS

This appendix demonstrates how one would compute the drag from both the developing and fully developed flows through the annular gap. This is accomplished by using only the graphs generated as a result of this investigation. Consider the following case:

$$\begin{aligned} r_i &= 0.875 \text{ ft}, \\ b &= 1.143, \\ L_v &= 21 \text{ ft}, \\ U_v &= 40 \text{ ft/s}, \\ \text{Fluid} &= \text{sea water @ } 60^\circ\text{F}, \nu = 0.1258 \times 10^{-4} \text{ ft}^2/\text{s}, \\ \text{Re}_v &= U_v r_i / \nu = 2.782 \times 10^6. \end{aligned}$$

The total drag force on the vehicle is:

$$\begin{aligned} (\text{DRG})_T = & \cancel{F_N}^0 + (\text{PDRG})_e + (\text{SHRDRG})_e + (\text{PDRG})_{fd} \\ & + (\text{SHRDRG})_{fd} + \cancel{F_B}^0. \end{aligned} \quad (\text{E-1})$$

Consider only the drag contribution due to the flow through the annulus. The nose drag (F_N) and base drag (F_B) are not included in this discussion. They can be approximated as described in appendix H.

The drag forces contributed by the developing portion of the flow are:

$$(\text{PDRG})_e = f_e \frac{L^*}{D_h} \frac{\rho U_v^2 A_v}{2g_c} = 14,788 \text{ lbf},$$

where $f_e = 0.1646$ (figure 3-19), and $L^*/D_h = 23.46$ (figure 3-22), and

$$(\text{SHRDRG})_e = (\bar{\tau}_i)_e^* \frac{\rho U_v^2}{2g_c} 2\pi r_i L^* = 2354 \text{ lbf} ,$$

where $(\bar{\tau}_i)_e^* = 0.04584$ (figure 3-20).

The drag forces contributed by the fully developed portion of the flow are

$$(\text{PDRG})_{fd} = \frac{(L_v - L^*)}{D_h} f_{fd} \frac{\rho U_v^2 A_v}{2g_c} = 31,252 \text{ lbf} ,$$

where $f_{fd} = 0.1348$, and

$$(\text{SHRDRG})_{fd} = (\tau_i)_{fd}^* \frac{\rho U_v^2}{2g_c} 2\pi r_i (L_v - L^*) = 5424 \text{ lbf} ,$$

where $(\tau_i)_{fd}^* = 0.04094$ (figure 2-10). Then, from equation (E-1),

$$(\text{DRG})_T = 53,818 \text{ lbf}.$$

For the case presented here, the drag contributions can be summarized as follows:

$$\left. \begin{array}{l} (\text{PDRG})_e = 22.5 \text{ percent} \\ (\text{SHRDRG})_e = 4.4 \text{ percent} \end{array} \right\} \text{ Drag due to developing flow.}$$

$$\left. \begin{array}{l} (\text{PDRG})_{fd} = 58.1 \text{ percent} \\ (\text{SHRDRG})_{fd} = 10.1 \text{ percent} \end{array} \right\} \text{ Drag due to fully developed flow.}$$

The shear and form drag contributions for developing and fully developed flows will vary with L_v , b , and Re_v . The shear drag will usually be less significant than the form drag for both flow regions.

APPENDIX F

TABULATED RESULTS OF ANALYSIS FOR DEVELOPING FLOW

Re_v	b	f_e	$(\bar{\tau}_i)_e^*$	$(\bar{\tau}_o)_e^*$	L^*/D_h
10^5	1.01	60.68	13.64	13.30	13.28
10^6		35.82	8.219	7.990	17.68
10^7		23.78	5.568	5.420	21.43
10^5	1.05	2.2511	0.5964	0.5207	14.19
10^6		1.470	0.3647	0.3148	17.18
10^7		0.9912	0.2462	0.2097	22.88
10^5	1.143	0.3298	0.08951	0.06128	15.15
10^6		0.1963	0.05434	0.03611	20.60
2.782×10^6		0.1646	0.04484	0.02987	23.46
10^7		0.1306	0.03721	0.02385	25.19
1.36×10^5	1.1664	0.2230	0.06324	0.04056	13.84
10^5	1.333	0.07047	0.02368	0.01043	17.13
10^6		0.04155	0.01471	0.006066	22.73
1.683×10^6		0.03695	0.01299	0.005387	24.08
10^7		0.02843	0.01009	0.003927	30.09
10^5	1.6	0.02689	0.01095	0.002896	22.46
10^6		0.01586	0.007009	0.001658	29.11
10^7		0.01096	0.004887	0.001067	37.33
10^5	2.0	0.01265	0.006554	0.0009288	27.76
10^6		0.007780	0.004309	0.0005190	37.96
10^7		0.005627	0.003107	0.0003324	46.0

APPENDIX G

DATA TABLES FOR $U_v = 40$ FEET/SECOND, $b = 1.143$ RUN

Table G-1. Entry Region Result for $U_v = 40$ ft/s, $r_i = 10.5$ in., $r_o = 12.0$ in.

x	x/D _h	U _δ	δ _i	δ _o	τ _i	τ _o	dp/dx	f _e
(ft)		(ft/s)	(ft)	(ft)	(lb _f /ft ²)	(lb _f /ft ²)	(lb _f /ft ³)	
0.000	0.0000	170.5273	0.000000	0.000000	370.339569	248.992249		
0.067	0.2694	171.0750	0.002395	0.001898	109.086792	71.947845	-3789.90063	0.5956
0.271	1.0837	171.9349	0.007115	0.005354	87.903572	57.793549	-1513.48376	0.2378
0.521	2.0815	172.8063	0.012106	0.009047	80.169029	52.633793	-1296.48340	0.2037
0.797	3.1856	173.6643	0.017233	0.012849	75.850349	49.771946	-1145.11975	0.1800
1.097	4.3821	174.5298	0.022433	0.016724	73.088577	47.938892	-1088.32935	0.1710
1.416	5.6602	175.4027	0.027657	0.020631	71.260376	46.682808	-1054.91357	0.1658
1.751	6.9968	176.2685	0.032868	0.024578	70.087509	45.779408	-999.52258	0.1571
2.099	8.3885	177.1318	0.038021	0.028497	69.451256	45.136513	-974.82605	0.1532
2.476	9.8934	178.0153	0.043086	0.032365	69.251076	44.708622	-998.05811	0.1568
2.870	11.4680	178.8936	0.048120	0.036192	69.181625	44.421341	-975.70728	0.1533
3.278	13.0990	179.7612	0.053309	0.040071	68.722549	44.163242	-931.64026	0.1464
3.742	14.9512	180.6366	0.058488	0.043914	68.371521	43.990250	-928.36432	0.1459
5.870	23.4555	185.0870	0.071477	0.053648	66.070000	43.599998	-858.90002	0.1350
Integrated Average					72.99	47.57	-1048.	0.1646
Fully Developed--> Analysis								
		182.75	0.07287	0.05213	65.197	43.599	-858.87	0.1348
%Difference--> Between Developing and Fully Developed Analysis								
		1.3	1.9	2.9	1.3	0.0		

Table G-2. Volume Flux for Profiles Shown in Figure 3-11

Profile #	Q _{IN}	Q _I	Q _{CORE}		Q _O		Q _{TOT}		
	(ft ³ /s)	(ft ³ /s)	% of Total	(ft ³ /s)	% of Total	(ft ³ /s)	% of Total	(ft ³ /s)	% of Total
1	125.66	5.93	4.7	113.40	90.2	5.32	4.2	124.65	99.2
2	125.66	36.05	28.7	57.41	45.7	32.15	25.6	125.62	100.0
3	125.66	61.26	48.8	9.34	7.4	54.02	43.0	125.62	99.2

APPENDIX H.

METHOD USED TO ESTIMATE NOSE AND BASE DRAG

The Bernoulli equation for constant elevation is

$$(u_2^2 - u_1^2) = -(p_2 - p_1) \quad , \quad (H-1)$$

where station 1 designates a point in the flow just ahead of the vehicle. Station 2 designates a point within the annulus at a distance from the throat equal to the length of the nose section.

Continuity requires that

$$\frac{u_2}{u_1} = \frac{A_1}{A_2} = b^2/(b^2 - 1) \quad , \quad (H-2)$$

where $A_1 = \pi r_o^2$ and $A_2 = \pi(r_o^2 - r_i^2)$.

The analysis assumes that $u_1 = U_v$. Substituting equation (H-2) into (H-1) leads to the expression for the pressure drop across the nose:

$$\Delta p_N = C_{nt} \frac{\rho U_v^2}{2g_c} - \left[\left(b^2/(b^2 - 1) \right)^2 - 1 \right] \quad .$$

The quantity C_{nt} is the nose coefficient from Hoerner (reference 30, page 3-12) that accounts for various nose types. In general C_{nt} can vary between -0.05 (ogive nose) and 1.0 (hollow nose). The drag force due to the pressure drop necessary to accelerate the fluid over the nose and into the annular throat is

$$F_N = C_{nt} \frac{\rho U_v^2}{2g_c} A_v \left[\left(b^2/(b^2 - 1) \right)^2 - 1 \right] \quad . \quad (H-3)$$

The drag force due to the low pressure region immediately behind the vehicle (from Hoerner) can be approximated by

$$F_B = C_b \frac{\rho U_v^2}{2g_c} A_v$$

$$\text{where } C_b = 0.29 \left\{ \frac{2 \left[(\bar{\tau}_i)_e^* L^* + (\tau_i)_{fd}^* (L_v - L^*) \right]}{r_i} \right\}^{-1/2}$$

Keep in mind that the relationships just derived for the drag over the nose and base of the vehicle are only approximate. Quantities C_{nt} and C_b were obtained from experiments performed in an infinite flow field.

REFERENCES

1. E. Becker, "Stromungsvorgange In Ringformigen Spalten (Labyrinth-Dichugen)," Zeitschrift V.D.I., vol. 51, 1907, pp. 1133-1141.
2. A. Quarmby, "An Analysis of Turbulent Flow in Concentric Annuli," Applied Scientific Research, vol. 19, July 1968, pp. 250-293.
3. A. Quarmby, "An Experimental Study of Turbulent Flow Through Concentric Annuli," International Journal of Mechanical Science, vol. 9, April 1966, pp. 205-221.
4. N. W. Wilson and J. O. Medwell, "An Analysis of the Developing Turbulent Hydrodynamic and Thermal Boundary Layers in an Internally Heated Annulus," ASME Journal of Heat Transfer, vol. 64, February 1971, pp. 25-32.
5. I. Sud and J. B. Chaddock, "Drag Calculations for Vehicles in Very Long Tubes from Turbulent Flow Theory," Journal of Fluids Engineering, vol. 103, June 1981, pp. 361-366.
6. J. V. Davidson, "Aerodynamic Drag of Tube Vehicles," Master's Thesis, Duke University, Durham, NC, 1974.
7. C. J. Lawn and C. J. Elliot, "Fully Developed Turbulent Flow Through Concentric Annuli," Journal of Mechanical Engineering Science, vol. 14, June 1972, pp. 195-204.
8. R. R. Rothfus, C. C. Mondrad, R. G. Sikchi, and W. J. Heideger, "Isothermal Skin Friction In Flow Through Annular Sections," Industrial and Engineering Design and Process Development, 1955, pp. 913-918.
9. W. M. Kays, E. Y. Leung, and W. C. Reynolds, "Heat Transfer With Turbulent Flow In Concentric And Eccentric Annuli With Constant And Variable Heat Flux," Engineering Report, Art. 4, Stanford University, Stanford, California, 1962.
10. J. A. Brighton and J. B. Jones, "Fully Developed Turbulent Flow in Annuli," ASME Journal of Basic Engineering, vol. 86, December 1964, pp. 835-844.
11. V. Mikrjukov, "Turbulent Flow of a Fluid in a Straight Pipe of Annular Cross Section," in Technical Physics of the USSR, State Technical Theoretical Press, Leningrad, vol. 4, 1937, p. 961.
12. F. R. Lorenz, "On Turbulent Flow Through Annular Passage," Communications, Institute of Fluid Mechanics, Karlsruhe, 26, 1932.
13. J. G. Knudsen and D. L. Katz, "Velocity Profiles in Annuli," Proceedings of the Midwestern Conference on Fluid Dynamics, First Conference, Illinois, May 1950, pp. 175-203.

REFERENCES (Cont'd)

14. S. Tomotika and I. Imai, "On the Velocity Distribution in Turbulent Flow through a Straight Pipe of Annular Cross Section," Rep. Aero. Res. Inst., Tokyo Imp. Univ., vol. 14, 1939 p. 301.
15. A. Quarmby, "Improved Application of the Von Karman Similarity Hypothesis To Turbulent Flow in Ducts," Journal of Mechanical Engineering Science, vol. 11, no. 1, 1969, pp. 14-21.
16. F. Page, W. G. Schlinger, D. K. Beaux, and B. H. Sage, "Temperature Gradients in Turbulent Gas Streams - Point Values of Eddy Conductivity and Viscosity in Uniform Flow Between Parallel Plates," Industrial and Engineering Chemistry, vol. 44, 1952, p. 424.
17. I. Sud, "An Analysis of Turbulent Flow and Heat Transfer for Vehicles Travelling In Tubes," Ph. D. Dissertation, Duke University, Durham, NC, 1974.
18. F. M. White, Viscous Flow, McGraw Hill, New York, 1974.
19. F. M. White, "An Algebraic Theory for Turbulent Flow in a Circular Annulus With A Moving Wall," (in preparation).
20. S. Tomotika, K. Tamada, and Y. Saito, "Application of the Similarity Theory of Turbulence to the Flow through a Straight Pipe of Annular Cross Section," Rep. Aero. Res. Inst. Tokyo Imp. Univ., vol. 15, 1940, p. 29.
21. R. M. Olson and E. M. Sparrow, "Measurements of Turbulent Flow Development in Tubes and Annuli With Square or Rounded Entrances," AIChE Journal, November 1963, pp. 776-779.
22. M. Okiishi and G. K. Servoy, "An Experimental Study of the Turbulent-Flow Boundary-Layer Development in Smooth Annuli," American Society of Mechanical Engineers Journal of Basic Engineering, vol. 89, December 1967, pp. 823-836.
23. E. R. G. Eckert and T. F. Irvine, Jr., "Proceedings Fifth Midwestern Conference on Fluid Mechanics," The University of Michigan Press, Ann Arbor, Michigan, 1957, pp. 122-145.
24. G. M. Gregorek and J. J. Engle, "An Experimental Study of Aerodynamics of Vehicles Travelling at High Speeds Through Long Tubes," The Ohio State University, Columbus, Ohio (Presented at the International Conference on Vehicle Mechanics at Wayne State University, July 1968).
25. R. G. Hoppe and S. W. Gouse, Jr., "Fluid Dynamic Drag on Vehicles Travelling Through Tubes," Report No. 1-59076-1, Carnegie-Mellon University, August 1969, NTIS No. PB 188 451.

REFERENCES (Cont'd)

26. S. F. Grittner, "Aerodynamic Characteristics of Vehicles Travelling in Perforated Tubes," Master's Thesis, Duke University, Durham, NC, August 1972.
27. L. D. Smith, "Experimental Investigation of Tube Vehicle Aerodynamic Characteristics," Master's Thesis, Duke University, Durham, NC, 1972.
28. A. H. Shapiro and R. D. Smith, "Friction Coefficients in the Inlet Length of Smooth Round Tubes," Technical Note 1785, U.S. National Advisory Committee For Aeronautics, 1948.
29. E. R. Van Driest, "On Turbulent Flow Near a Wall," Heat Transfer and Fluid Mechanics Institute Symposium, Paper 12, University of California, Los Angeles, CA, 1955.
30. S. F. Hoerner, Fluid Dynamic Drag, Published by the Author, 1965, pp. 3.7-3.14.
31. D. A. Kotlow, "Aerodynamic Drag of Cylindrical Vehicles Moving Concentrically Within Long Tubes," Master's Thesis, University of Rhode Island, Kingston, RI, 1985.
32. F. M. White, Fluid Mechanics, McGraw Hill, New York, 1979.

BIBLIOGRAPHY

- Barrow, H., Y. Lee, and A. Roberts, "The Similarity Hypothesis Applied to Turbulent Flow in an Annulus," International Journal of Heat and Mass Transfer, vol. 8, May, 1965, pp. 1499-1505.
- Clauser, F. H., "The Turbulent Boundary Layer," Advances in Applied Mechanics, vol. 4, Academic Press Inc., New York, NY, 1956, pp. 1-51.
- Davis, E. S., "Heat Transfer and Pressure Drop in Annuli," Transactions of the ASME, vol. 65, 1943, p. 755.
- "Experimental Aerodynamic Characteristics of Vehicles in Confined Spaces," Technical Report No. IRT-UMTA-DC-7-72-13, Caltech, Pasadena, CA, December 1972.
- Hammit, A. G., The Aerodynamics of High Speed Ground Transportation, Western Periodicals Co., 1973.

BIBLIOGRAPHY (Cont'd)

- Jonsson, V. K., and E. M. Sparrow, "Experiments on Turbulent-Flow Phenomena in Eccentric Annular Ducts," Journal of Fluid Mechanics, vol. 25, pt. 1, 1966, p. 65.
- Kurtz, D. W., and B. Dayman Jr., "Experimental Aerodynamic Characteristics of Vehicles Travelling in Tubes," NASA TM 33-731, National Aeronautics and Space Administration, July 1975.
- Lee, Y., "Turbulent Heat Transfer From The Core Tube In Thermal Entrance Regions of Concentric Annuli," International Journal of Heat and Mass Transfer, vol. 11, 1967, pp. 509-522.
- Lee, Y., and H. Barrow, Proc. I. Mech. Engrs., vol. 178, 1964, p. 1.
- Levy, S., "Turbulent Flow In An Annulus," ASME Journal of Heat Transfer, Series C, vol. 89, 1967, pp. 25-31.
- Mills, A. F., Journal of Mechanical Engineering Science, vol. 4, 1962, p. 63.
- Parker, D., and M. Satterthwaite, "Tests of the Three-Inch Spring Launcher Complete Breadboard," NUSC TM No. 82-2122, Naval Underwater Systems Center, Newport, RI, 13 October 1982.
- Tomotika, S., and K. Tamada, Rep. Aero. Res. Inst., Tokyo Imp. Univ., vol. 15, 1940, p. 77.
- Tomotika, S., and H. Umemoto, Rep. Aero. Res. Inst., Tokyo Imp. Univ., vol. 15, 1940, p. 61.

INITIAL DISTRIBUTION LIST

Addressee	No. of Copies
NAVSEA (SEA-56W13 (P. Crabb))	1
DTIC	12
CNA	1

END
DATE
FILMED

DTIC
10-88